

AN INVESTIGATION OF THE IRRADIATION PRODUCTS FORMED  
IN AIR BY NATURAL SPECIMENS OF CHALCOPHOSITE  
AS A FUNCTION OF TEMPERATURE

By

PATRICIA B. A. RULANDINI

A DISSERTATION PRESENTED TO THE GRADUATE SCHOOL  
OF THE UNIVERSITY OF FLORIDA IN  
PARTIAL FULFILLMENT OF THE REQUIREMENTS  
FOR THE DEGREE OF DOCTOR OF PHILOSOPHY

UNIVERSITY OF FLORIDA

1987

## ACKNOWLEDGMENTS

The author would like to thank her supervisory committee for their time and patience throughout this study. A great deal of growth and maturity on the part of the author is directly related to their continued help and guidance. In particular, special thanks and appreciation go to her committee chairman, Dr. P. H. Rabinow, through his understanding and encouragement she had the opportunity of working in France. Her work in France led to the topic of her dissertation and the subsequent construction of a diffractometer. His constant optimism and helpful suggestions during the construction of the diffractometer were invaluable. In addition the field of computer science was opened to the author with constant encouragement from her advisor.

Much gratitude and thanks go to Dr. Guy Rabinow when she worked for him in France. His time and help during her stay in France and in both the construction of the diffractometer and the research topic were always given with attention and care. The time spent in conferences with her committee and Dr. Rabinow when he was in Baltimore was always productive and much appreciated.

The love and support from her parents and family throughout all the years has never been appreciated. She is most grateful to her brother Edward who did the final dress figures both in this dissertation and in her master's thesis. Special thanks go to Dr. R. E. Becker whose time and patience helped the author during much of this study.

As for the friends both here in the U. S. and in Europe who were always there, often in ways not completely known, she thanks them for being so special and committed. Special thanks go to her husband who taught her much about electronic components and convinced her that computer interfacing could be understood. Much of the computer programming was discussed with Dr. E. Smith in whom she is greatly indebted for his idea and patience in teaching her many tricks of the trade. Most of the paper data was acquired by E. Hefenstey whom she and patients in appreciation by the author. She also thanks E. Riter for her help with all the printing necessary for the figures in this dissertation and E. Hefenstey for his help with the word processing and his constant encouragement.

A unique part of the author's story in Stansville has been her association with the sailing community. A deep interest is felt toward all of her sailing friends. Although not directly connected with this work they helped in many ways. The opportunity to spend time with all time and energy the author spent, and she thanks Dr. E. Hefenstey for the confidence in her sailing abilities. Much of her ability to keep her life and work in perspective is due to friends, her children, in which she spent much time enjoying and appreciating the marvelous science of sailing.

At the end of this work the author will take up a postdoctoral position in West Germany. The author is most thankful to her advisor Dr. F. H. Hefenstey who helped with the manuscript and Dr. E. Hefenstey for his wonderful encouragement.

# TABLE OF CONTENTS

ACKNOWLEDGMENTS	ii
ABSTRACT	iii
CHAPTER 1 INTRODUCTION	1
CHAPTER 2 LITERATURE REVIEW	7
Introduction	8
Properties of Chalcogenites	8
Surface Analysis of Minerals	10
High Temperature And Reduced Oxidation Of Chalcogenites	10
Low Temperature Oxidation of Chalcogenites	10
CHAPTER 3 EXPERIMENTAL METHOD AND ANALYTICAL TECHNIQUES	19
Sample Origin And Preparation	19
Natural And Induced Surface Oxidation And pHed Techniques	19
CHAPTER 4 RESULTS	40
Natural Oxidation in Atmosphere	44
Freshly Polished, Freshly Frosted, and Reduced Specimens	44
Reaction of Chalcogenites in Laboratory Air	48
Temperature Induced Oxidation in Atmosphere	70
Low Temperature Heat Treatment	74
Medium Temperature Heat Treatment	100
Examination of Film Structure of Reaction Products On Chalcogenites	100
CHAPTER 5 DISCUSSION	108
Introduction	108
Calculation of Solubility From Heated Chalcogenites	108
Relationship of Observed Reflectance Curves To Reaction Products	140
Polished	140
Solubility Curve Stage Surves from Oxide Thickness	140
Frosted versus Polished Specimens	140
Size Of Reaction Product in Bulk Chalcogenite Specimens	187

CHAPTER 1 SUMMARY AND FUTURE WORK	100
Summary	100
Future Work	101
APPENDIX A REFLECTANCE MODEL CALCULATIONS	103
APPENDIX B OPTICAL REFRINDIRECTOMETER BASIC PROGRAM	106
APPENDIX C SHIPER REFLECTOR BRILLIANTNESS ANALYSIS	108
RELIABILITY	110
BIBLIOGRAPHICAL LIST	112

Dissertation Presented to the Graduate School  
of the University of Florida in Partial Fulfillment of the  
Requirements for the Degree of Doctor of Philosophy

AN INVESTIGATION OF THE SURFACE OXIDATION PROCESS FORMED  
IN AIR ON NATURAL SPECIMENS OF CALCOPIPERINE  
AS A FUNCTION OF TEMPERATURE

By

Patricia E. A. Benschmidt

May 1980

Chairman: P. E. Ballou

Major Department: Department of Materials Science and Engineering

Kinetics of chalcopyrite at low temperatures on polished and fractured specimens has been studied. Auger electron and X-ray photoelectron spectroscopies were used to explore the spatial geometry and chemical state of the surface products formed between 25°C and 300°C in air. The reaction products consisted of an outer iron oxide layer and an intermediate copper rich sulfide layer. Several different oxides and sulfides were consistent with the electron spectroscopy data. To better identify the compounds present, specimens were analyzed at selected angles with an optical spectrophotometer at 5464 Å. Incident angle reflectance measurements allowed the reaction products to be analyzed as a function of time and temperature. Since the optical properties of a compound are unique, a reflectance model with homogeneous layers was used to explain reflectance curves by varying the compound in the thickness of each layer.

Using reflectance measurements, the reaction products were identified as  $\text{Co}_2\text{Fe}_2\text{O}_4$  in contact with the  $\text{CoFe}_2\text{O}_4$  and either  $\text{CoO}$  or  $\text{Co}_3\text{O}_4$  as an intermediate layer between  $\text{Co}_2\text{Fe}_2\text{O}_4$  and the outer oxide. The outer oxide was most consistent with  $\text{Fe}_2\text{O}_3$ . Relative thicknesses were calculated from a series of balanced chemical equations. The data show that the  $\text{Co}_2\text{Fe}_2\text{O}_4$  layer was much thicker than the layer of  $\text{CoO}$  or  $\text{Co}_3\text{O}_4$ . Calculated and experimental curves agreed well. This structure of reaction products was consistent for exposures between 40% and 80% $\text{O}_2$ , with thickness increasing with increasing temperature.

The total film layer thicknesses calculated at 40% were between 1500 and 2000. At 80% the thickness varied from 200 to 3500 with greater thicknesses calculated with longer reaction times. Thicknesses at 80% ranged from 1500 to 2000. Oxidation of  $\text{CoO}$  and  $\text{Fe}_2\text{O}_3$  transformed to a  $\text{Co}_2\text{Fe}_2\text{O}_4$  phase above 80% resulting in an increased total reaction product thickness adjacent to oxidation.

## CHAPTER 1 INTRODUCTION

Characterization of a material is a critical step in understanding its chemical and physical properties and determining potential industrial applications. A number of mechanical and chemical procedures are employed to prepare a specimen for analysis. Many techniques require flat polished surfaces while some require thin sections or ground particles. In general, a sample is produced from a larger specimen and polished as a bulk sample or ground to fine particles. Often chemical etching or ion etching techniques are employed to clean the specimen or to make thin sections for special microanalytical techniques. However, some techniques require a specimen to be coated. These procedures can have an effect on the specimen and are generally taken into account when determining the chemical and physical properties of a material.

In characterizing ore minerals (relevant specific to this study) within ores, the critical question asked by the mineralogist characterizing the uncrushed ore is what are minerals are present and in what quantities? The value of a mineral can depend on the amount and type of trace elements and other phases present within the bulk and consequently this can be an important factor in the steps chosen for further processing. In general, these questions are answered by optical observations, quantitative image analysis, scanning electron microscopy



SEM) and both techniques like electron probe microanalysis (EPMA) all of these techniques however, require a polished specimen.

Preparation of the ore after aging in the environment begins with a fracturing (initiating and propagating) process. After the initial fracturing process (which can be in air or vacuum) the ore goes through a differential etching process that selectively separates the components (inclusions) present in the ore. Further processing of the ore aimed to remove an amount of value can involve electrochemical cleaning, tumbling, or etching procedures either separately or in combination. To check into the homogeneity present at the surface are an indication of the probable success of the procedure. Thus, characterizing the surface morphology of a mineral mineral immediately after a leaching process is important to better understand the role of mechanical procedures, atmospheric action, and temperature effects. Both atmospheric action and temperature effects can induce surface changes on a fractured surface and on a polished surface. Much work has been done on fractured specimens. This leads to a basic question: how can ore preparation (initiating vs fracturing) affect the accuracy of analysis and therefore processing of the ore (mineral dissolution or differential etching effectiveness: tumbling, or etching)? Of primary interest to both microanalysts and surface scientists is the effect of temperature and of mechanical procedures (which is themselves not proven to increase in the temperature) on the surface products. In this study the surface products formed at low temperature are an important step (see section mineral surface morphology) will be investigated.

Chalcopryite,  $\text{CuFeS}_2$ , is a member of the sulfide family and occurs as a intermediate in nature. Some of its important properties are shown in Table 1.1. It is the only ore from which copper is extracted and is thus very valuable. The name is derived from the Greek word for brass in combination with pyrite. Its striking brass-yellow color observed on freshly fractured or polished specimens has lost in its more common name of "fool's gold". However, it is often found with an iridescent film due to surface oxidation.

Table 1.1  
Physical properties of chalcopryite ( $\text{CuFeS}_2$ ).

Crystal Structure	Orthorhombic, $a=0.356$ , $b=0.352$ , $c=0.395$
Color Luster	Brass-yellow, metallic
Phase Transformation	$\gamma\text{-CuFeS}_2$ , cubic $\text{CuFeS}_2$
Volume	$10^{-23}$ , $10^{-23}$
$\rho_g$	5.40 g/cm <sup>3</sup>
Brittleness	100 to 1000 x $10^{-8}$ dynes

Chalcopryite is one of the most stable sulfide minerals making efficient extraction (or recovery) of copper a difficult and challenging process. There is a compelling need to learn more about chalcopryite to pave the way for more cost-effective utilization. Hence, it is no wonder that its bulk properties have been extensively studied. However, the sulfide scientist has also interested scientists from the standpoint of mineral processing and more recently from the standpoint of surface science.

In general, bulk mineral samples have a number of planes which are often found as edges or large inclinations. In the technology of surface analytical techniques has developed similar means of analysis

have become possible. These surface analytical techniques lend themselves ideally to the study of surface oxidation of metal areas exposed within naturally occurring void-like structures. The surface oxidation of chalcopyrite can affect further processing stages of the ore mineral and is thus important to characterize from the standpoint of beneficiation.

A number of variations that affect the surface oxidation of chalcopyrite have been discussed, including chemical leaching, humidity effects, polishing techniques, and physical contact with other minerals. Air oxidation at room temperature (in laboratory air) has shown a slight color alteration on the surface of a polished specimen with further silver enrichment (from brown-yellow to a tan-orange) observed as a function of time in air (KROG). Extensive surface oxidation of weathered samples (fractured surfaces) has been observed and related to the chemical leaching character of the mineralogical site (FRANZ). The oxidation has also been found to induce surface coloration resulting from the oxidation products of the surface (FRANZ). Required contact between chalcopyrite and leachants of silver sulfate phases has been found to cause surface coloration which is also due to the oxidation products of the surface (FRANZ-KROG). Although a great deal of work has been expended to understand the surface reactions of chalcopyrite they have generally limited the areas of leaching (FRANZ, FRANZ-KROG), leaching (FRANZ-KROG) ( $\text{H}_2\text{O}^+$ - $\text{SO}_4^{2-}$ ), and leaching (FRANZ-KROG) ( $\text{H}_2\text{O}^+$ - $\text{SO}_4^{2-}$ ). Much less emphasis has been placed in the surface reactions of chalcopyrite in air for freshly fractured and/or polished specimens. However, the effects of slight leaching above room temperature on the surface reactions of chalcopyrite have not been studied.

Due to the nature of the specimens in this study, i.e. the presence of both dense and porous within the bulk which reduces the area of analysis. It was necessary to use analytical techniques with high spatial resolution. Previous studies on the surface oxidation (XPS) and related etching (SEM) of chalcopyrite specimens and related sulfides (PbS) have typically used Auger electron spectroscopy (AES) and X-ray photoelectron spectroscopy (XPS) for the characterization of surface films. Optical reflectance with high spatial resolution has been used in conjunction with the above techniques to further enhance the characterization of the compound formed at the surface (SEM, SEM-EDS, SEM-EDS) as optical microreflectometer (OM) was constructed as part of this study and used in conjunction with the above analytical techniques. The characterization process was enabled by the use of a reflectance model to calculate reflectance curves based upon a specific film geometry and compound identified on the surface of chalcopyrite.

It is the purpose of this investigation to characterize, using a combination of multi-analytical analytical techniques, the products formed on chalcopyrite. Natural specimens of chalcopyrite were heated in laboratory air at two temperatures (350°C-500°C) as compared to that is used for roasting procedures (>500°C) or smelting (>1200°C). Both polished and leached specimens will be compared to compare the reaction products formed at the surface after reaction in laboratory air. The results will be used to determine the reaction products that are indicative to chalcopyrite that prolonged oxidation effects are formed and the oxidation process monitored. In addition, the effect of inclusion within the bulk specimen will be discussed.

The balance of the dissertation will include a literature survey in Chapter 2 that describes the physical properties of chalcogenides, the use of various analytical techniques in chemistry, and the various oxidation studies that have been previously reported up to this time. The experimental methods and procedures are described in Chapter 3 with respect to the various analytical techniques employed in this study and the sample preparation and heat treatments used for bulk specimens. The experimental characterization of the reaction products on fractured and polished specimens as a function of temperature and time will be presented in Chapter 4. Lastly, a discussion and summary of the results will be presented in Chapter 5 and Chapter 6, respectively.

## CHAPTER 2 LITERATURE REVIEW

### Introduction

The most common and widespread sulfide mineral is pyrite ( $\text{FeS}_2$ ), which is most frequently associated with chalcopyrite ( $\text{CuFeS}_2$ ), sphalerite ( $\text{ZnS}$ ), and galena ( $\text{PbS}$ ). Within the binary Cu-Fe-S system chalcopyrite is the most common copper mineral (POLLAR) and the major ore mineral of copper. It is found naturally in contact with a number of other copper ores (PETER-ROSE, 1968) and silver ores (POLLAR). In addition to the presence of other sulfide minerals, silicates, carbonates, and silicate compounds are commonly found within naturally occurring chalcopyrite specimens. Quartz is the principal inert gangue mineral (POLLAR).

The copper sulfides commonly associated with chalcopyrite consist of covellite ( $\text{CuS}$ ) and chalcocite ( $\text{Cu}_2\text{S}$ ) and copper sulfide minerals having a stoichiometry in between covellite and chalcocite. The chalcopyrite specimens used in this study were found to contain inclusions of copper sulfide ( $\text{Cu}_x\text{S}$  or  $\text{CuS}$ ) and an iron sulfide with quartz as the gangue material. The iron sulfide region was later clearly identified due to some discrepancy in the mineralogical name used for iron sulfide minerals. These iron sulfide minerals are commonly found hematite, pyrrhotite, and kryptokobaltite (TIERCE, 1968). The name hematite ( $\text{Fe}_2\text{O}_3$ ,  $\text{Fe}_2\text{O}_3$ ) should properly be restricted to highly hydrated iron sulfide (with variable water content) that is crystalline or amorphous

in nature [FERN]. Serphite (or long iron ore) is a widespread iron oxide mineral (FeO), or ferrosil and the principal component of rust on steel. Lepidocrocite (FeO) has the same chemical formula as goethite however the OH is a hydroxyl group and it has a different crystal structure [FERN]. After hematite ( $\text{Fe}_2\text{O}_3$ ), serphite which consists mainly of microcrystalline goethite is the most abundant ferric oxide and is the stable form observed under the hydrothermal conditions near the earth's surface. Serphite with hematite forms the ground of soilite ores. The name was originally given to the iron oxides lepidocrocite (FeO) [FERN]. According to some studies goethite ( $\text{FeO}_2$ ) does not contain a hydroxyl (OH) group [FERN, FERN] but has octahedral hydrogen ( $\text{H}^+$ ) in tetrahedral coordination with the oxygen atoms. Reference reflectance data for goethite [FERN] with a chemical formula of FeO has a reflectance curve for two orientations which is characteristic of an orthorhombic structure (see Figure 2.10 in Chapter 4). In this study the results from the reference reflectance data will be used.

### Properties of Chrysotile

Chrysotile has a characteristic honey-yellow color with a white luster. Chrysotile is known as "Veil's gold", a term also applied to opals. It is brittle and often found naturally laminated. The structure of chrysotile is a superstructure of the silicate type [FERN], belonging to the tetragonal crystal (uniaxial) system with unit cell dimensions  $a=0.354$  nm and  $c=1.01$  nm [FERN]. Chrysotile exhibits a weak optical anisotropy [FERN] with a difference in refractive index between the two orientations (the ordinary refraction for extraordinary orientation) of less than 0.01 above the  $c$  to

The composition deviates only slightly from  $\text{GaSb}_{1-x}\text{Fe}_x$ . The phase is slightly metal-rich at high temperatures [1988a,1988b,1988c,1988d]. Half of the cation positions are occupied by Ga, half by Fe, and all ions are tetrahedrally coordinated. This ordered tetragonal structure is stable up to 577°C [1978a]. Above this temperature it is converted to a cubic high temperature form with the sodium chloride structure [1988a,1978b,1988c,1988d,1988e]. When heated above 500°C, chalcogenides gradually lose sulfur [1978a]. However, a published report of irreversible sulfur loss at 500°C was also found [1988b]. Neutron diffraction [1988f] and Raman scattering [1988,1988a] have been used to determine the magnetic moment arrangement and internal magnetic field respectively. Iron is present as  $\text{Fe}^{2+}$  with the high-spin  $d^6$  configuration, while sulfur is present as  $\text{S}^{2-}$ . However, there are some discrepancies in the data supporting these conclusions about the valence state of the copper and iron ions within the chalcogenide structure [1988g].

Chalcogenides is an semiconducting [1988a,1988b,1978c] semiconductor [1988b,1978c] with a band gap energy of approximately 650 eV and a thermoelectric power of 440  $\mu\text{V/K}$ . It is found to behave mostly as an n-type semiconductor [1978c], although some p-type specimens have been observed [1988a]. Raman scattering in chalcogenides has been observed as a slight metal-excess [1978c]. A metal excess (sulfur deficiency) corresponds to a donor defect (n-type conductor) above 510°C the conductivity increases, but not because of an intrinsic semiconductivity. Rather it is due to a deviation in the stoichiometry (due to partial dissociation and loss of sulfur). Thus, the n-type conduction is most likely a consequence of a slight metal-excess.



impurities. Iron substituted for copper has been reported to have a donor effect [1986i] while the reverse has an acceptor effect. A similar effect has been observed for copper substituted for iron in ferrite. Impurities have not been found to affect the martensitic rate or the reliability of chalcogenites. Natural  $\gamma$  type spinelites are rare, possibly because of the donor effect of excess nickel which results from the loss of sulfur from the bulk chalcogenite.

The direction of antiferromagnetism is parallel to the  $c$ -axis ( $c$ -axis direction [1981b]). The magnetic moments of iron and copper are  $1.4\mu_B$  and  $0.1-0.3\mu_B$ , respectively. Infrared absorption and Raman effect studies [1986b] reported a band gap of 0.34eV [1986c] and a hole mobility of  $30 \text{ cm}^2/\text{volt-sec}$  (natural  $\alpha$ -type single crystal spinelites) at liquid nitrogen temperature and  $20 \text{ cm}^2/\text{volt-sec}$  at room temperature [1986d]. The band gap is chalcogenite in due to the  $d$  electrons from the Fe.

The Cu-Fe-S ternary system may have the most phases of all ternary phase relations as suggested by preliminary research [1986a,1986b,1986c,1986d,1986e,1986f]. A list of the more common mineral compositions reported in the Cu-Fe-S ternary system is shown in Table 1-1. Some well reported variations in chemical composition are designated with a second chemical formula in parentheses for digenite ( $\text{Cu}_{1-x}\text{Fe}_x\text{S}_2$  versus  $\text{Cu}_9\text{FeS}_{10}$ ), tennantite ( $\text{Cu}_8\text{FeS}_9$  versus  $\text{Cu}_{10}\text{FeS}_{11}$ ), and covellite ( $\text{Cu}_2\text{S}_3$  versus  $\text{Cu}_{1.5}\text{S}_2$ ). The minerals of only interest in this study are chalcogenite ( $\text{FeFeS}_3$ ), bornite ( $\text{Cu}_5\text{FeS}_4$ ), chalcocite ( $\text{Cu}_2\text{S}$ ), and covellite ( $\text{CuS}$ ) which are the most common of the copper ore minerals. Additionally data on the phase relations at 100°C and below are tabulated due to their practical value.



### Surface Analysis of Minerals

Surface analytical techniques have been widely applied to the study of the surfaces of metals and alloys, giving valuable information concerning oxidation behavior. Additionally, the surfaces of dissolved semiconductors have been studied. The surface properties of the metal sulfides in atmosphere, however, have not been as extensively studied. More specifically, the semiconducting transition metal sulfide, chalcogenite, has been studied mainly with both analytical and microstructural techniques. Although optical reflectance techniques have been used, their main purpose has been for mineral identification with little work in the area of surface reactions in atmosphere of chalcogenites.

Surface analytical techniques were first extensively used in the field of mineralogy in the early seventies (1968, 1969, 1970, 1971, 1972, 1973) with X-ray photoelectron spectroscopy (XPS) being most commonly used. Sulfide minerals were studied due to their importance in the field of mineral processing and the role of surface chemistry in subsequent processing steps. Characterization of the surface oxidation states of sulfide minerals after reaction in aqueous solution have also been demonstrated with XPS.

The reaction of the surface of powdered sulfide minerals (ground in air) was characterized with XPS (1981) by distinguishing between different sulfur compounds (sulfide versus a sulfate). The inability to distinguish between different copper sulfide compounds such as  $\text{CuS}$ ,  $\text{Cu}_2\text{S}$ ,  $\text{FeS}$ , and  $\text{CuFeS}_2$  was reported. This results from a single Fe  $2p_{3/2}$  peak with no satellite peak characteristic of each compound. A number of associated and dissolved copper minerals were



are utilized for low grade ore minerals where the mineral is oxidized or reduced in the presence of aqueous solutions. Often leaching is used in combination with roasting and smelting procedures. Roasting and smelting processes involve high temperatures to oxidize the mineral as completely as possible to produce a slag which contains the element of interest. The oxidation products formed at temperatures in excess of 1000°C include copper sulfides, copper-iron sulfides, mixed copper-iron oxides, copper sulfates, sulfur dioxide and elemental S. The specific compounds formed are dependent on the temperature and oxidizing conditions. In the roasting or smelting of chalcopyrite the element desired is in the form of copper sulfide or copper oxide which can be leached with dilute acid while mixed oxides ( $\text{CuFeO}_2$ ) are depressed since they are insoluble and will lower the yield of ore in.

The effect of particle size, temperature, and reagent concentration on the dissolution of copper sulfides has been reviewed [1408] for a number of leaching systems. The leaching systems included sulfuric acid, ammonium, hydrogen, chloride, nitric acid, cyanide, and electrochemical dissolution. The most common leaching system is sulfuric acid in combination with various oxidizing agents.

In general the reaction of  $\text{CuFeS}_2$  in aqueous environments is very complex due to the number of variables that must be considered. A number of reaction products have been reported, however not all of these products are formed simultaneously. In fact within one aqueous system the reaction products can change due to changes in the reagent concentration [1409], solution pH [1409], temperature [1408], and the type of electrochemical dissolution (anodic versus cathodic) [1411]. The reaction products that have been reported include copper and iron

sulfides, elemental sulfur, sulfur dioxide, iron hydroxide, iron hydroxide, iron oxides, oxides (FeO), copper polysulfides ( $\text{CuS}_x$ ), copper sulfides in the composition range  $\text{Cu}_2\text{S}$  to  $\text{Cu}_2\text{S}_3$  and various copper-iron sulfides. The most common copper-iron sulfide reaction product reported in literature ( $\text{Fe}_2\text{S}_3\text{Cu}_2\text{S}_4$ ) while others are mostly associated with possible reaction products and include hydroxide ( $\text{Fe}_2\text{S}_3\text{Cu}_2\text{S}_4$ ), azide ( $\text{Cu}_2\text{S}_3\text{Cu}_2\text{S}_4$ ) and telluride ( $\text{Cu}_2\text{S}_3\text{Cu}_2\text{S}_4$ ). It is not possible to determine, from these studies, which reaction products are intrinsic to chalcopyrite and which are mainly dependent on the exposure environment, temperature, and solution pH. Thus, these studies have not led to a clearer understanding of the oxidation products of chalcopyrite. A reaction system with fewer variables is required to characterize the chalcopyrite oxidation system.

#### Low Temperature Oxidation of Chalcopyrite

The surface oxidation of chalcopyrite has been studied after air exposure (cleanly polished) [1989, 1990], exposure (ground particles) to air and distilled water [1991], exposure (crushed specimens) to dry oxygen or distilled water [1992] and exposure to moist air [1993] at 25°C. The contact between different elements present as inclusions in the bulk sulfide has also been shown to cause oxidation or surface alteration of chalcopyrite. Thus the presence of inclusions is important in the reaction at the surface of chalcopyrite.

A number of compounds have been postulated as the reaction products of chalcopyrite in air at temperatures less than 100°C. These range from iron oxides to iron hydroxides, sulfates, sulfides and polysulfides. The compounds that have been suggested also include metal sulfates, oxides and polysulfides. Elemental sulfur has also

been detected at the surface of chalcopyrite reacted in air. Due to the complexity of the Cu-Fe-S ternary system and the addition of S and water to this system the number of possible compounds quickly becomes very large. Increasing the temperature to those used in roasting and leaching procedures allows the formation of mixed Cu-Fe oxides, copper sulfates, copper sulfides and iron oxides.

These studies have observed the formation of mixed oxides on the surface of chalcopyrite. X-ray fluorescence has been conducted with thin thickness [XRF-L] and invasive wetting to form a compound at the surface of chalcopyrite [XRF-W] both in the bulk and from adjacent regions found in contact with chalcopyrite. Consequently, the reaction products that are intrinsic to chalcopyrite have not been well characterized but instead have been described in terms of their occurrence within very complex systems.

Polished bulk specimens of chalcopyrite [XRF-L] was produced in BPH as oxidation layers that was described as an outer layer of an iron sulfide with an iron oxide region between the outer layer and a copper rich sulfide which was in contact with the bulk chalcopyrite for diamond polishing. The outer iron sulfide region was not found after chemical etch polishing. Thus, even the polishing technique was found to cause a difference in the surface oxidation products of chalcopyrite. Optical microspectroscopy [UCM] was used to analyze the surface film formed after polishing and mixed oxides that were observed as a function of time in air. An overall decrease in reflectance was found for diamond polishing as compared to a chemical etch polishing sequence. Reflectance analysis [XRF-W] showed that the spots were due to an increase in the thickness of the surface iron oxide layer. Coloured

spots were found around holes or inclusions and may have resulted from water penetrating in the defects which would enhance the local oxidation process. A number of surface compounds and oxides were found to be associated with reflectance and IR data (RHEED) on surfaces subsequently incubated in air after diamond polishing. The incubating of chalcopyrites within a sphalerite ore was modeled with an outer iron oxide (FeO- $\text{Fe}_2\text{O}_3$ ) layer and an intermediate CuS outer  $\text{Cu}_2\text{S}$  layer that showed equivalent reflectance curves and were comparable to experimental reflectance curves. The film thickness of the layers was on the order of 100Å. The incubated areas were found to contain a small concentration of Ag at the surface which was mostly (but present in the bulk chalcopyrite) in the chalcopyrite region as the surface had not oxidized removed with spattering.

Chalcopyrite in contact with silver minerals (in veins or inclusions) has been found to undergo rapid tarnishing (RHEED) which appears to be caused by surface diffusion of Ag onto the chalcopyrite followed by its reaction to form  $\text{Ag}_2\text{S}$ . Different degrees of tarnishing were found after 4 months and have been correlated with different orientations (inclination). The surface reactions on chalcopyrites are important and are obviously influenced by the crystal orientation (presence of dislocations, and adsorbed species). Further studies on the relationship between Ag and tarnishing of chalcopyrites showed that tarnishing in the presence of silver sulfide could also be induced with a weak light source (RHEED RHEED). The colored areas were correlated with the content of Ag. A blue color associated with a higher Ag content. A reflectance model (RHEED RHEED) was used to calculate reflectance curves based on a  $\text{Ag}_2\text{S}$  (RHEED) outer layer and an internal



oxide  $\text{Fe}_2\text{O}_3/\text{Cu}_2\text{O}$  [MMA 6064] layer. Good agreement between calculated and experimental reflectance curves was demonstrated for the oxidation of chalcopyrite in contact with a silver sulfide layer.

In the air oxidation of chalcopyrite [TACI] surface analysis with X-ray photoelectron spectroscopy (XPS) showed a composition of  $\text{CuFe}_{1-x}\text{Cu}_x\text{S}_{1.25}\text{O}_{1.25}$  after washing in distilled water for 5 minutes. The sulfate peak was completely removed. The Cu peak was reported as being absent and after desorption had peaks at 931 (4s) (95) and 955 (s) (95) with relative intensities shown in parentheses. Thus, some  $\text{Cu}^{2+}$  was postulated (due to the peak at 955 eV) and an increase in the binding energy of the Cu 1<sub>2</sub>3/2 line) as a copper sulfate compound although this was not further discussed. No mention was made as to the color of the chalcopyrite either after washing or before. However, the fact that it was called a porous chalcopyrite implies that a mixed species was observed. An outer layer of  $\text{Fe}_2\text{O}_3 \cdot \text{H}_2\text{O}$  with an intermediate  $\text{Cu}_2\text{S}$  (polyoxidized) layer was reported in another study on the oxidation of chalcopyrite in air [MACE]. Further oxidation was shown to result in a copper sulfate according to XPS data. The copper sulfate presumably resulted from reaction of  $\text{Cu}_2\text{S}$  with oxygen:



Dry oxidation of chalcopyrite [TMAO] was studied with Auger electron spectroscopy (AES). Initial absorption of oxygen was associated with Fe rather than Cu as demonstrated by the fact that the low energy Fe 2pV peak at 478eV split into two peaks at 482eV and 485eV (C was at 285eV). Thus the Fe peaks have been associated with  $\text{Fe}_2\text{O}_3$  and mixed iron surfaces, that is, they appear to be associated with the formation of  $\text{Fe}^{3+}$ . The total thickness of the oxidation layer after 30

mineral's exposure to dry air was 12h. In addition, a specimen fractured in distilled water exposed to air was found to have a 100 layer after 1 minute's oxidation, and 100 after 90 minutes of oxidation. The outer layer formed during wet oxidation was a copper-rich region associated with both 8 and 9. The reaction products were not reported as a specific compound. A region under the copper-rich outer layer had a copper to iron ratio of 8.4 before reaching a bulk value of 1. Samples [PFA6] from naturally weathered pieces of chalcopyrite (utilizing AEM depth profiling) found fine layers that were much thinner and varied between samples. The variation was not described although it was implied as a difference in the total thickness of the fine layers. The observed fine grains forming on weathered pieces of chalcopyrite was reported [PFA6] to be due to the leaching of soluble copper oxide from the oxidized layer with subsequent reprecipitation onto the surface. This was found to be in agreement with with the copper-rich layer at the surface and an underlying iron oxide layer. Another study [TAK8] reported on iron hydroxide or oxyhydroxide layer and a copper sulfate after 2 hours in distilled water. The fine layer was reported to be approximately 100 thick. Exposure of chalcopyrite to 40% relative humidity at 25°C for four weeks [TAK8] resulted in iron oxides ( $\text{Fe}_2(\text{OH})_2\text{O}_4$ ), copper sulfate ( $\text{CuSO}_4$ ), elemental sulfur, and hematite ( $\text{Fe}_2\text{O}_3$ ).

In another study [BRI8] chalcopyrite was exposed to air or distilled water at room temperature with a relative humidity varying between 50% and 70% (this characterized with 60% exposure of chalcopyrite to air caused a rapid formation of iron hydroxide or oxyhydroxide within the first few layers. Rusty iron oxides ( $\text{Fe}_2(\text{OH})_2\text{O}_4$ ) was formed

subsequently was also stated to be the major oxidation product in air. The copper was found to remain in the same chemical state ( $Cu^{+2}$ ) as found in the bulk by monitoring the x-ray induced Cu L<sub>2,3</sub>PE line and the CuK $\alpha$ PEPE line as a function of reaction time (30 days) in air. Exposure to air was not found to involve the formation of basic sulfates ( $PbSO_4$ ) or sulfur (it is the first few layers of oxidation). Oxidation in distilled water gave rise to Fe as an impregnation or hydroxide. Copper was found in the same chemical state as that of the bulk. The formation of a sulfate was not observed ( $PbSO_4$ ).

Although a great deal of work has been done on the surface oxidation of chalcopyrite, the complexity of the system has led to many possible reaction products. At this point it is not clear what reactions are intrinsic to chalcopyrite and what are dependent on the environmental conditions of the study. Further very few studies have made any specific reference to the colored tarnishing observed in nature on polished specimens. Some wet oxidation, and as a result of physical contact between minerals. In general, colored tarnishing has been related to solution processes since weathering has produced such minerals that are friable. However, certain oxidation on polished specimens as a function of time has also produced colored tarnishing. To further investigate the oxidation of chalcopyrite this study has placed emphasis on testing natural specimens to approximate the oxidizing process and to further control the effect of humidity and long-time oxidation exposure. In addition, it was of interest to determine the effect of impurities that are present in bulk specimens of chalcopyrite.

The oxidation products formed in air at room temperature have consisted of both iron oxides and iron sulfates. However, there is some

discrepancy is to the presence of a copper sulfide, copper polysulfide, borosulfide, telluride, or selenosulfide. Evidently, there is some discrepancy in the products formed at low temperatures (<1500°C) and relative humidities ranging from 30% to 70%. In one case no copper sulfide is reported while in another case a copper trisulfide oxidizing to a copper sulfide is reported. The products that have been postulated in addition have been iron oxides, iron and copper sulfides, and a variety of copper and iron sulfide compounds.

## CHAPTER 2 EXPERIMENTAL METHOD AND ANALYTICAL TECHNIQUES

### Sample Origin And Preparation

#### Mineral Origin

The bulk chromatopelite specimens used in this study originated from two different deposits. The Le Rose deposit in Togo, France made up the majority of the samples used in this study. Two other phases--muscovite ( $K_2O$ ) and pyrochlore ( $ThO_2$  or  $UO_2$ )--were present as veins (or inclusions) within the chromatopelite matrix. Additionally, gangue is composed consisting mainly of silica commonly found within natural altered specimens, was present. In Togo specimens free of inclusions or veins of copper sulfides and iron oxides were used for comparison with specimens with inclusions in this study.

The second source of chromatopelite specimens used in this study originated from Idaho, Montana. These specimens contained veins of chlorite ( $Mg_2Si$ ) and pyrochlore as well as gangue material within the bulk chromatopelite. All specimens from the Idaho also contained inclusions. In some cases specimens with only  $Mg_2Si$  inclusions were used to study the effect of temperature on the leaching.

#### Sample Preparation

Large samples were fractured into smaller specimens by hand or with a light blow to the surface using a sharp instrument. For studying polished rather than fractured surfaces, samples were first cut with a Rockwell diamond saw to obtain roughing faces then a diamond or glass and

then hand polished. Hand polishing the specimens decreased the overall temperature effect which results from automatic polishing wheels. The polishing process utilized dry silicon carbide paper starting with 100 grit, then changing to 320 grit and finishing with 600 grit. The samples were ultrasonically cleaned in reagent grade acetone after for 10 minutes between each polishing stage to eliminate stray particles which could scratch the surface in a subsequent grinding stage. After the dry grinding steps the next stage consisted of diamond polishing the specimens (diamond polishing) in an ultrasonic bath consisting of equivalent proportions of alcohol and kerosene [TMAU]. The specimens were rinsed between polishing stages as described above. The diamond polishing compounds were obtained from Goodrich. Polishing was started with 1500 diamond paste and went through 1000, 500, and finished with 2500 diamond. The polishing times were longest for the 1500 and 1000 steps (approximately 10 minutes) and decreased for the 500 steps to 5 minutes and approximately 3 to 4 minutes for the 2500 steps. The surface of the polished specimens were checked periodically with a microscope for scratches between polishing stages to optimize the overall polishing process.

#### Sample Storage

Samples were stored before and after polishing in laboratory air. The relative humidity ranged between 40% and 70%. The temperatures ranged between 20°C and 30°C. Oxidized samples and bulk materials were stored in plastic containers under the above conditions. Samples were always handled with tweezers or plastic gloves after polishing or other treatments.

### Normal and Induced Surface Oxidation

#### Normal Oxidation in Laboratory Air

The reaction of chalcogenides upon exposure to laboratory air leads to a surface alteration that is a function of time in atmosphere and will be designated as normal oxidation. Data designated as being from freshly fractured or polished samples were collected immediately after fracturing a specimen or polishing a specimen in air. The effect of time on the reactions was decreased by withdrawing the specimen at the same position as a function of time. Normal oxidation of chalcogenides leads to a surface dissimulation which will be called tarnishing. The dissimulation may or may not lead to uniformity of color on the surface.

#### Induced Surface Oxidation in Laboratory Air

Oxidation (or alteration) of  $\text{GaSe}_2$  in air at temperatures above room temperature is designated as induced or accelerated surface oxidation. After polishing the specimens and obtaining data from the freshly polished surfaces the specimens were placed on an alumina boat and pushed into the hot zone of a quartz tube open to the ambient. A Marshall Furnace (Model 4 1400) was used with a Type B (chromium-clad) thermocouple. The temperature was collected and controlled to within  $\pm 4^\circ\text{C}$ . The furnace was allowed to equilibrate for 1-2 hours in air before the specimen was inserted into the hot zone of the furnace. The time of reaction at  $200^\circ\text{C}$  and  $300^\circ\text{C}$  ranged from 10 minutes to 24 hours. After brief treatment at a specified time the specimens were pulled out of the furnace immediately and allowed to cool at room temperature. The specimens were cooled within 1-2 minutes after removal from the furnace.

### Analytical Techniques

A number of analytical techniques were utilized to characterize the films formed on the surface of stainless steel. X-ray photo spectroscopy (XPS) is similar to surface film but reduction of data for surface analysis is very efficient and XPS is preferably used as a bulk technique. The source XPS, installed in Bureau de Recherches Chimiques at Marseilles in France was widely used to determine the composition of the bulk stainless steel both before and after heat treatment. Surface sensitive techniques such as X-ray photoelectron spectroscopy (XPS) and Auger electron spectroscopy (AES) were used to determine the compounds formed on the surface and over a depth into the sample. In addition to these techniques, an optical interferometer (OI) was built to analyze the film and the bulk as a thickness gauge. A model to calculate the reflectance was used to help identify the reaction products and determine the thickness and geometry.

#### Auger Photoelectron Spectroscopy

A Bruker KAM 400 Auger Photoelectron spectrometer (XPS) installed in the Department of Materials Science and Engineering at the University of Florida was utilized for this study. Chemical state information on the products formed on the surface of  $\text{In}_2\text{O}_3$  and as a function of film depth was obtained. However, XPS has been used as a versatile analytical tool to study the chemical structures of the species in thin films of the surface of metals, alloys, semiconductors, and minerals [1986 TARDY-THOM 1986, 1986 TARDY-THOM 1986, 1986 TARDY-THOM 1986, 1986 TARDY-THOM 1986, 1986 TARDY-THOM 1986]. Analysis with XPS is routinely used to study the surface processes occurring on organic compounds and polymers [1981]



The principles and characteristics of XPS are reviewed by (THERMOMAX, 1991). Briefly, core electrons are photoejected from the specimen under X-ray bombardment in accordance with the photoelectric effect which is schematically shown in Figure 8. The kinetic energy of the ejected photoelectrons ( $E_{kin}$ ) is equal to the energy of the incident X-ray ( $h\nu$ ) minus the binding energy of the ejected electron ( $E_B$ ) and minus the work function  $\phi_p$  of the spectrometer. For a monochromator a good electrical contact exists between the sample and the spectrometer so that the Fermi level is the same for the sample and the spectrometer (THERM). A work function relaxation energy (PREE) due to the removal of an electron from a localized energy level results in a lower binding energy of the ejected electron. The photoelectron originates from electron levels with binding energies less than the energy of the incident photon and are characteristic of a specific element.

The electron-photon interaction in XPS is a single interaction event which forms a singly ionized state that has two possible methods of relaxation or de-excitation. The first is an effect known as X-ray fluorescence where an electron from an outer shell moves to fill the inner electron vacancy (see Figure 8-1b) and a quantum of X-ray energy is emitted. It is difficult to release the excess energy. X-ray emission is an electromagnetic radiative process and depends upon the acceleration experienced by the emitting electron. Thus, a decrease in X-ray emission is expected with decreased energy. The second possible relaxation method is by a nonradiative relaxation of an electron known as the Auger effect (AUGER). The core level vacancy (for example in the K shell) can be filled with an  $L_1$  electron with the excess energy being

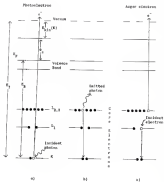


Figure 3.1 Schematic diagrams for three electron spectroscopy processes: a) X-ray photoelectron spectroscopy (XPS), b) X-ray analysis (XAS) and c) Auger electron spectroscopy (AES).

transferred to an  $L_{2,3}$  electron which is known as a Auger electron. This is schematically shown in Figure 2.4a. This Auger electron is said to originate from an  $KL_1L_{2,3}$  transition. The energy of the photoelectron is dependent on the energy of the incident photon. However, the energies of characteristic X-rays and Auger electrons are independent of the incident photon energy as long as there is enough energy to excite a core electron. Thus, X-ray independent can mean both photoelectrons and Auger electrons to be analyzed. However, Auger electrons in AED are conventionally produced by an electron beam as discussed below.

A Mg K $\alpha$  X-ray source (2000 W) was used to obtain UPS spectra. The ESCA 500 system uses a hemispherical electrostatic analyzer to measure the energy of the ejected photoelectrons. Two analyzer modes of operation are available for data collection. The first is the constant transmission mode designated as FID, and the second is the fixed retard ratio mode designated as FRR. In the FID mode, the transmission energy of the analyzer is kept constant so that the electrons entering the analyzer are retarded by an increasing amount as higher kinetic energy electrons are analyzed. In the FRR mode, electrons entering the analyzer have their energy retarded through the analyzer by a constant proportion of their initial energy. Thus, the transmission energy of the analyzer is constantly varied as the kinetic energy is varied in order to maintain the fixed retarding ratio. The FRR mode gives higher sensitivity in the low binding energy (high kinetic energy) region where C 1s, O 1s, S 2p, Fe 2p, Cu 2p, Ni 2p, and Fe 3p are analyzed. However, the Cu 2p peak was usually not detected in this mode due to its high binding energy. Consequently, the FID mode was used to record the Cu 2p peaks.

The 0° peak was assigned a value of 0.00V in both the PET mode and the RLS mode to compensate for sample charging.

A differentially pumped ion gun within the XPS system was used to sputter the films formed in micrographs. Argon ions with an energy of 5 keV were produced at a gas pressure of  $1 \times 10^{-8}$  Torr. The neutral incident pressure in the analysis chamber was  $1 \times 10^{-10}$  Torr.

Angle resolved or grazing angle XPS was used to increase the sensitivity to species at the surface [TOM1]. As the angle of electron emission relative to the sample surface is decreased, the surface area analyzed is increased while the sample depth analyzed is decreased, thus less the effect of increasing the relative peak intensities of the surface species. An angle of 60° was used for normal analysis while a grazing angle of 20° was used for angle resolved analysis [TOM2]. A standard peak deconvolution routine from Shirley software was used to assign specific peaks. The relative peak intensity was documented in this study and can be used to relate between deconvoluted peaks within the same scan and compare an equivalent ratio to another scan.

### Scanning Electron Spectroscopy

A Perkin Elmer Model 550 Scanning Super Microprobe (located at Parks Japan in Orlando, Florida) was used to analyze the surfaces of chlorinated species. For some of the super electron spectroscopy (SES), a Perkin Elmer Model 550 assembly located in the Department of Materials Science and Engineering at the University of Florida was utilized. Specifically, SES [TOM3, TOM4] has been used to study the spatial distribution of specific elements over the surface and their variation with depth into the solid. SES is being used to study microstructures, which, alloys and minerals to study the other surface

inputs for excitation, surface detection, or abnegation, as well as diffusion studies (often in conjunction with a number of surface analytical techniques) [JAHN 1980, JAHN 1982, JAHN 1983].

Auger electrons are produced whenever incident radiation with an energy exceeding that necessary to remove an inner-shell electron (such as photons, electrons, ions, or neutral atoms) interacts with an atom. In AES, electrons are used as the probing or primary source. Before the atom is ionized while with a core hole, that is a missing inner-shell electron. The atom is then in an unstable excited state and de-excitation occurs rapidly (approximately  $10^{-15}$  sec.), resulting in the emission of an X-ray (discussed above) or an electron called an Auger electron (as discussed above). The emission of various other Auger electrons is possible because each atom has several electron levels and sublevels. The driving force behind Auger transitions is the electrostatic force between electron-shells of unfilled shells (filled shells are symmetric and thus produce no net force).

Auger spectra are displayed as the number of electrons with a specific energy distribution,  $N(E)$ , versus energy. For this spectrometer the data were collected in the  $N(E)$  mode. However small Auger signals often occur on a high background. Consequently, an  $N(E)$  spectrum can be enhanced by taking the derivative  $dN(E)/dE$  of the spectrum. Peak-to-peak heights in the  $dN(E)/dE$  spectra are used to quantify Auger spectra since they are often proportional to the number of atoms exciting the Auger electron [JAHN 1980].

An electron gun is used for primary electron excitation of the sample. The primary electron beam energy in this study was generally held with a beam current of 0.0004. The beam pressure of the vacuum



the Remickberger equations. This procedure is discussed in Appendix A (Equations A. 97 and A. 10).

DESCRIPTION OF CHOPY. The reflectance spectroradiometer (see Figure 6. 8) was developed by Choy (1969). There are four main components (see Figure 6. 8): (1) a white light source, (2) a monochromator (see Figure 6. 8), (3) the microscope and (4) a detector. White light from the source is monochromatized and focused onto a sample by the microscope. The reflected light is also focused by the microscope and its intensity is measured by the photomultiplier tube. The result is a reflectance curve (i.e., a plot of percent reflectance versus wavelength). A standard (114) is generally used to determine the reflectance of an unknown specimen;  $R_{spec}$  is:

$$R_{spec} = R_{stan} (I_{spec}/I_{stan}) \quad (6-12)$$

where  $I_{spec}$  or  $I_{stan}$  represents the reflected intensity from either the specimen or the standard respectively, and  $R_{stan}$  is the known reflectance of the standard. The reflectance curve for a bulk homogeneous solid may also be calculated using the complex index of refraction. Although more complicated, a reflectance model was developed to calculate reflectance curves for a bulk solid covered with a thin absorbing layer of a different chemical composition (1980). This model is described in Appendix A and assumes normally incident light onto an absorbing substrate coated with one or more thin absorbing films. The substrates and films are assumed to exist with perfectly parallel interfaces. Development of the model starts with the interaction between substrate 1 and air 2. The reflectance coefficient between medium 1 and 2 is given by



Figure 3.1 Schematic diagram of the optical microreflectometer used in this study. The labeled components are discussed within the text.

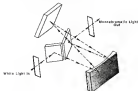


Figure 3.2 Optical layout of the Brillouin scattering experiment with 1000 lines per cm ruled.



$$R_{12} = \frac{(n_1 - n_2)^2 + (k_1 - k_2)^2}{(n_1 + n_2)^2 + (k_1 + k_2)^2} \quad (9.1)$$

where  $n$  is the real refractive index and  $k$  is the extinction coefficient. The optical constants  $n$  and  $k$  are related to the complex index of refraction  $\tilde{n}$  by  $\tilde{n} = n + jk$ . The phase change  $\Phi_{12}$  of light reflected at the interface is given by

$$\tan(\Phi_{12}) = \frac{2n_1 k_2 - n_2 k_1}{(n_1^2 - n_2^2) + (k_1^2 - k_2^2)} \quad (9.2)$$

Equations 9.1 and 9.2 may be extended to a substrate covered with a thin film in contact with air. Reflection at both interfaces give multiple internal reflections within the single homogeneous layer is traced and summed to obtain the complex amplitude of the wave reaching the detector. An overall phase change can be described which includes phase changes due to reflection at successive interfaces and the phase changes due to optical path difference. The resulting reflected intensity from a substrate (0) covered with a thinning thin layer (1) in contact with air (2) is denoted as  $R^*$  where  $d$  is the thickness of the film and  $\lambda$  is the wavelength of light:

$$R^* = \frac{R_{11} + R_{22} e^{2ikd} + 2(R_{11} R_{22})^{-1/2} e^{ikd} \cos(\Phi_{11} + \Phi_{22} - \tan^{-1} k_1/n_1)}{1 + R_{11} R_{22} e^{2ikd} + 2(R_{11} R_{22})^{-1/2} e^{ikd} \cos(\Phi_{11} + \Phi_{22} - \tan^{-1} k_1/n_1)} \quad (9.3)$$

where  $k = 2\pi \tilde{n}_1/\lambda$ .

Thus, for a single homogeneous layer, the resulting reflectance,  $R^*$ , is a function of the phase changes at each interface  $\Phi_{12}$ , the reflection from each interface  $R_{12}$ , the optical constants  $n$  and  $k$ , the film thickness  $d$  and the wavelength of light  $\lambda$ . This model can be

attached to multiple this film in a substrate through an adhesive procedure as discussed in Appendix A [B088].

DESCRIPTION OF EQUIPMENT. In addition to the components that make up the DM (see previous section), the computer interfacing used to step the monochromator and record the reflected intensity from the photoconductor will also be discussed. Finally, the data collection and data reduction procedures used to obtain the reflectance curves of a specimen will be described.

A detailed description of the DM where the details for each component described below correspond with those shown in Figures 3.1 - 3.4. A beam of white light originates from an Arald Quartz Halogen Lamp (40) which utilizes a 1000 watt tungsten filament and an optional rear mirror assembly to increase the output light intensity. A condenser cooling transformer is connected to the lamp power line and it stabilizes the light intensity reaching the monochromator (41). A condensing lens (LPS 7) is used to collect the radiation and focus the beam uniformly onto the entrance of the monochromator slit. The beam of white light passes through an aluminum cylinder with a copper water cooling system (42) which helps dissipate the heat developed from the high intensity light source.

The Arald grating monochromator (model #77445) runs a 1000 Line ruled grating which is driven by an Arald stepper motor (43). The stepper motor is mounted onto the shaft of the ruled grating and electrically connected to a stepper motor controller (44) within a DMAC crate (Kelley 4004) and controlled by an IBM PC (45). The optical layout of the monochromator is shown in Figure 3.2. White light passes through a Fan Fixed slit (46) is reflected from two mirrors and

then unabsorbed by the grating. This light is then reflected from two additional mirrors and exits through a lens slit. The bandwidth is adjustable through interchangeable fused silica (FS) which can range from 1 to 10 nanometers.

Monochromatic light enters the microscope which is installed as shown through slit in Figure 2.2. The brightfield vertical illuminator (40) is equipped with field and aperture diaphragms which are used in conjunction with a brightfield objective (41) to focus the monochromatic light onto a specimen mounted on the specimen stage (42). The objective used is a 60 Plus 400 high performance glass objective with a numerical aperture of 0.4 and a working distance of 1mm. Ideally corrected optics results in the complete elimination of ghost images and artifacts produced by the half mirror (40) of the brightfield vertical illuminator. The reflected light from the specimen goes through the half-mirror, a tube lens (410) and field photo aperture (411) before entering the photographic unit (412). Within the photographic unit the reflected light is directed to the aperture (404) of the entrance of the photomultiplier tube (403). The aperture determines the area on the surface of the specimen which will be analyzed. A 1 mm diameter aperture results in an analyzed area of 800  $\mu$ m in diameter. A prism is located within the photographic unit to direct the light to either the photomultiplier tube, the camera (402) or to a focusing telescope allowing alignment of the area to be analyzed or photographed.

The photomultiplier tube detects radiant energy in the ultraviolet, visible and near infrared regions of the electromagnetic spectrum. An RCA 4820 photomultiplier tube with an RCA 6P 1000 high voltage power supply (405) are used in this system. The direct current (DC) input

voltage required by the PM 104B supply is supplied by a Tripp Lite 50 power supply (X17) with a 10 A with 50 output voltage. The photomultiplier gain was controlled by the high voltage power supply which provides a regulated output voltage (-100 to -3000 volts) that was controlled by a potentiometer (X18). As the gain of the photomultiplier tube was increased, the dark current was also increased. Typical values of the dark current were between 0.1nA to 0.5nA. The analog output signal from the photomultiplier tube whose voltage range from 1 to 100mV was input to a Galaxy 488 integrating preamplifier (X19) for digital output to the computer. The photodiode used is a SGM detector which exhibits a spectral range between 350nm and 850nm with a spectral sensitivity as shown in Figure 3.4. Response curves were not available for the monochromator for the light source, thus it was necessary to check the spectral sensitivity of the GDM with reference spectra. Silver and silicon were used to obtain reference curves which were compared with reference data to determine the sensitivity of the optical monochromator. The range for optical use was between 350nm and 750nm.

An IBM-PC equipped with a National Instruments 1602-160 interface board is used to communicate with the Galaxy preamplifier and the Galaxy 488B-1000 which houses the Stanford Engineering stepper motor controller and the COMAC to 1602-160 interface (X21). The program, written in IBM Basic runs both COMAC and 488 commands, and is listed Appendix B. The stepper motor is controlled by the stepper motor controller which receives COMAC commands from the COMAC to 1602 interface. These commands are used to step the monochromator every 10nm (1000) between 350nm and 750nm. The program (see Appendix A) collects

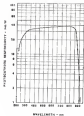


Figure 3-4 Typical response curve for the GaAs photodiode in the 614-4800 photomultiplier tube

data from the piezometer by taking the average of 8 readings from the piezometer starting at 400ms, storing the digital value in a file, then stopping the water flow and repeating the data collection and storage until the water reaches 140ms. The stopper water is programmed to stop back to 100ms that is 400ms to account for any backlash. The 400 is then ready for another scan between 400ms and 140ms or any region within that range. The entire scan flow repeating to end takes 5 minutes. The values for acceleration, deceleration, velocity, and maximum speeds of the stopper water can be set by programming on the front panel of the stopper water controller. Thus allowing the time to complete a scan. The data from each scan is stored in a file on a floppy disk. An additional step in order to obtain reflectance curve of a specimen is to measure the reflected intensity of the single crystal (SC standard),  $I_{\text{std}}$  (single crystal (SC) just prior to measuring the reflected intensity of the specimen,  $I_{\text{spec}}$ ) in air. Knowing  $I_{\text{std}}$ ,  $I_{\text{spec}}$  and  $R_{\text{std}}$ , the value of  $R_{\text{spec}}$  can then be calculated according to:  $R_{\text{spec}} = I_{\text{spec}} (R_{\text{std}} / I_{\text{std}})$ . This calculation is done on the IBM-PC through MPDS 103 which updates the files stored for reflected intensity. Each correct value are stored at each step in a file which is also reported to MPDS and is calculated from the reflected intensities of the specimen and standard prior to calculating the percent reflectance. Percent reflectance as a function of wavelength is graphed with the capabilities of MPDS. An illustration of the results of the above procedure is shown in Figure 5.5. The specimen was freshly fractured bulk chalcopyrite which prior to fracturing had been heated at 300°C for 1 hour. Analysis performed on fractured surface revealed a few minutes

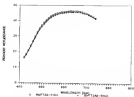


Figure 3.8 Reflectance curves measured from G8 taken sequentially 10 minutes apart (page 8 starts measured plus sign) to determine the stability of the instrument.

to first align the specimen so that a 30° flat area was normal to the optical axis of the microscope. The fractured area was not exposed to air during testing. The surface of a fresh fractured area in the bulk was not affected by the heat treatment and is equivalent to an abraded specimen freshly fractured in air. Ten scans were taken to determine the visibility of the instrument, the first involved focusing a flat area and focusing. The second scan was done immediately after the 40 minutes, Figure 3.85 first scan, with only a small delay due to shocking the area and microscope focus between the two scans. The reflectance curves were found to be equivalent with small changes most likely due to fracture in air. The visibility was also demonstrated by observing that the dark current measured in all scans was constant and independent of time.



## CHAPTER 4 RESULTS

This chapter contains the experimental results on several chalcogenide specimens which were subjected at 85°C, 100°C, or 150°C in laboratory air as a function of time. The experimental results were derived from RPS, ATR, and DR data. A thin film reflectance model was used to calculate reflectance curves based upon the film geometry and composition data obtained from RPS and ATR. Survey scans of the painted specimens and depth profiling through the film layers with ATR and RPS were used to obtain information on the film geometry and composition. Reflectance data further defined the film thickness, composition, and geometry when experimental data were compared with calculated reflectance curves. This data collection procedure allowed a number of possible compounds which could not be uniquely characterized with ATR and RPS to be tested by comparing the calculated reflectance curves after varying the compounds, their thickness, and the film structure spatial geometry with experimental reflectance curves.

A summary of the chalcogenide specimens analyzed is shown in Table 4.1. Of interest is their microstructural origin and the presence or absence of delamination (which is designated with a T for present or an N for not). Analysis done on fractured versus polished specimens is designated as F and P, respectively, while a specimen received in an available form was designated with an M. Specimen heat treatment schedules are given for each temperature.

Table 4.1

Summary of x-ray diffraction specimens analyzed. Their origin, presence of inclusions, and heat treatment temperature and time.

Specimen	Matrix	Inclusions	Treatment	Time(h)
80	La Bore	Y	33°C, P	.....
81	Bottle	Y	33°C, P	.....
82	La Bore	Y	33°C, P	.....
83	Bottle	Y(Ca <sub>2</sub> Si)	33°C, P	.....
84	La Bore	Y	33°C, P	.....
C	La Bore	Y	33°C, P	.....
88F	La Bore	Y	33°C, P	.....
CA	La Bore	Y	33°C, P	.....
88Gnd	La Bore	Y	33°C, P	.....
87	La Bore	Y	33°C, P	.....
88	La Bore	Y	33°C, P	.....
89	La Bore	Y	33°C, P, J	.....
90	La Bore	Y	33°C, P	.....
91	Bottle	Y(Ca <sub>2</sub> Si)	33°C, P	.....
92	La Bore	Y	300°C, P	0
93	La Bore	Y	300°C, P	1.0
94	La Bore	Y	300°C, P	2.0
95	La Bore	Y	300°C, P	33.0
96	Bottle	Y(Ca <sub>2</sub> Si)	300°C, P	0.0
97	La Bore	Y	300°C, P	0.0
98	La Bore	Y	300°C, P	0.0
88F	La Bore	Y	300°C, P	0.0
100	La Bore	Y	300°C, P	0.0
99	La Bore	Y	300°C, P	0.0
99	La Bore	Y	300°C, P	0.0
101	La Bore	Y	300°C, P	0.0
102	La Bore	Y	300°C, P	0.0
103	La Bore	Y	300°C, P	0.0
104	La Bore	Y	300°C, P	0.0
105	La Bore	Y	300°C, P	0.0
106	La Bore	Y	300°C, P	0.0
107	La Bore	Y	300°C, P	0.0
108	La Bore	Y	300°C, P	0.0
109	La Bore	Y	300°C, P	0.0
110	La Bore	Y	300°C, P	0.0
111	La Bore	Y	300°C, P	0.0
112	La Bore	Y	300°C, P	0.0
113	La Bore	Y	300°C, P	0.0
114	La Bore	Y	300°C, P	0.0
115	La Bore	Y	300°C, P	0.0
116	La Bore	Y	300°C, P	0.0
117	La Bore	Y	300°C, P	0.0
118	La Bore	Y	300°C, P	0.0
119	La Bore	Y	300°C, P	0.0
120	La Bore	Y	300°C, P	0.0
121	La Bore	Y	300°C, P	0.0
122	La Bore	Y	300°C, P	0.0
123	La Bore	Y	300°C, P	0.0
124	La Bore	Y	300°C, P	0.0
125	La Bore	Y	300°C, P	0.0
126	La Bore	Y	300°C, P	0.0
127	La Bore	Y	300°C, P	0.0
128	La Bore	Y	300°C, P	0.0
129	La Bore	Y	300°C, P	0.0
130	La Bore	Y	300°C, P	0.0
131	La Bore	Y	300°C, P	0.0
132	La Bore	Y	300°C, P	0.0
133	La Bore	Y	300°C, P	0.0
134	La Bore	Y	300°C, P	0.0
135	La Bore	Y	300°C, P	0.0
136	La Bore	Y	300°C, P	0.0
137	La Bore	Y	300°C, P	0.0
138	La Bore	Y	300°C, P	0.0
139	La Bore	Y	300°C, P	0.0
140	La Bore	Y	300°C, P	0.0
141	La Bore	Y	300°C, P	0.0
142	La Bore	Y	300°C, P	0.0
143	La Bore	Y	300°C, P	0.0
144	La Bore	Y	300°C, P	0.0
145	La Bore	Y	300°C, P	0.0
146	La Bore	Y	300°C, P	0.0
147	La Bore	Y	300°C, P	0.0
148	La Bore	Y	300°C, P	0.0
149	La Bore	Y	300°C, P	0.0
150	La Bore	Y	300°C, P	0.0
151	La Bore	Y	300°C, P	0.0
152	La Bore	Y	300°C, P	0.0
153	La Bore	Y	300°C, P	0.0
154	La Bore	Y	300°C, P	0.0
155	La Bore	Y	300°C, P	0.0
156	La Bore	Y	300°C, P	0.0
157	La Bore	Y	300°C, P	0.0
158	La Bore	Y	300°C, P	0.0
159	La Bore	Y	300°C, P	0.0
160	La Bore	Y	300°C, P	0.0
161	La Bore	Y	300°C, P	0.0
162	La Bore	Y	300°C, P	0.0
163	La Bore	Y	300°C, P	0.0
164	La Bore	Y	300°C, P	0.0
165	La Bore	Y	300°C, P	0.0
166	La Bore	Y	300°C, P	0.0
167	La Bore	Y	300°C, P	0.0
168	La Bore	Y	300°C, P	0.0
169	La Bore	Y	300°C, P	0.0
170	La Bore	Y	300°C, P	0.0
171	La Bore	Y	300°C, P	0.0
172	La Bore	Y	300°C, P	0.0
173	La Bore	Y	300°C, P	0.0
174	La Bore	Y	300°C, P	0.0
175	La Bore	Y	300°C, P	0.0
176	La Bore	Y	300°C, P	0.0
177	La Bore	Y	300°C, P	0.0
178	La Bore	Y	300°C, P	0.0
179	La Bore	Y	300°C, P	0.0
180	La Bore	Y	300°C, P	0.0
181	La Bore	Y	300°C, P	0.0
182	La Bore	Y	300°C, P	0.0
183	La Bore	Y	300°C, P	0.0
184	La Bore	Y	300°C, P	0.0
185	La Bore	Y	300°C, P	0.0
186	La Bore	Y	300°C, P	0.0
187	La Bore	Y	300°C, P	0.0
188	La Bore	Y	300°C, P	0.0
189	La Bore	Y	300°C, P	0.0
190	La Bore	Y	300°C, P	0.0
191	La Bore	Y	300°C, P	0.0
192	La Bore	Y	300°C, P	0.0
193	La Bore	Y	300°C, P	0.0
194	La Bore	Y	300°C, P	0.0
195	La Bore	Y	300°C, P	0.0
196	La Bore	Y	300°C, P	0.0
197	La Bore	Y	300°C, P	0.0
198	La Bore	Y	300°C, P	0.0
199	La Bore	Y	300°C, P	0.0
200	La Bore	Y	300°C, P	0.0

### Natural Isotopes in Absolute

#### Brushy-Polluted, Freshly-Exposed, And Unaltered Specimens

Exposure conditions spectra. Spectra from unaltered specimens of chrysotile analyzed with XPS are shown in Figure 4.1 for a fresh specimen (94), with copper sulfate delamination. The spectra for the three specimens with well defined delamination were equivalent. The S 2p line observed in  $L_{23}VV$  and Fe  $L_{23}VV$  Auger lines are known to be insensitive to changes in the chemical state of the element. They were observed at the same binding energy in all three specimens. Although the Fe(2p3/2)) line was not clearly detectable in the two leached specimens it was observed in the bulk specimen (Figure 4.2). This is most likely due to a contamination layer at the surface in the leached specimens. The Cl 2p line was observed in all three specimens at 199 eV which is characteristic of a sulfate. The S 2s and the Cu(2p3/2)) spectra were observed in all specimens and are shown in Figure 4.3. The S 2s line was at the same binding energy in all three specimens. Specimen 94 had the lowest Cu(2p3/2)) intensity with a binding energy between that of specimen 92 and specimen 93. The Cu(2p3/2)) line for specimen 92 was at a lower binding energy (approximately 1 eV) as compared to specimen 93 but shared the highest intensity of the three specimens. No Cu satellite shake up peaks were observed. The binding energy of the Cu(2p3/2)) line was consistent with a sulfate compound (100-105). The C 1s and O 1s peaks were observed in all spectra and resulted from the polluting atmosphere and surface reaction upon exposing suboxide samples to laboratory air. While the Ti 2p line was observed at times it was not observed in all spectra and its peak was not detected in these specimens. The Si 2p line when present is most likely due to the

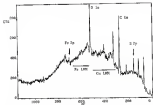


Figure 4.1 XPS survey scan for a natural chlorophyllin specimen from water [10] with  $\text{Ca}_2\text{F}_2$  detection.

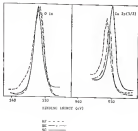


Figure 4.6 High resolution EPD spectra for selected absorption systems for the O Ia and the Fe I(4471) lines for systems SF, SE, and SC

was used in the polishing procedure (see Chapter IX) and from the presence of chloride regions (present in paper) within the large area covered with BPS (about 300  $\mu$ m diameter). A 5  $\mu$ p line from anode (approximately 100 keV) was not observed in any of the spectra for polished specimens either immediately after polishing or after mounting for several weeks in laboratory air. A summary of the range of energies for iron, copper, and copper compounds is shown in Table 4.2.

Table 4.2

Binding energy ranges from XPS characterization of Fe 5p, S 2s, and Cu 2p peaks used throughout the text

Fe 5p	iron oxide	710-707 eV	711-708 eV
	iron hydroxide	711-707 eV	712-707 eV
	iron sulfide	712-708 eV	712-708 eV
S 2s	oxide	228-227 eV	229-228 eV
	hydroxide	229-227 eV	229-228 eV
	sulfide	229-227 eV	229-228 eV
Cu 2p	copper sulfide	932-927 eV	933-927 eV
	copper hydroxide	933-927 eV	933-927 eV

**Super-resolution spectra.** A freshly polished Fe wire specimen (100) was used for super-pixel analysis (this sample was later heated at 100°C). An super-spectrum from charge-coupled went to a Sci-Pixel 5000 after five selected spectra averaging, is shown in Figure 4.10. The main elements detected were Cu (904eV), Fe (709eV), and S (159eV) with C (285eV) as a carbon contaminant. Low energy Cu L<sub>2,3</sub> and Fe L<sub>2,3</sub> peaks were observed at 932eV and 484eV respectively. No copper was detected on the etched and charge-coupled surface (includes-free Fe wire specimen

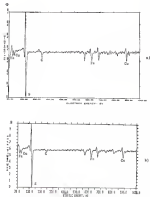


Figure 4.9: Scanning EDS point analysis from an selected electrocatalytic specimen after 4 minute reaction time: (a) first EDS point and (b) first EDS point. Peaks of interest are Fe(130), Cu(150), Fe(170), and Cu(200).

[Fig] are freshly polished, then fractured. Both the polished and fractured surfaces were analyzed and the spectra were equivalent to that for a polished area. From specimen BE. The spectrum from the fractured region after five minutes of sputtering is shown in Figure 4.16. Thus, the fractured area analyzed was found to be equivalent to a freshly polished area. The C and D are similar experiments.

Optical microstructural analysis. Chalcopyrite specimens from both the La Jara and Betta deposits were freshly polished according to the procedures outlined in Chapter 3 just prior to obtaining reflectance curves from the optical reflectometer (OR). The La Jara specimens were mostly BF with iron oxide inclusions and copper sulfide inclusions in the form of vesicles and BE as inclusion-free specimens (this specimen was later heated at 800°C - a heated specimen from Betta BE contained copper sulfide inclusions equivalent to those detected in specimen BF). Representative reflectance curves are shown as calculated spectra in Figure 4.16 for chalcopyrite regions in specimens BF, BE, and BE. Calculated reflectance curves are reconstructed as unsmoothed spectra (S<sub>meas</sub> and S'<sub>meas</sub>). The calculated curves are for the two crystallographic orientations of FeS<sub>2</sub> designated as R<sub>1</sub> (S<sub>meas</sub>) and R<sub>2</sub> (S'<sub>meas</sub>) (see Appendix A). Spectroscopic OR curves were obtained for each of the regions, and similar curves were observed for all freshly polished samples independent of the origin. The slight differences observed in the reflectance spectra of Figure 4.16 may result from slight differences in the microtopography of the surface. These differences could result from specimen origin. However, the initial reaction of the surface upon exposure to air can also cause changes in the surface reflectivity (SROR) of a specimen. This has been observed for a number



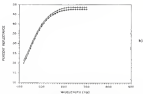
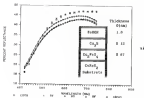


Figure 4 a) Reflectance curves generated with GEN-OP of chalcogenite from its spectrum (001, 010 and 011) (calculated lines) versus calculated versus experimental spectra for films grown epitaxially and b) reference reflectance curves for the two crystallographic orientations (001 and 010) of chalcogenite

of solidi elements (TGMN, HRL, LBRN, HBRN) reflectance coefficients published by the International Mineralogical Association (IMA) (see below) for two Microscopy were plotted to obtain the reference reflectance curve for tetragonal  $\text{CaFe}_2\text{Si}_2\text{O}_8$  (see Figure 4.4a) for the two crystallographic orientations [110 $\text{CaFe}_2\text{Si}_2\text{O}_8$ ] (h<sub>1</sub> [secondary]) and h<sub>2</sub> [primary]; the two orientations were obtained from a polycrystalline chalcophyllite specimen polished with etchant oxide. A large grain within the specimen was chosen and the reflected intensity was measured as the specimen was rotated around the optical axis until a minimum was obtained. The reflectance curve obtained at this orientation was for h<sub>1</sub>. The specimen was then rotated ninety degrees to obtain h<sub>2</sub>. Reflectance curves for a freship fractured to three specimens, CA, and a bulk specimen, BHP that was heat treated, then freship fractured are shown in Figure 4.5. These curves showed an overall equivalent shape with higher percent reflectance between 400nm and 700nm as compared to those shown in Figure 4.4. Their wavelength and reflectance minima and maxima values follow for  $\lambda_{\text{min}}$  and 490 (specimen CA) and 500 (specimen BHP) for  $\lambda_{\text{max}}$ .

Mineral Identification. Electron probe microanalysis (EPMA), in conjunction with AEM and SEM, was used to examine the phases found in a bulk to bulk (BX) and bulk (BX) specimen. An optical photomicrograph representative of a bulk chalcophyllite specimen is shown in Figure 4.6. For specimen BX (Bette) showing minerals (copper sulfide and born oxide) within the bulk chalcophyllite matrix. X-ray maps (200pm x 200pm) for elemental Fe, Cu, and S are shown for specimen BX in Figure 4.7. The chalcophyllite region had Cu, Fe, and S present, the region immediately in contact with chalcophyllite had only Cu and S. The iron sulfide region is

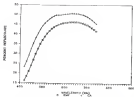


Figure 4.8 Reflectance spectra recorded with ORS for freshly deuterated specimens CA (top trace) and MB (bottom).



Figure 4.8 Optical photomicrograph of a natural specimen of biotite schists (B) with chlorite (C) inclusions originating from biotite (B).

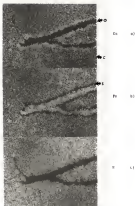


Figure 4.1 B-scan elemental maps for Beller system (a) Ca (b) Fe, and (c) S. Maps have dimensions of 100µm x 50µm. Regions which can be identified are: C = chalcopyrite, S = Copper sulfide, and G = glass matrix

contact with the copper sulfide region showed a high Fe signal with very low signals from Cu and S. Qualitative maps were consistent with  $\text{CuFeS}_2$  as the bulk material and Cu as the mineral in direct contact with  $\text{CuFeS}_2$ . Data from AED (see Figure 4.1a) confirmed that the iron region had Fe and S as its main constituents. The low energy Fe  $L_{2,3}$  peak was split into two peaks that have been associated with an iron oxide (PITAK-PAUL) and to this case with  $\text{FeO}$  (TOSAKI). The presence of Cu and S in the Cu-sulfide region (see Figure 4.1b) and Cu, Fe, and S in the chalcopyrite region was confirmed with AED data. Data from EDX showed that arsenic, silver, selenium, and tellurium were below the detection limits of 0.006%, 0.003%, 0.001%, and 0.001%, respectively in chalcopyrite.

Reflectance curves from the three phases (chalcopyrite, copper sulfide, and iron oxide) in specimens 20 and 21 are shown in Figure 4.2. They correlate with the maps acquired with SEM with the exception of the copper sulfide region in the latter specimen (21). The reflectance curves in Figure 4.2a were consistent with that for a chalcopyrite region (compare with Figure 4.1). The copper sulfide region was not found in an area of at least 10  $\mu\text{m}$  in diameter and thus could not be analyzed in specimen 20. The reflectance curve for the copper sulfide region in specimen 21 is shown in Figure 4.2b and also compared with the reference reflectance curves for  $\text{FeS}$  and  $\text{FeS}_2$ . The reflectance curves in Figure 4.2c were from the iron sulfide region and also compared with the  $\text{FeS}$  reference reflectance curves for goethite ( $\text{FeOOH}$ ) and hematite ( $\text{Fe}_2\text{O}_3$ ) and were consistent with goethite. The two corresponding atomizations  $R_1$  and  $R_2$  are shown in Figure 4.3a for goethite and hematite. The

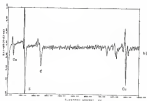
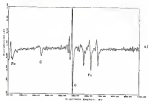


Figure 4-2 X-ray photoelectron spectra for specimen 82; (a) iron oxide (Fe<sub>2</sub>O<sub>3</sub>) and (b) copper sulfate (CuSO<sub>4</sub>)

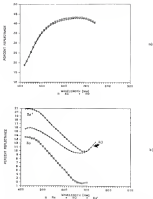
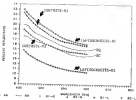


Figure 8.8 Reflection curves for (a) *Rhodospirillum rubrum*, specimens AB and BC, 10 crystals, specimen BQ and reference data for the crystal orientation (for BQ 1), and (b) similar for specimens AB and BQ versus reference data for position and degradation for the crystal orientation (BQ 100).





reflectance curves in the visible region for goethite has been shown to be similar to limonite (TJ90N) which is another iron oxide mineral. Limonite is actually coprecipitated like goethite or lepidocrocite along with hematite and additional water (20 to 100 by weight).

Optical data from the reflectance curves will be discussed by referring to reflectance ratios,  $R_{\text{max}}$ , in percent (%) and their corresponding wavelengths,  $\lambda_{\text{max}}$ , in microns ( $\mu$ ). Similarly a reflectance minimum,  $R_{\text{min}}$ , and the corresponding wavelength,  $\lambda_{\text{min}}$ , will be referred to throughout this study. Data for the reflectance ratios and ratios from different specimens are shown in Table 4.3.

Table 4.3  
Wavelength and reflectance ratios and ratios for selected specimens from which specific ratios in each specimen.

SPECIMEN	Name	$\lambda_{\text{max}}$	$\lambda_{\text{min}}$	$R_{\text{max}}$	$R_{\text{min}}$
Visible region					
20	Go. hemat.	400	425-0		
23	hemo	400	425-0		
28	Go. hemat.	400	440-0		
31	hemo	400	440-0		
37	Go. hemat.	400	440-0		
44	Go. hemat.	400	440-0		
50F	hemo	400	440-0		
Faded region					
55	Go. hemat.	400	475-0	440	22-0
		400	480-0		
		400	485-0		
56	hemo	440	500-0	440	14-00
		440	475-0		
		440	500-0		
		440	505-0		
UV region					
58	hemo	440	10-0	470	0-02

### Exposure of Chalcopyrite in Laboratory Air

EXPERIMENTAL PROCEDURE: An inclusion-free  $\text{Cu}$  foil specimen, 10. mm polished then fractured in order to analyze both a polished and a fractured area on the same sample. The specimen remained in laboratory air for 15 days before analyzing with EPMA.

In analyzing the fractured area, aluminum foil was used to mask a small area of the specimen for analysis. Visual observation of the fractured surface showed one surface tarnishing with some areas bright gold and other areas being dull orange-yellow in color. The area masked included areas that were lightly and heavily tarnished; therefore EPMA data are simultaneously collected from both areas. Auger point analysis (see next section) were taken separately on these two areas.

The EPMA survey spectra from the polished area was equivalent to those taken from other chalcopyrite specimens. A thin iron oxide layer is detected after polishing with diamond. The survey spectra for the fractured area of the specimen showed the presence of a sulfide compound in addition to a sulfide compound as shown in Figure 4.10 for the  $\text{S}_{K\alpha}$  spectrum. Copper was present in the  $\text{Cu}^{2+}$  state on fractured surfaces as indicated with EPMA by a weak satellite shake-up peak at 940 eV (see peak labeled A in Figure 4.10). The detection of a sulfide sulfur ( $\text{S}_{23.0\text{eV}}$ ) and the  $\text{Cu}^{2+}$  (labeled peak B at 900 eV in Figure 4.10) suggests that a copper sulfide is present. Copper sulfide compounds are found in nature during leaching and during high temperature roasting. In contrast, the  $\text{Cu}_{K\alpha}$  peak was only weakly detected from the polished as compared to the fractured surface of the same sample which suggests that an iron oxide surface contamination layer was present at a thickness close to the escape depth of the  $\text{Cu}$  photoelectrons.

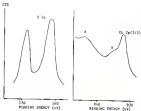


Figure 4.18 XPS survey spectra of a fractured specimen of chalcophyllite originating from Le Barre and containing no inclusions. The  $S\ 2p$  is approximately 168 eV indicative of a sulfide while that at 285 eV indicates a sulfate. For the  $S\ 2p\ 2/3$  peak, peak  $s$  and the shake-up peak labeled  $a$  indicate also the presence of a sulfide.

The fractured specimen is not a dense fracture in the sense of an oxidized surface, but rather should be categorized as creating free galvanic anodes along a crack. The polished specimen showed an Fe(II)/Fe(III) intensity ratio that was larger than for the truly fractured area by a factor of 2. This suggests that the polished surface is iron-rich (free oxidation of iron) while the fractured galvanic surface is copper-rich (due to leaching conditions).

Auger Electron Spectroscopy. Auger point analysis was used to analyze the other half of specimen 16 (the base, inclusion-free substrate) fractured in air. To determine if freshly fractured specimens showed spectra equivalent to freshly polished surfaces. The exact probe of interest was Cu(2p), Fe(2p), S(2s), and S(2p). Carbon(1s) was found on the surface as a contaminant which was removed after 2.5 minutes of sputtering. After fracturing the specimen and analyzing the surface with Auger point analysis the specimen was allowed to sit in laboratory air for 30 days. Auger point analysis was employed again after 30 days to determine the extent of oxidation. This half of specimen 16 showed similar fractured areas as did the other half used for XPS analysis. General points in the fractured area were analyzed and found to be either Fe and S rich or Fe and S rich. The Fe and S rich regions would be consistent with the copper sulfate. Good free Fe on fractured surfaces. The iron and copper rich regions would be consistent with the observation of Fe(II)/Fe(III) probe with XPS since the area of analysis for XPS is approximately 300 Å in diameter. Thus, although there are some notably furnished after fracturing, there are other areas with visible tarnishing detected. It was these areas that were compared with the polished areas after 30 days in laboratory air.

The Auger spectra of the polished (Figure 4.11) and fractured (Figure 4.12) unspattered areas were found to have approximately peak shapes and relative peak heights. After sputtering for 5 minutes with argon, the fractured area is free of oxygen while the polished area shows a small oxygen peak. After 5 minutes of sputtering no oxygen is detected in either the fractured or polished area. Thus, both areas showed the formation of a thin iron oxide layer.

Auger point analysis from two areas of specimen 10 (the two natural oxidation) was employed to obtain a depth profile of the film formed after exposure to laboratory air for approximately 4 months. A 14 minute sputter depth profile for area 1 is shown in Figure 4.13a and for area 2 in Figure 4.13b. Area 1 was a red/purple region while area 2 was a dark amorphous region. The surface of both areas consisted mainly of Fe and O with C. After 30 minutes of sputtering to remove C, an iron oxide was detected from the presence of two lines at 450V and 500V (2.5eV peak energy difference) [FeO<sub>2</sub>FeO] as shown in Figure 4.14. The peak energy difference between the two low energy peaks are consistent with  $\alpha$ -Fe<sub>2</sub>O<sub>3</sub> (7-5eV) and FeO (7-5eV) [FeO] - With further sputtering the peak energy difference decreased and approached that of Fe<sub>2</sub>O<sub>3</sub> (4.5eV-5.5eV). The presence of even Fe<sub>2</sub>O<sub>3</sub> at the surface of the outer Fe<sub>2</sub>O<sub>3</sub> layer will lead to an increase in the peak energy difference from 5eV to 5eV [FeOFeO]. The low energy Fe peak at 510V was not observed until after the two low energy peaks decreased in amplitude which occurred after 2.5 minutes of sputtering. After 10 minutes of sputtering (Figure 4.15b) the Fe 510V peak is consistent with elemental iron. Although the C line decreased drastically after 5.5 minutes of sputtering, some carbon was detected throughout the film.

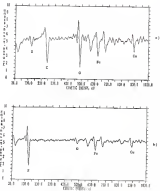


Figure 4-11) XPS spectra for specimen Fe isolated and treated at 30°C for 30 days: a) spectra for unspattered surface and b) spectra after 2 minutes spattering

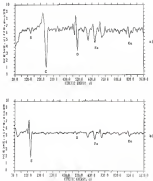
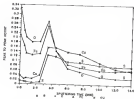
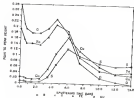


Figure 4.10 XPS spectra for specimen 5a. Etched and reacted at 85°C for 25 days: (a) spectra for unetched surface and (b) spectra after 2 minutes etching.





a)



b)

Figure 4.10 Auger spectra depth profile for two series of samples (a) initially deposited in air for 8 months (a) red (single scan) and (b) dark orange (scan area).

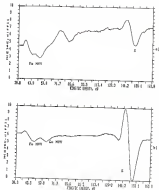


Figure 4-14 AES curves for specimen 36 reacted at 22°C for 8 months: a) Fe MYV line associated with an iron oxide and b) Fe and Ga MYV lines associated with both oxides.

There is a maximum in the Fe, Ni, Cu, and S peak to peak heights at the oxide/metallic interface which is believed to result from charging. The Cu/S ratio for the red-purple area (see Figure 4.12a) is closer to the surface (thinner iron oxide) than for the dark orange-brown area. After sputtering before sputtering detected a small Cu peak in the red-purple area while no Cu peak was detected in the dark orange-brown region suggesting that the Cu is closer to the surface or has a mixed heterogeneous layer with the iron oxide. Between 5 and 10 minutes of sputtering, the  $\text{Fe}(\text{HfO})/\text{Fe}(\text{HfO})$  and  $\text{Fe}(\text{HfO})/\text{Hf}(\text{HfO})$  ratios are  $> 1.0$  for the red-purple region while between 7 and 8 minutes the same is true for the dark orange-brown region suggesting a ferritic compound near to the bulk chalcopyrite. After 10 minutes of sputtering S was detected in the red-purple region with a formula of  $\text{Fe}_{1.15}\text{S}_{1.0}$  to  $\text{Fe}_{1.0}\text{S}_{1.0}$  while no oxygen was detected for the dark orange-brown region. The Cu, Fe, and S decreased in intensity to bulk chalcopyrite values while S was not detected after 10 minutes of sputtering ( $\text{FeS}_{1.00}\text{Fe}_{0.1}$ ).

Sputtering was discontinued after 10 minutes. Since no S peak was detected for the red-purple area while not for the orange-brown area it was of interest to see if surface oxidation was different. The formerly red-purple area was associated with a light gold brown color, a brown yellow color which is characteristic of a freshly polished chalcopyrite was associated with the previously orange-brown area. Thus the color observed is due to contributions from the optically absorbing surface compound present and the thickness of the layers. The detection of oxygen may be due to diffusion of oxygen into the bulk via vacancies due to a nonstoichiometric excess of Fe and S at the surface of chalcopyrite. Oxygen diffusion at room temperature has been

reported for 600 crystals [28000] that have an excess of Cd at the surface as a large concentration of surface vacancies which were available to accept. Diffusion of the copper into the bulk via surface vacancies was noticeable after a few days at room temperature. This process could be hastened by raising the temperature. Another possible explanation for the presence of  $\delta$  may be from spitting effects since the area analyzed was immediately adjacent to a proper (colloidal) inclusion.

Examination of the specimen (specimen 2) after 1 year in laboratory air. Specimen 2 appeared in laboratory air (1 year) of an inclusion-free. In here specimen showed a color change (see Figure 4 (b)) from a brown yellow color to a surface with regions which were the Coarse C1. Light golden brown (area B), and dark golden-brown (area A) in color. The wavelength and reflectance values and ratios are shown in Table 2.4. The polishing procedure on this specimen was slightly different than for the other specimens since it was polished in detail. First rather than a 11 mineral oil petroleum ether mixture, then cleaned in ethanol rather than petroleum ether. Additionally, the specimen was embedded in an embedding matrix. While these differences in handling are reported for accuracy, they are not believed to influence the long term oxidation behavior of sample 2 in air. The reflectance curves for specimen 2 after 1 year in air are dramatically distinct from those of a freshly polished specimen or one exposed for a short time in air. The characteristic wavelength  $\lambda_{max}$  associated with the maximum intensity  $R_{max}$  shifted from 610nm (area C) to 710nm (area B) to 770nm (area A) as  $R_{max}$  decreased and the spectrum flattened. The development of a broad  $R_{min}$  over the spectral range measured was observed for curves B and A as

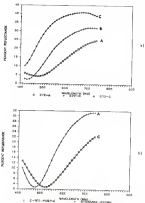


Figure 4: DSC curves for long time anneals at 25°C: a) specimen B (400°C) shows curves A, B, and C (endothermic, the dark green lines, light green lines, and red-purple lines respectively) and b) DSC (endothermic) shows curves A and C (the dark green lines and red-purple lines, respectively).

transmitted to an color  $\lambda_{\text{obs}}$  from freshly collected oligomeric species, however, as the species desolved (curve A compared to B) an increased reflectance at approximately 410nm (blue violet portion of the spectrum) was observed. The violet observed correlated with a decrease in reflectance from the yellow-green portion of the spectrum and an increase from the high and low wavelength portion of the spectrum. Shifts of  $\lambda_{\text{obs}}$  to longer wavelengths will be shown to correlate with a higher reaction product input.

After 8 minutes in laboratory air, inclusion-free spectrum 1B was analyzed with OM at the same two wavenumbers with AHS (see Figure 4.13 and Figure 4.14). The wavelength and reflectance scales and slopes were similar to those of the orange-brown region on spectrum 1 (see Table 4.4 and Figure 4.10, curve A). However, a red-purple region (Figure 4.10, curve B) was observed within spectrum 1B (see Table 4.5), and no more further shifts to longer wavelengths was measured for this region as compared to the dark orange-brown region of spectrum 1 and the dark orange-brown region of spectrum 1B. Thus, some variation in color is observed even in inclusion-free spectra which is dependent on the species and not the inclusion.

Table 4.5  
Wavelength and reflectance scales and slopes for oligomeric regions accurately isolated in air

Spectrum	Observed area	$\lambda_{\text{obs}}$	$\lambda_{\text{obs}}$	$\lambda_{\text{obs}}$	$\lambda_{\text{obs}}$
1B	Top	40.0	650	410	10.0
	Light orange-brown	84.0	780	410	0.0
	Dark orange-brown	94.0	770	415	0.0
1C	Dark orange brown	93.0	760	415	0.0
	Red-purple			520	0.0

A 40 Watt spectrum (C) was fractured in air and analyzed with OM

Immediately after fracturing. The reflectance curves for specimen C are shown in Figure 4 (b) at 0 hours, 10 hours (5 days) and 17 days after fracturing. A decrease in the overall percent reflectance was observed for the designed feature at  $R_{\text{avg}} = L_{\text{avg}}$ . A shift from  $L_{\text{avg}} = 0.05$  to  $L_{\text{avg}} = 0.04$  was observed with a decrease in  $R_{\text{avg}} = 0.05$  to  $R_{\text{avg}} = 0.04$ . Comparing data for freshly fractured surfaces in Figure 4 (b) to those of Figure 4 (a), it is obvious that the fractured surface on specimen C was already oxidized. In fact, the reflectance curves can be compared with those of specimen C coated for 1.5 years (see Figure 4 (b) and Table 4 (4)). Consequently the small shift observed after 17 days in air is probably due to the slower reaction rates of the previously oxidized surface. In addition, copper sulfide has been observed upon fractured surfaces (see Figure 4 (b)). Thickening of a copper sulfide would decrease the overall percent reflectance with little to no shift in  $\lambda_{\text{avg}}$  since the sulfide is nonabsorbing.

Calculated reflectance curves for copper. A reflectance model was used to calculate optical reflectance curves of an absorbing substrate covered with multiple thin layers of absorbing materials (see Appendix A). Reflectance curves with multiple homogeneous thin layers on the surface were modeled and compared with experimental curves. Data obtained from AM and UV were utilized to help narrow the possible compounds and their thicknesses. The value layer is an oxide/sulfide composed of iron with an underlying copper compound layer and a copper-rich sulfide layer in contact with the bulk substrate. The copper compound is in the  $\lambda$  region where UV data did not have the sulfate show-up peak for Cu(II). This value state is consistent with a number of copper compounds, especially sulfides, since a sulfide

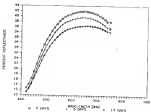
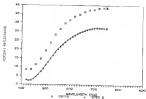


Figure 8-18 Reflectance curves for specimen 8 fractured in air and immersed immediately (curve a) and as a function of time in laboratory air, 3 days (curve b) and 17 days (curve c)



peak at a binding energy which is characteristic of a copper sulfide was also detected. These include covellite ( $\text{CuS}$ ), chalcocite ( $\text{Cu}_2\text{S}$ ), bornite ( $\text{Cu}_5\text{FeS}_4$ ), and chalcophyllite ( $\text{CuFeS}_2$ ) all of which are in the +1 valence state. The layer in contact with chalcophyllite is modeled as copper-rich bornite, justified in part by the fact that chalcophyllite and bornite may be found together in nature [PRAHR]. The outer layer was modeled with  $\text{Fe}_2\text{S}_3$  and the intermediate layer with a copper sulfide as shown schematically in Figure 4.12 through Figure 4.16. The thickness of the  $\text{CuS}$  or the  $\text{Cu}_2\text{S}$  intermediate layer was much thinner than the  $\text{Fe}_2\text{S}_3$  outer layer and the  $\text{Cu}_5\text{FeS}_4$  layer in contact with chalcophyllite. It is known [PRAHR] for films of 100Å or less in thickness that the reflectance curve can be calculated for either two homogeneous layers or one heterogeneous layer with the same resultant curve. In addition, changing the optical geometry of the layers and placing the iron oxide layer between the copper sulfide and the bornite layer had no effect on the calculated reflectance curves. Thus, either a heterogeneous outer layer structure or an outer layer of copper sulfide with an intermediate iron oxide layer would allow simultaneous detection of both the sulfides and the iron oxide as indicated from XPS data. Calculated curves for films of approximately 400Å, 400Å, and 400Å are shown in Figure 4.17, Figure 4.18, and Figure 4.19 respectively. The calculated and experimental reflectance curve shapes were most consistent when the series of layers and compounds shown schematically in Figure 4.12 through Figure 4.16 were utilized. The ratio of thicknesses were obtained by balanced chemical equations discussed in Chapter 3.

These data demonstrate that the native iron oxide and copper sulfide layers are thin and can be modeled with either the iron oxide or the



a)

	Thickness $\delta$ (nm)
$\text{Fe}_2\text{O}_3$	6.0
$\text{Fe}_2\text{O}_3$	0.0
$\text{Fe}_2\text{O}_3/\text{Fe}_2\text{O}_3$	6.0
$\text{CuFeO}_2$	
Substrate	

b)

Figure 6-17

Experimental (curve a) versus calculated (curve b) reflectance curves for specimen 8 coated at 325°C. for 1 hour. a) 400 curves and b) schematic diagram of the film layers and thicknesses.

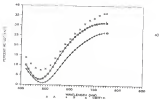
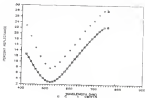


Figure 4.1b Schematic diagram of the film layers and range of thicknesses.



$\text{Fe}_2\text{O}_3$
$\text{Cu}_2\text{O}$
$\text{Cu}_2\text{FeS}_4$
$\text{CuFeS}_2$
Substrate

Thickness  $\mu$  (nm)

0.1

0.2

0.3

10

Figure 4-10

Experimental curves (a) versus calculated curves (b) reflectance curves for thickness of 0.1  $\mu$  (c) 0.2  $\mu$  (d) 0.3  $\mu$  (e) 0.4  $\mu$  (f) 0.5  $\mu$  (g) 0.6  $\mu$  (h) 0.7  $\mu$  (i) 0.8  $\mu$  (j) 0.9  $\mu$  (k) 1.0  $\mu$  (l) 1.1  $\mu$  (m) 1.2  $\mu$  (n) 1.3  $\mu$  (o) 1.4  $\mu$  (p) 1.5  $\mu$  (q) 1.6  $\mu$  (r) 1.7  $\mu$  (s) 1.8  $\mu$  (t) 1.9  $\mu$  (u) 2.0  $\mu$  (v) 2.1  $\mu$  (w) 2.2  $\mu$  (x) 2.3  $\mu$  (y) 2.4  $\mu$  (z) 2.5  $\mu$  (aa) 2.6  $\mu$  (ab) 2.7  $\mu$  (ac) 2.8  $\mu$  (ad) 2.9  $\mu$  (ae) 3.0  $\mu$  (af) 3.1  $\mu$  (ag) 3.2  $\mu$  (ah) 3.3  $\mu$  (ai) 3.4  $\mu$  (aj) 3.5  $\mu$  (ak) 3.6  $\mu$  (al) 3.7  $\mu$  (am) 3.8  $\mu$  (an) 3.9  $\mu$  (ao) 4.0  $\mu$  (ap) 4.1  $\mu$  (aq) 4.2  $\mu$  (ar) 4.3  $\mu$  (as) 4.4  $\mu$  (at) 4.5  $\mu$  (au) 4.6  $\mu$  (av) 4.7  $\mu$  (aw) 4.8  $\mu$  (ax) 4.9  $\mu$  (ay) 5.0  $\mu$  (az) 5.1  $\mu$  (ba) 5.2  $\mu$  (bb) 5.3  $\mu$  (bc) 5.4  $\mu$  (bd) 5.5  $\mu$  (be) 5.6  $\mu$  (bf) 5.7  $\mu$  (bg) 5.8  $\mu$  (bh) 5.9  $\mu$  (bi) 6.0  $\mu$  (bj) 6.1  $\mu$  (bk) 6.2  $\mu$  (bl) 6.3  $\mu$  (bm) 6.4  $\mu$  (bn) 6.5  $\mu$  (bo) 6.6  $\mu$  (bp) 6.7  $\mu$  (bq) 6.8  $\mu$  (br) 6.9  $\mu$  (bs) 7.0  $\mu$  (bt) 7.1  $\mu$  (bu) 7.2  $\mu$  (bv) 7.3  $\mu$  (bw) 7.4  $\mu$  (bx) 7.5  $\mu$  (by) 7.6  $\mu$  (bz) 7.7  $\mu$  (ca) 7.8  $\mu$  (cb) 7.9  $\mu$  (cc) 8.0  $\mu$  (cd) 8.1  $\mu$  (ce) 8.2  $\mu$  (cf) 8.3  $\mu$  (cg) 8.4  $\mu$  (ch) 8.5  $\mu$  (ci) 8.6  $\mu$  (cj) 8.7  $\mu$  (ck) 8.8  $\mu$  (cl) 8.9  $\mu$  (cm) 9.0  $\mu$  (cn) 9.1  $\mu$  (co) 9.2  $\mu$  (cp) 9.3  $\mu$  (cq) 9.4  $\mu$  (cr) 9.5  $\mu$  (cs) 9.6  $\mu$  (ct) 9.7  $\mu$  (cu) 9.8  $\mu$  (cv) 9.9  $\mu$  (cw) 10.0  $\mu$  (cx) 10.1  $\mu$  (cy) 10.2  $\mu$  (cz) 10.3  $\mu$  (ca) 10.4  $\mu$  (cb) 10.5  $\mu$  (cc) 10.6  $\mu$  (cd) 10.7  $\mu$  (ce) 10.8  $\mu$  (cf) 10.9  $\mu$  (cg) 11.0  $\mu$  (ch) 11.1  $\mu$  (ci) 11.2  $\mu$  (cj) 11.3  $\mu$  (ck) 11.4  $\mu$  (cl) 11.5  $\mu$  (cm) 11.6  $\mu$  (cn) 11.7  $\mu$  (co) 11.8  $\mu$  (cp) 11.9  $\mu$  (cq) 12.0  $\mu$  (cr) 12.1  $\mu$  (cs) 12.2  $\mu$  (ct) 12.3  $\mu$  (cu) 12.4  $\mu$  (cv) 12.5  $\mu$  (cw) 12.6  $\mu$  (cx) 12.7  $\mu$  (cy) 12.8  $\mu$  (cz) 12.9  $\mu$  (ca) 13.0  $\mu$  (cb) 13.1  $\mu$  (cc) 13.2  $\mu$  (cd) 13.3  $\mu$  (ce) 13.4  $\mu$  (cf) 13.5  $\mu$  (cg) 13.6  $\mu$  (ch) 13.7  $\mu$  (ci) 13.8  $\mu$  (cj) 13.9  $\mu$  (ck) 14.0  $\mu$  (cl) 14.1  $\mu$  (cm) 14.2  $\mu$  (cn) 14.3  $\mu$  (co) 14.4  $\mu$  (cp) 14.5  $\mu$  (cq) 14.6  $\mu$  (cr) 14.7  $\mu$  (cs) 14.8  $\mu$  (ct) 14.9  $\mu$  (cu) 15.0  $\mu$  (cv) 15.1  $\mu$  (cw) 15.2  $\mu$  (cx) 15.3  $\mu$  (cy) 15.4  $\mu$  (cz) 15.5  $\mu$  (ca) 15.6  $\mu$  (cb) 15.7  $\mu$  (cc) 15.8  $\mu$  (cd) 15.9  $\mu$  (ce) 16.0  $\mu$  (cf) 16.1  $\mu$  (cg) 16.2  $\mu$  (ch) 16.3  $\mu$  (ci) 16.4  $\mu$  (cj) 16.5  $\mu$  (ck) 16.6  $\mu$  (cl) 16.7  $\mu$  (cm) 16.8  $\mu$  (cn) 16.9  $\mu$  (co) 17.0  $\mu$  (cp) 17.1  $\mu$  (cq) 17.2  $\mu$  (cr) 17.3  $\mu$  (cs) 17.4  $\mu$  (ct) 17.5  $\mu$  (cu) 17.6  $\mu$  (cv) 17.7  $\mu$  (cw) 17.8  $\mu$  (cx) 17.9  $\mu$  (cy) 18.0  $\mu$  (cz) 18.1  $\mu$  (ca) 18.2  $\mu$  (cb) 18.3  $\mu$  (cc) 18.4  $\mu$  (cd) 18.5  $\mu$  (ce) 18.6  $\mu$  (cf) 18.7  $\mu$  (cg) 18.8  $\mu$  (ch) 18.9  $\mu$  (ci) 19.0  $\mu$  (cj) 19.1  $\mu$  (ck) 19.2  $\mu$  (cl) 19.3  $\mu$  (cm) 19.4  $\mu$  (cn) 19.5  $\mu$  (co) 19.6  $\mu$  (cp) 19.7  $\mu$  (cq) 19.8  $\mu$  (cr) 19.9  $\mu$  (cs) 20.0  $\mu$  (ct) 20.1  $\mu$  (cu) 20.2  $\mu$  (cv) 20.3  $\mu$  (cw) 20.4  $\mu$  (cx) 20.5  $\mu$  (cy) 20.6  $\mu$  (cz) 20.7  $\mu$  (ca) 20.8  $\mu$  (cb) 20.9  $\mu$  (cc) 21.0  $\mu$  (cd) 21.1  $\mu$  (ce) 21.2  $\mu$  (cf) 21.3  $\mu$  (cg) 21.4  $\mu$  (ch) 21.5  $\mu$  (ci) 21.6  $\mu$  (cj) 21.7  $\mu$  (ck) 21.8  $\mu$  (cl) 21.9  $\mu$  (cm) 22.0  $\mu$  (cn) 22.1  $\mu$  (co) 22.2  $\mu$  (cp) 22.3  $\mu$  (cq) 22.4  $\mu$  (cr) 22.5  $\mu$  (cs) 22.6  $\mu$  (ct) 22.7  $\mu$  (cu) 22.8  $\mu$  (cv) 22.9  $\mu$  (cw) 23.0  $\mu$  (cx) 23.1  $\mu$  (cy) 23.2  $\mu$  (cz) 23.3  $\mu$  (ca) 23.4  $\mu$  (cb) 23.5  $\mu$  (cc) 23.6  $\mu$  (cd) 23.7  $\mu$  (ce) 23.8  $\mu$  (cf) 23.9  $\mu$  (cg) 24.0  $\mu$  (ch) 24.1  $\mu$  (ci) 24.2  $\mu$  (cj) 24.3  $\mu$  (ck) 24.4  $\mu$  (cl) 24.5  $\mu$  (cm) 24.6  $\mu$  (cn) 24.7  $\mu$  (co) 24.8  $\mu$  (cp) 24.9  $\mu$  (cq) 25.0  $\mu$  (cr) 25.1  $\mu$  (cs) 25.2  $\mu$  (ct) 25.3  $\mu$  (cu) 25.4  $\mu$  (cv) 25.5  $\mu$  (cw) 25.6  $\mu$  (cx) 25.7  $\mu$  (cy) 25.8  $\mu$  (cz) 25.9  $\mu$  (ca) 26.0  $\mu$  (cb) 26.1  $\mu$  (cc) 26.2  $\mu$  (cd) 26.3  $\mu$  (ce) 26.4  $\mu$  (cf) 26.5  $\mu$  (cg) 26.6  $\mu$  (ch) 26.7  $\mu$  (ci) 26.8  $\mu$  (cj) 26.9  $\mu$  (ck) 27.0  $\mu$  (cl) 27.1  $\mu$  (cm) 27.2  $\mu$  (cn) 27.3  $\mu$  (co) 27.4  $\mu$  (cp) 27.5  $\mu$  (cq) 27.6  $\mu$  (cr) 27.7  $\mu$  (cs) 27.8  $\mu$  (ct) 27.9  $\mu$  (cu) 28.0  $\mu$  (cv) 28.1  $\mu$  (cw) 28.2  $\mu$  (cx) 28.3  $\mu$  (cy) 28.4  $\mu$  (cz) 28.5  $\mu$  (ca) 28.6  $\mu$  (cb) 28.7  $\mu$  (cc) 28.8  $\mu$  (cd) 28.9  $\mu$  (ce) 29.0  $\mu$  (cf) 29.1  $\mu$  (cg) 29.2  $\mu$  (ch) 29.3  $\mu$  (ci) 29.4  $\mu$  (cj) 29.5  $\mu$  (ck) 29.6  $\mu$  (cl) 29.7  $\mu$  (cm) 29.8  $\mu$  (cn) 29.9  $\mu$  (co) 30.0  $\mu$  (cp) 30.1  $\mu$  (cq) 30.2  $\mu$  (cr) 30.3  $\mu$  (cs) 30.4  $\mu$  (ct) 30.5  $\mu$  (cu) 30.6  $\mu$  (cv) 30.7  $\mu$  (cw) 30.8  $\mu$  (cx) 30.9  $\mu$  (cy) 31.0  $\mu$  (cz) 31.1  $\mu$  (ca) 31.2  $\mu$  (cb) 31.3  $\mu$  (cc) 31.4  $\mu$  (cd) 31.5  $\mu$  (ce) 31.6  $\mu$  (cf) 31.7  $\mu$  (cg) 31.8  $\mu$  (ch) 31.9  $\mu$  (ci) 32.0  $\mu$  (cj) 32.1  $\mu$  (ck) 32.2  $\mu$  (cl) 32.3  $\mu$  (cm) 32.4  $\mu$  (cn) 32.5  $\mu$  (co) 32.6  $\mu$  (cp) 32.7  $\mu$  (cq) 32.8  $\mu$  (cr) 32.9  $\mu$  (cs) 33.0  $\mu$  (ct) 33.1  $\mu$  (cu) 33.2  $\mu$  (cv) 33.3  $\mu$  (cw) 33.4  $\mu$  (cx) 33.5  $\mu$  (cy) 33.6  $\mu$  (cz) 33.7  $\mu$  (ca) 33.8  $\mu$  (cb) 33.9  $\mu$  (cc) 34.0  $\mu$  (cd) 34.1  $\mu$  (ce) 34.2  $\mu$  (cf) 34.3  $\mu$  (cg) 34.4  $\mu$  (ch) 34.5  $\mu$  (ci) 34.6  $\mu$  (cj) 34.7  $\mu$  (ck) 34.8  $\mu$  (cl) 34.9  $\mu$  (cm) 35.0  $\mu$  (cn) 35.1  $\mu$  (co) 35.2  $\mu$  (cp) 35.3  $\mu$  (cq) 35.4  $\mu$  (cr) 35.5  $\mu$  (cs) 35.6  $\mu$  (ct) 35.7  $\mu$  (cu) 35.8  $\mu$  (cv) 35.9  $\mu$  (cw) 36.0  $\mu$  (cx) 36.1  $\mu$  (cy) 36.2  $\mu$  (cz) 36.3  $\mu$  (ca) 36.4  $\mu$  (cb) 36.5  $\mu$  (cc) 36.6  $\mu$  (cd) 36.7  $\mu$  (ce) 36.8  $\mu$  (cf) 36.9  $\mu$  (cg) 37.0  $\mu$  (ch) 37.1  $\mu$  (ci) 37.2  $\mu$  (cj) 37.3  $\mu$  (ck) 37.4  $\mu$  (cl) 37.5  $\mu$  (cm) 37.6  $\mu$  (cn) 37.7  $\mu$  (co) 37.8  $\mu$  (cp) 37.9  $\mu$  (cq) 38.0  $\mu$  (cr) 38.1  $\mu$  (cs) 38.2  $\mu$  (ct) 38.3  $\mu$  (cu) 38.4  $\mu$  (cv) 38.5  $\mu$  (cw) 38.6  $\mu$  (cx) 38.7  $\mu$  (cy) 38.8  $\mu$  (cz) 38.9  $\mu$  (ca) 39.0  $\mu$  (cb) 39.1  $\mu$  (cc) 39.2  $\mu$  (cd) 39.3  $\mu$  (ce) 39.4  $\mu$  (cf) 39.5  $\mu$  (cg) 39.6  $\mu$  (ch) 39.7  $\mu$  (ci) 39.8  $\mu$  (cj) 39.9  $\mu$  (ck) 40.0  $\mu$  (cl) 40.1  $\mu$  (cm) 40.2  $\mu$  (cn) 40.3  $\mu$  (co) 40.4  $\mu$  (cp) 40.5  $\mu$  (cq) 40.6  $\mu$  (cr) 40.7  $\mu$  (cs) 40.8  $\mu$  (ct) 40.9  $\mu$  (cu) 41.0  $\mu$  (cv) 41.1  $\mu$  (cw) 41.2  $\mu$  (cx) 41.3  $\mu$  (cy) 41.4  $\mu$  (cz) 41.5  $\mu$  (ca) 41.6  $\mu$  (cb) 41.7  $\mu$  (cc) 41.8  $\mu$  (cd) 41.9  $\mu$  (ce) 42.0  $\mu$  (cf) 42.1  $\mu$  (cg) 42.2  $\mu$  (ch) 42.3  $\mu$  (ci) 42.4  $\mu$  (cj) 42.5  $\mu$  (ck) 42.6  $\mu$  (cl) 42.7  $\mu$  (cm) 42.8  $\mu$  (cn) 42.9  $\mu$  (co) 43.0  $\mu$  (cp) 43.1  $\mu$  (cq) 43.2  $\mu$  (cr) 43.3  $\mu$  (cs) 43.4  $\mu$  (ct) 43.5  $\mu$  (cu) 43.6  $\mu$  (cv) 43.7  $\mu$  (cw) 43.8  $\mu$  (cx) 43.9  $\mu$  (cy) 44.0  $\mu$  (cz) 44.1  $\mu$  (ca) 44.2  $\mu$  (cb) 44.3  $\mu$  (cc) 44.4  $\mu$  (cd) 44.5  $\mu$  (ce) 44.6  $\mu$  (cf) 44.7  $\mu$  (cg) 44.8  $\mu$  (ch) 44.9  $\mu$  (ci) 45.0  $\mu$  (cj) 45.1  $\mu$  (ck) 45.2  $\mu$  (cl) 45.3  $\mu$  (cm) 45.4  $\mu$  (cn) 45.5  $\mu$  (co) 45.6  $\mu$  (cp) 45.7  $\mu$  (cq) 45.8  $\mu$  (cr) 45.9  $\mu$  (cs) 46.0  $\mu$  (ct) 46.1  $\mu$  (cu) 46.2  $\mu$  (cv) 46.3  $\mu$  (cw) 46.4  $\mu$  (cx) 46.5  $\mu$  (cy) 46.6  $\mu$  (cz) 46.7  $\mu$  (ca) 46.8  $\mu$  (cb) 46.9  $\mu$  (cc) 47.0  $\mu$  (cd) 47.1  $\mu$  (ce) 47.2  $\mu$  (cf) 47.3  $\mu$  (cg) 47.4  $\mu$  (ch) 47.5  $\mu$  (ci) 47.6  $\mu$  (cj) 47.7  $\mu$  (ck) 47.8  $\mu$  (cl) 47.9  $\mu$  (cm) 48.0  $\mu$  (cn) 48.1  $\mu$  (co) 48.2  $\mu$  (cp) 48.3  $\mu$  (cq) 48.4  $\mu$  (cr) 48.5  $\mu$  (cs) 48.6  $\mu$  (ct) 48.7  $\mu$  (cu) 48.8  $\mu$  (cv) 48.9  $\mu$  (cw) 49.0  $\mu$  (cx) 49.1  $\mu$  (cy) 49.2  $\mu$  (cz) 49.3  $\mu$  (ca) 49.4  $\mu$  (cb) 49.5  $\mu$  (cc) 49.6  $\mu$  (cd) 49.7  $\mu$  (ce) 49.8  $\mu$  (cf) 49.9  $\mu$  (cg) 50.0  $\mu$  (ch) 50.1  $\mu$  (ci) 50.2  $\mu$  (cj) 50.3  $\mu$  (ck) 50.4  $\mu$  (cl) 50.5  $\mu$  (cm) 50.6  $\mu$  (cn) 50.7  $\mu$  (co) 50.8  $\mu$  (cp) 50.9  $\mu$  (cq) 51.0  $\mu$  (cr) 51.1  $\mu$  (cs) 51.2  $\mu$  (ct) 51.3  $\mu$  (cu) 51.4  $\mu$  (cv) 51.5  $\mu$  (cw) 51.6  $\mu$  (cx) 51.7  $\mu$  (cy) 51.8  $\mu$  (cz) 51.9  $\mu$  (ca) 52.0  $\mu$  (cb) 52.1  $\mu$  (cc) 52.2  $\mu$  (cd) 52.3  $\mu$  (ce) 52.4  $\mu$  (cf) 52.5  $\mu$  (cg) 52.6  $\mu$  (ch) 52.7  $\mu$  (ci) 52.8  $\mu$  (cj) 52.9  $\mu$  (ck) 53.0  $\mu$  (cl) 53.1  $\mu$  (cm) 53.2  $\mu$  (cn) 53.3  $\mu$  (co) 53.4  $\mu$  (cp) 53.5  $\mu$  (cq) 53.6  $\mu$  (cr) 53.7  $\mu$  (cs) 53.8  $\mu$  (ct) 53.9  $\mu$  (cu) 54.0  $\mu$  (cv) 54.1  $\mu$  (cw) 54.2  $\mu$  (cx) 54.3  $\mu$  (cy) 54.4  $\mu$  (cz) 54.5  $\mu$  (ca) 54.6  $\mu$  (cb) 54.7  $\mu$  (cc) 54.8  $\mu$  (cd) 54.9  $\mu$  (ce) 55.0  $\mu$  (cf) 55.1  $\mu$  (cg) 55.2  $\mu$  (ch) 55.3  $\mu$  (ci) 55.4  $\mu$  (cj) 55.5  $\mu$  (ck) 55.6  $\mu$  (cl) 55.7  $\mu$  (cm) 55.8  $\mu$  (cn) 55.9  $\mu$  (co) 56.0  $\mu$  (cp) 56.1  $\mu$  (cq) 56.2  $\mu$  (cr) 56.3  $\mu$  (cs) 56.4  $\mu$  (ct) 56.5  $\mu$  (cu) 56.6  $\mu$  (cv) 56.7  $\mu$  (cw) 56.8  $\mu$  (cx) 56.9  $\mu$  (cy) 57.0  $\mu$  (cz) 57.1  $\mu$  (ca) 57.2  $\mu$  (cb) 57.3  $\mu$  (cc) 57.4  $\mu$  (cd) 57.5  $\mu$  (ce) 57.6  $\mu$  (cf) 57.7  $\mu$  (cg) 57.8  $\mu$  (ch) 57.9  $\mu$  (ci) 58.0  $\mu$  (cj) 58.1  $\mu$  (ck) 58.2  $\mu$  (cl) 58.3  $\mu$  (cm) 58.4  $\mu$  (cn) 58.5  $\mu$  (co) 58.6  $\mu$  (cp) 58.7  $\mu$  (cq) 58.8  $\mu$  (cr) 58.9  $\mu$  (cs) 59.0  $\mu$  (ct) 59.1  $\mu$  (cu) 59.2  $\mu$  (cv) 59.3  $\mu$  (cw) 59.4  $\mu$  (cx) 59.5  $\mu$  (cy) 59.6  $\mu$  (cz) 59.7  $\mu$  (ca) 59.8  $\mu$  (cb) 59.9  $\mu$  (cc) 60.0  $\mu$  (cd) 60.1  $\mu$  (ce) 60.2  $\mu$  (cf) 60.3  $\mu$  (cg) 60.4  $\mu$  (ch) 60.5  $\mu$  (ci) 60.6  $\mu$  (cj) 60.7  $\mu$  (ck) 60.8  $\mu$  (cl) 60.9  $\mu$  (cm) 61.0  $\mu$  (cn) 61.1  $\mu$  (co) 61.2  $\mu$  (cp) 61.3  $\mu$  (cq) 61.4  $\mu$  (cr) 61.5  $\mu$  (cs) 61.6  $\mu$  (ct) 61.7  $\mu$  (cu) 61.8  $\mu$  (cv) 61.9  $\mu$  (cw) 62.0  $\mu$  (cx) 62.1  $\mu$  (cy) 62.2  $\mu$  (cz) 62.3  $\mu$  (ca) 62.4  $\mu$  (cb) 62.5  $\mu$  (cc) 62.6  $\mu$  (cd) 62.7  $\mu$  (ce) 62.8  $\mu$  (cf) 62.9  $\mu$  (cg) 63.0  $\mu$  (ch) 63.1  $\mu$  (ci) 63.2  $\mu$  (cj) 63.3  $\mu$  (ck) 63.4  $\mu$  (cl) 63.5  $\mu$  (cm) 63.6  $\mu$  (cn) 63.7  $\mu$  (co) 63.8  $\mu$  (cp) 63.9  $\mu$  (cq) 64.0  $\mu$  (cr) 64.1  $\mu$  (cs) 64.2  $\mu$  (ct) 64.3  $\mu$  (cu) 64.4  $\mu$  (cv) 64.5  $\mu$  (cw) 64.6  $\mu$  (cx) 64.7  $\mu$  (cy) 64.8  $\mu$  (cz) 64.9  $\mu$  (ca) 65.0  $\mu$  (cb) 65.1  $\mu$  (cc) 65.2  $\mu$  (cd) 65.3  $\mu$  (ce) 65.4  $\mu$  (cf) 65.5  $\mu$  (cg) 65.6  $\mu$  (ch) 65.7  $\mu$  (ci) 65.8  $\mu$  (cj) 65.9  $\mu$  (ck) 66.0  $\mu$  (cl) 66.1  $\mu$  (cm) 66.2  $\mu$  (cn) 66.3  $\mu$  (co) 66.4  $\mu$  (cp) 66.5  $\mu$  (cq) 66.6  $\mu$  (cr) 66.7  $\mu$  (cs) 66.8  $\mu$  (ct) 66.9  $\mu$  (cu) 67.0  $\mu$  (cv) 67.1  $\mu$  (cw) 67.2  $\mu$  (cx) 67.3  $\mu$  (cy) 67.4  $\mu$  (cz) 67.5  $\mu$  (ca) 67.6  $\mu$  (cb) 67.7  $\mu$  (cc) 67.8  $\mu$  (cd) 67.9  $\mu$  (ce) 68.0  $\mu$  (cf) 68.1  $\mu$  (cg) 68.2  $\mu$  (ch) 68.3  $\mu$  (ci) 68.4  $\mu$  (cj) 68.5  $\mu$  (ck) 68.6  $\mu$  (cl) 68.7  $\mu$  (cm) 68.8  $\mu$  (cn) 68.9  $\mu$  (co) 69.0  $\mu$  (cp) 69.1  $\mu$  (cq) 69.2  $\mu$  (cr) 69.3  $\mu$  (cs) 69.4  $\mu$  (ct) 69.5  $\mu$  (cu) 69.6  $\mu$  (cv) 69.7  $\mu$  (cw) 69.8  $\mu$  (cx) 69.9  $\mu$  (cy) 70.0  $\mu$  (cz) 70.1  $\mu$  (ca) 70.2  $\mu$  (cb) 70.3  $\mu$  (cc) 70.4  $\mu$  (cd) 70.5  $\mu$  (ce) 70.6  $\mu$  (cf) 70.7  $\mu$  (cg) 70.8  $\mu$  (ch) 70.9  $\mu$  (ci) 71.0  $\mu$  (cj) 71.1  $\mu$  (ck) 71.2  $\mu$  (cl) 71.3  $\mu$  (cm) 71.4  $\mu$  (cn) 71.5  $\mu$  (co) 71.6  $\mu$  (cp) 71.7  $\mu$  (cq) 71.8  $\mu$  (cr) 71.9  $\mu$  (cs) 72.0  $\mu$  (ct) 72.1  $\mu$  (cu) 72.2  $\mu$  (cv) 72.3  $\mu$  (cw) 72.4  $\mu$  (cx) 72.5  $\mu$  (cy) 72.6  $\mu$  (cz) 72.7  $\mu$  (ca) 72.8  $\mu$  (cb) 72.9  $\mu$  (cc) 73.0  $\mu$  (cd) 73.1  $\mu$  (ce) 73.2  $\mu$  (cf) 73.3  $\mu$  (cg) 73.4  $\mu$  (ch) 73.5  $\mu$  (ci) 73.6  $\mu$  (cj) 73.7  $\mu$  (ck) 73.8  $\mu$  (cl) 73.9  $\mu$  (cm) 74.0  $\mu$  (cn) 74.1  $\mu$  (co) 74.2  $\mu$  (cp) 74.3  $\mu$  (cq) 74.4  $\mu$  (cr) 74.5  $\mu$  (cs) 74.6  $\mu$  (ct) 74.7  $\mu$  (cu) 74.8  $\mu$  (cv) 74.9  $\mu$  (cw) 75.0  $\mu$  (cx) 75.1  $\mu$  (cy) 75.2  $\mu$  (cz) 75.3  $\mu$  (ca) 75.4  $\mu$  (cb) 75.5  $\mu$  (cc) 75.6  $\mu$  (cd) 75.7  $\mu$  (ce) 75.8  $\mu$  (cf) 75.9  $\mu$  (cg) 76.0  $\mu$  (ch) 76.1  $\mu$  (ci) 76.2  $\mu$  (cj) 76.3  $\mu$  (ck) 76.4  $\mu$  (cl) 76.5  $\mu$  (cm) 76.6  $\mu$  (cn) 76.7  $\mu$  (co) 76.8  $\mu$  (cp) 76.9  $\mu$  (cq) 77.0  $\mu$  (cr) 77.1  $\mu$  (cs) 77.2  $\mu$  (ct) 77.3  $\mu$  (cu) 77.4  $\mu$  (cv) 77.5  $\mu$  (cw) 77.6  $\mu$  (cx) 77.7  $\mu$  (cy) 77.8  $\mu$  (cz) 77.9  $\mu$  (ca) 78.0  $\mu$  (cb) 78.1  $\mu$  (cc) 78.2  $\mu$  (cd) 78.3  $\mu$  (ce) 78.4  $\mu$  (cf) 78.5  $\mu$  (cg) 78.6  $\mu$  (ch) 78.7  $\mu</$

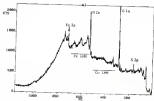
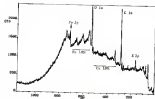
surface or below the copper sulfide layer at the surface. The underlying boron layer is etched in contact with the electrolyte in all cases. The iron oxide thickness decreases at 20°C range from 100 to 150 nm for  $V_{\text{app}}$  = 100V to 200V. The chloride layer thickness ranges from 100 to 2 nm.

### Temperature-Dependent Oxidation in Air/Sulfuric

#### Low Temperature and Potentials

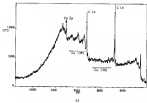
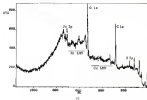
Electrochemical Analysis X-ray photoelectron spectroscopy (XPS) was used to analyze four Fe-SiO<sub>2</sub> specimens heated at 200°C (Fe-100h), 200h (Fe-200h), 400h (Fe-400h), and 800h (Fe-800h). An XPS survey spectra of each specimen is shown in Figure 4-20. The Fe 2p lines along with the iron binding energy peaks for Fe and Fe are detected in each specimen. Additionally the sulfide lines were observed for each specimen with the exception of specimen Fe-800h (200°C). The Si 2p line observed in the survey scans of Figure 4-20a, Figure 4-20b, and Figure 4-20c is most likely from polishing sile as described in Chapter 3.

In addition to survey scans, specific XPS peaks were analyzed at higher energy resolution. High resolution Fe 2p spectra were recorded from the specimens heated for 0.5 hours, 1 hour, and 2 hours (see Figure 4-21a). The Fe 2p peak at 686 eV indicates that a sulfide is present, while that at approximately 689 eV is associated with a sulfate, as elemental sulfur was detected. The sulfate line was most intense from specimens Fe-100h (0.5h) and Fe-200h (1h) and in fact was higher in intensity than the sulfide peak. The ratio of sulfate to sulfide peaks (integrated from the three specimens heated for shorter times) was decreased. The sulfide peak could originate from the bulk of an interfacial sulfide layer. The sulfate layer formed could then be quantitatively thicker (at 10 hours).



(a)

Figure 4 (a) XPS survey spectra for specimens heated at 500°C, (a) B2 (1000s), (b) B3 (1000s), (c) B4 (1000s), and (d) B5 (1000s).



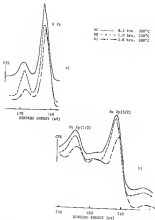


Figure 4-31. High-resolution XPS spectra for chloroacetic anhydrides (heated at 100°C): (a) Fe 2p; (b) Fe 2p(1/2); (c) Fe 2p(3/2).





4c

0.5 hr. —————  
 1.0 hr. - - - - -  
 2.0 hr. — · — · —



4d

resulting in a less intense oxide peak. The Fe 2p spectra from the short time heated specimens are shown in Figure 4 (ii). A small shift (1 eV) to a lower binding energy and a satellite line detected at approximately 718 eV are observed for 300°C (as compared to the other specimens). The 300°C specimen for the more than 2 hours, shown in Figure 4 (iii), illustrates that two peaks at binding energies of 711 eV and 708 eV identified as a hematite and goethite respectively gave an intensity on the heating time at 300°C is increased from 1.4 hours to 2 hours. Conversely, the peak at 705 eV, identified as a metal oxide, decreases with time at temperature. Thus, the surface evolution is correlated to a hematite and goethite composed as a function of time at 300°C. The Cu 2p peak (see Figure 4 (iv)) was detected only for specimen E1 in the Fe 2p peak region the Fe 2p peak. The presence of Cu could be due to nonuniformity in the film or a copper oxide layer at or near the surface.

X-ray Induced Auger Spectroscopy. The X-ray induced Fe LMM Auger lines shown in Figure 4 (v) for computerized heated specimens were quite broad (7-10eV), due in part to the very overlapping Auger lines. Auger lines frequently exhibit chemical shifts which are larger than core level photoelectron lines due to larger relaxation energies [7080 eV]. As changes with heating time were observed in the Auger line shapes which suggests that the film products detected at the surface as a result of heating were stable. However, the X-ray induced Fe LMM transitions are each more evident on heated versus unheated specimens.

The most intense line observed for Cu was the  $L_{2,3}VV$  line. Although the Cu  $L_{2,3}VV$  (930eV) line was observed in all three specimens, as was the Fe  $L_{2,3}VV$  (890eV) line, there was a decrease in the Cu line intensity as

best treated film was increased. However, there was no change in the peak energy towards either  $\text{Cu}(\text{OH})_2$ ,  $\text{Cu}_2\text{O}$ , or Cu.

#### High-resolution XPS. Three specimens were best treated at 400°C

for 1 hour and analyzed with xps. Depth profiles were obtained to determine the film geometry and relative thickness of each layer.

Atomic concentrations of the eleven main species (see Table 1) were obtained (Cu was with inclusion); Fe (Cu film without inclusion); and Fe (oxide with inclusions of  $\text{Cu}_2\text{O}$ ) and depth profiles as shown in Figure 4 (8). In all cases an iron oxide was observed at the surface (Fe 2p split in the low energy Fe 2VV peaks). Copper and sulfur were detected

on the unpolished surface for specimens 8E and 9E. Within the first couple of minutes (2 to 3 minutes) of sputtering, S decreased while the S and Cu ions seem to increase in specimens 8E and 9E. Longer sputtering (8 minutes) was required to see the same trend for specimen 9E. The Fe-S interaction is most obvious in specimens 8E and 8F where the outer iron oxide layer is distinct from the inner layer and much thicker for specimen 8E. This is not as clearly seen for specimen 9E since an iron oxide-copper-sulfur was all detected simultaneously at the surface. The bulk composition is depleted in Fe with an

approximate composition of  $\text{CuFe}_{0.4}\text{S}_{0.2}\text{O}_{1.2}$ . The inner layer of specimen 8E has a Cu/Fe ratio that was greater than unity but became equal to unity at the bulk while that of specimen 9E (Figure 4.10c) is 4/3. The intermediate layer for specimens 8E (4 to 77 minutes) and 9E (4 to 8 minutes) seem to be associated with a copper-rich sulfate. Data from XPS suggested that both a copper sulfate and an iron oxide were present at the surface. Thus, although the film is too thin to determine its actual geometry, there is good indication that a copper sulfate had in-

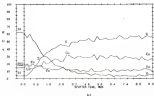
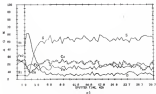
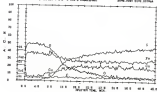


Figure 4-32 wt depth profile for polished specimen heated at 500°C for 2 hours: (a) Fe for base with lamellae; (b) Fe for base without lamellae; and (c) Ni base with  $\text{Co}_2\text{S}_3$  (see 14-1004).

FILE 007 IN DATA BUNDLE 000 0000

SCALE FACTOR, DIFFERENTIAL 1 AND 2 ANALYSIS

200-0000 0000 0000

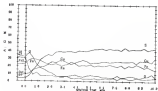


iron oxide may be simultaneously present on the surface of specimens 10 and 11.

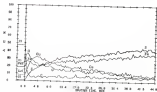
The low energy Fe XPS peaks detected at the sputtered and polished surfaces (between 2 and 4eV) are consistent with an  $\text{Fe}_2\text{O}_3/\text{Fe}$  layer and a small amount of FeOOH (since a hydroxide was detected with XPS as indicated by the peak energy difference (see section discussion of Chalcopyrite in laboratory air)). Within the lower oxide layer in specimen 10, the Cu/Fe ratio is greater than unity and is consistent with a Cu-Fe compound while the Fe is more likely bonded to the oxygen since no iron oxide was not detected from XPS data. Again following that the surface layer is a mixed  $\text{Cu}_2\text{S}/\text{FeS}_2/\text{Fe}$  region.

Fractured chalcopyrite specimens were analyzed with AED to determine if the film layer structure was equivalent to that of polished then heated specimens. The 10 Kev specimens were freshly fractured then heated at 400°C for 1 hour. Specimen 10F contained no inclusions while specimen 10F contained inclusions of FeOOH and Cu<sub>2</sub>S. The depth profiles for the CuFeS<sub>2</sub> region of each specimen are shown in Figure 4.10. Specimen 10F (without inclusions) has a thin outer iron oxide layer (see Figure 4.10a) that gives is a bulk CuFeS<sub>2</sub> at greater depths. A Cu/Fe ratio greater than unity is detected after 2-7 minutes of sputtering which indicates that a copper sulfide under a copper-rich iron sulfide composed may be present between the surface oxide and the bulk.

Specimen 10F (with inclusions) has an outer iron oxide layer while at 5 minutes of sputtering the Cu/Fe ratio is 1.7 which suggests that the lower layer is a Cu-rich sulfide. Moreover, the Cu/Fe ratio does not level off at unity as would be expected for a bulk CuFeS<sub>2</sub>. The bulk is



a)



b)

Figure 4 (a) XRD depth profiles for specimen 100°C for 2 hours; (a) 100°C (without inclusions) and (b) 100°C (with inclusions)

displayed in 1a and 5. Since these specimens were immediately fractured before testing it was not possible to know which areas had previously existed as cracks and were fractured before fracturing. In spite of this, the outer layer on all samples was an iron oxide (just as was found on polished specimens of chalcopyrite). An intermediate copper-rich sulfide layer is demonstrated. The region beyond the intermediate layer which should have been the bulk chalcopyrite may in fact have been removed due to previous reactions. The indentation free specimen did show a depth profile that was equivalent with specimens 1B and 1C suggesting that the condition of a fresh fractured surface is equivalent to a polished specimen at 400°C.

Optical photomicrographs. Chalcopyrite specimens from the 1a Run that were heat treated at 400°C for times ranging from 30 minutes to 12 hours. An optical micrograph representation of the four specimens is shown in Figure 4 1a (specimen 1C). Chalcopyrite regions were measured with 1000 hour specimens 1B(100°C, 2 hrs), 1B(200°C, 2hrs), 1B(300°C, 2hrs), and 1B(400°C, 12hrs). All polished 1a Run specimens contained deep area PGM inclusions (less than  $5 \mu^2$  (2- 1 to 2) inclusions). The optical photomicrograph taken at a magnification of 400X shown in Figure 4 1a suggests that inclusions were a major constituent of the specimen but this is not accurate and only appears to be true because of the magnification used for the photomicrograph. A more accurate representation of the structural area of inclusions can be seen in Figure 4 1c.

Exponential optical micrographs/analysis. Reflection curves from chalcopyrite are shown in Figure 4 1B as a function of heat treatment time at 400°C. The value of  $R_{\text{max}}$  and  $L_{\text{max}}$  for specimen 1C is 42% and 475nm, after 30 minutes at 400°C. These values are similar



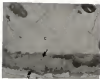


Figure 4-66 Optical Photomicrograph representative of a bulk chalcoprite (B) specimen (B) (a) (b) with arsenite (P) and pyrite (P) inclusions. The black areas observed are pores.

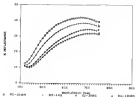


Figure 4.98 Soljection curves for bulk anisotropic crystallization (anneal) at 300°C for (a) (curve a): 1 (curve b): 2 (curve c): and 10 (curve d) hours.

to those from a freshly polished specimen<sub>0</sub> with only a slight decrease in  $\lambda_{\text{min}}$  and a corresponding increase in  $\lambda_{\text{max}}$ . In addition, a decreased reflectance at 480nm (12%) was observed as compared to freshly polished values of 18%. This same trend was observed for the other three curves in Figure 4.18 with a shift to  $\lambda_{\text{max}}$  to higher wavelengths and an overall decrease in reflected intensity. A reflectance minimum,  $\lambda_{\text{min}}$ , develops at 1 hour and shifts to larger wavelengths with a later  $t_{\text{min}}$  with increased heating time at 300°C (see Table 4.8). The reflectance parameters shown below in Table 4.8 also include those for shifts in  $\lambda_{\text{min}}$  up to 160nm. The values for 0.5, 1, and 2 hours of heating at 300°C are representative of Baile and Le Bars specimens. Both specimens contained  $\text{Cu}_2\text{S}$  inclusions in much greater quantity as compared with Le Bars specimens which contained inclusions of CuS and FeS<sub>2</sub>. The greatest shift in  $\lambda_{\text{min}}$  was found in Le Bars specimens at 300°C for  $\lambda_{\text{min}}$  regions within 100nm of the  $\text{Cu}_2\text{S}$  value. This same trend was seen in all Baile specimens heated at 300°C and is most likely due to reaction between the chalcopyrite and the copper sulfide vein (see Appendix C).

The shift of  $\lambda_{\text{min}}$  to larger wavelengths for reactions at 300°C is consistent with shifts observed in  $\lambda_{\text{min}}$  up to 120nm for reactions at 200°C. This shift is consistent with an increase in the thickness of the outer oxide layer as demonstrated with xrf depth profile data from specimens 18 and 28 as compared to specimens 16 and 20. In addition the intermediate layer was more complicated suggesting that the shift in  $\lambda_{\text{min}}$  and the shape of the reflectance curve are dependent on both the thickness of the film and the composition present. Greater shifts at 300°C were found from chalcopyrite areas within 100nm of copper sulfide

Table 4.3  
Wavelength and reflectance maxima and minima for  $\text{CuFeS}_2$  specimens heated at 300°C for various times

Specimen	Time	$\lambda_{\text{max}}$	$\lambda_{\text{min}}$	$\lambda_{\text{min}}$	$\lambda_{\text{min}}$
8C	None	670	48.0		
8D	1 hour	670	48.0		
		690	50.0	490	11.0
		690	50.0	425	11.0
8J	2 hours	690	50.0	490	9.0
		710	50.0	430	10.0
8E	3 hours	690	50.0	490	11.0
7E	3 hours	690	48.0	430	10.0
8H	3 hours	740	51.0	490	9.0
		740	51.0	430	12.0
8A	12 hours	700	50.0	490	10.0
		790	51.0	490	10.0
		700	50.0	430	9.0

incisions. Reflectance curves from areas > 100 $\mu$ m away from the copper sulfide incisions had  $\lambda_{\text{min}} = 4$  micron. Thus the increase in  $\lambda_{\text{min}}$  is due to increased reactivity which is dependent upon the copper sulfide incisions.

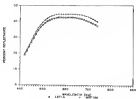
The  $\text{Cu}_2\text{S}$  incisions in bulk and in bare specimens have been observed to transform to covellite at 300°C and 400°C (see Appendix C).

Thus an increase in the reactivity of chalcopyrite in contact with  $\text{Cu}_2\text{S}$  was observed both as a shift in the  $\lambda_{\text{min}}$  value as well as an increase in the thickness of the mirror iron scale as observed from AAS depth profile data. The reaction of chalcopyrite at 30°C and 300°C are equivalent in the reaction products formed however the extent of reaction is affected by the increase in temperature and the subsequent liberation of the copper sulfide incisions.

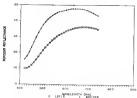
To compare fractured specimens heated at 300°C with polished specimens EPS was used to analyze the surface products. The reflectance curves for Le Barre specimens 8EP (with incisions) and 8EP(without incisions) freshly fractured then heated at 300°C for 2 hours are shown

in Figure 4.16. The reflectance curves for freshly fractured areas are equivalent to those observed for freshly polished specimens. After heating, the same areas were analyzed with ABE. In the case of specimen BBE the same area was analyzed with ABE, however this was not possible with specimen DAF. Auger data suggested that a thin outer iron oxide layer was associated with a copper sulfide and an intermediate copper rich sulfide layer. These data support that for these fresh fractured areas of chalcopyrite the reaction at 200°C is equivalent to that of a freshly polished specimen and is an extension from the reaction at 110°C.

Calculated optical spectroreflectance spectra. Calculated reflectance curves for two specimens heat treatments were modeled with a hematite layer in contact with the bulk chalcopyrite, an outer  $\text{Fe}_2\text{S}_3$  layer and a copper sulfide layer between  $\text{Fe}_2\text{S}_3$  and  $\text{Cu}_2\text{FeS}_3$ . Calculated and experimental reflectance curves are shown to agree in Figure 4.17 for polished specimens heated at 200°C. Experimental reflectance curves for fractured specimens were equivalent to those shown in Figure 4.17. Reflectance curves with connected symbols represent experimental data while the curve with disconnected symbols represent calculated data. These were best fit with CdS or  $\text{Cu}_2\text{S}$  on the copper sulfide layer and the iron sulfide layer being  $\text{Fe}_2\text{S}_3$ , consistent with ABE data. The reflectance curves for specimens BB(Dar) and BB(Dar) are represented in Figure 4.18 as connected lines and connected plus signs, respectively. They are compared with a calculated curve for an  $\text{Fe}_2\text{S}_3$  outer layer which is designated with disconnected triangles (in triangles). For the thin layer represented with later-shown to follow the calculated curves were similar with  $\text{Fe}_2\text{S}_3$  or  $\text{FeS}$ , this was also consistent with ABE data for unpolished areas, while this was not true

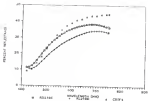


a)



b)

Figure 3. GIX reflectance curves for Cu Beep specimens (a) with fractured and (b) after heating at 600°C for 2 hours.



$\text{SiO}_2/\text{Si}_3\text{N}_4$
$\text{SiO}_2/\text{Si}$
$\text{SiO}_2/\text{Si}_3\text{N}_4/\text{Si}$
$\text{SiO}_2/\text{Si}_3\text{N}_4$ Substrate

Thickness Range  $d$  (nm)

4-6

6-12

8-4

Figure 4.25

Calculated (dashed) and experimental (solid) curves for the three specimens listed at 25°C for the case of specimens 80 (dashed), 81 (solid) and 82 (dotted) of 10 nm and 20 nm thickness of the film layer structure for calculated reflectance curves.

for larger shifts in  $\lambda_{\text{min}}$ , where the iron oxide was consistent with an  $\text{Fe}_2\text{O}_3$  layer. For the fractured specimen 007 the difference between the calculated and measured reflectance curves with  $\lambda_{\text{min}} = 495\text{-}505\text{nm}$  led to an outer iron oxide layer 4nm thick and equivalent to those in Figure 4.10.

A similar comparison was done for two areas on specimen 00 for  $\lambda_{\text{min}}$  values of 540nm and 545nm as shown in Figure 4.10. The upper oxide for these curves was modelled with  $\text{Fe}_2\text{O}_3$  (1 nm) for  $\lambda_{\text{min}}$  values and the outer iron oxide was  $\text{Fe}_2\text{O}_3$  (10nm). The calculated curve for  $\text{Fe}_2\text{O}_3/\text{Fe}_2\text{O}_3$  is represented as unconnected diamonds. For  $\lambda_{\text{min}}$  values the thickness for the iron oxide ( $\text{Fe}_2\text{O}_3$ ) was then while the top was too thick (see Figure 4.10b-unconnected  $\Delta^n$ ). As the  $\lambda_{\text{min}}$  shifts to longer wavelengths the overall thickness of the film increases. Since the upper oxide layer is much thinner than either the hercynite or the outer iron oxide layer both components fit the data equally well. However, by not using a copper sulfide layer the calculated reflectance curves are much less consistent with the reflectance data (discussed in Chapter 5). In addition by using either  $\text{Fe}_2\text{O}_3$  or  $\text{FeSO}_4$  in the outer layer the comparison between calculated and experimental curves was not good. This will also be discussed in Chapter 5.

These data suggest that the film layer structure consistent with A01, A02, and 008 data results is an outer iron oxide and copper sulfide layer with an intermediate hercynite layer in contact with the chalcopyrite substrate. The shift in  $\lambda_{\text{min}}$  ranges from 495nm to 545nm with an outer iron oxide thickness that ranges from 2nm to 10nm while the copper sulfide layer ranges from 2nm to 10nm. The hercynite layer thickness ranges from 2nm to 10nm for the corresponding shift in  $\lambda_{\text{min}}$ .



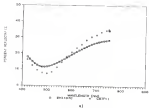
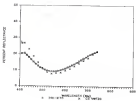


Figure 4 24

Calculated (curve b) and reflectance curves versus wavelength curves (curve a) for the two specimens tested at 200°C for (specimen a) 1 min + 10 min and b) 1 min + 10 min. Schematic of the film layer structure are shown below the reflectance curves.



b)

Thickness  $d$  (nm)

20.0

10.0

20.0

### Surface Temperature and Treatment

Exposure studies (XPS) species from the hydroxide specimens with 100%NiO<sub>2</sub>. Both specimens of chlorophyll from the West and North were heat treated at 300°C for times ranging between 1 and 4 hours in laboratory air. Specimen 10 was heated for 1 hour, while 22, 24 and 25 (West) were heated for 2 hours and 26 was heated for 4 hours. The 10 to 4 to, Fe(2p<sub>3/2</sub>), and Cu(2p<sub>3/2</sub>) lines from four specimens are compared in Figure 4.20. The information from each peak will be discussed in turn, beginning with the 10 to peak.

All of the 10 to peaks were shifted to an energy near 100 eV indicative of a sulfate (see Figure 4.19). No absorbed sulfate was detected at the left but very weak sulfate peaks between 181 eV and 185 eV were observed for specimens 22 and 24. These weak peaks could have been due to a  $K_{\alpha}$  X-ray satellite line about 7 eV below the main line but the absence this line for specimen 26 proves that the sulfate peak reported above was weak but real. As indicated previously, no sulfate sufficiently thick to totally obscure aluminum from the substrate is present; therefore the sulfate must be deposited in the iron oxide. The O 1s lines shown in Figure 4.18b dissociated into three distinct contributions as shown for specimen 26 in Figure 4.19. The components are centered at 533 eV-535 eV, 531 eV-533 eV and 529 eV-531 eV which are consistent with a sulfate (TSPAC) a hydroxide (PHAL) and sulfate compound (SMTU).

The Fe 2p lines shown in Figure 4.19c are similar for 1 or 2 hours but become very asymmetric after 4 hours at 300°C. The weak satellite line at a binding energy approximately 7 eV higher than the Fe(2p<sub>3/2</sub>) line is consistent with the Fe being oxidized as either an

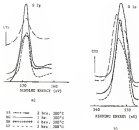
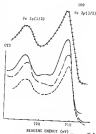


Figure 4.28

High energy resolution XPS spectra for polypropylene oxidized with ceric oxide heated at 200°C for 2 or 4 hours; a) O(1s); b) C(1s). a) Fe (1p<sub>3/2</sub>) and Al (2p<sub>3/2</sub>)



	Time	Temp
1A	2 hrs.	300°C
1B	1 hr.	300°C
1C	4 hrs.	300°C
1D	2 hrs.	300°C
1E	2 hrs.	300°C



sulfide, hydrosulfide, or sulfide. Large asymmetry is also after 4 hours at 500°C) generally result from large charge transfer during the formation of higher oxidation states of the transition metal (TMC1, S2S1A, S2S1B, T2S1C). Copper was detected at the surface using the Cu(2p<sub>3/2</sub>/2p<sub>1/2</sub>) line shown in Figure 4.200. The Cu lines have similar peak angles (90° left) while specimens 88 and 89 are shifted higher (approximately 100°). However all of the Cu(2p<sub>3/2</sub>) peaks are so broad, it is obvious that multiple chemical states are represented. In fact two components, one near 90° representing sulfide and another near 100° representing Cu<sub>2</sub>S (sulfate), could be deconvoluted from the spectra (see Table 4.6).

This is contrast to samples heated to 500°C, heating samples with incubation at 500°C creates sulfides on the surface. It appears that both Cu and Fe form sulfides under these conditions. Besides the sulfides, oxides and hydrosulfides of iron are present, similar to before from degradation and 500°C reaction.

Table 4.6

X-ray photoelectron peak deconvolution for five specimens heated at 500°C for 1 (S2S1), 100 (S2S1A, S2S1B) and 4 hours (T2S1C). Numbers in parentheses are relative peak intensities

Specimen	Fe(2s)	Fe(2p)	Fe(2p <sub>3/2</sub> /2p <sub>1/2</sub> )	Cu(2p <sub>3/2</sub> /2p <sub>1/2</sub> )
85	100.0 (100)	530 (100)	708.0 (100)	100.0 (100)
		500.0 (100)	711.0 (100)	100.0 (100)
		560.0 (100)	714.0 (100)	
87	100.0 (100)	330.0 (100)	710.0 (100)	100.0 (100)
		560.0 (100)	710.0 (100)	100.0 (100)
		571.0 (100)	709.0 (100)	
88	100.0 (100)	530 (100)	710.0 (100)	100.0 (100)
		500.0 (100)	710.0 (100)	100.0 (100)
		560.0 (100)	710.0 (100)	
89	100.0 (100)	500.0 (100)	710.0 (100)	100.0 (100)
		560.0 (100)	710.0 (100)	100.0 (100)
		571.0 (100)	710.0 (100)	
90	100.0 (100)	530.0 (100)	710.0 (100)	100.0 (100)
		500.0 (100)	710.0 (100)	100.0 (100)
		560.0 (100)	710.0 (100)	

Depth profiling performed with RPS yielded chemical information about the film products after reaction in laboratory air at 300°C. Specimen SP(300°C, 3hrs) was sputtered with argon ions incrementally while collecting high energy resolution data for Fe, Cu, O, S, and C. High energy resolution RPS scans were performed for each element before sputtering and incrementally between sputtering. A summary of the peaks assigned using computer assisted deconvolution procedures and the corresponding sputter times are shown in Table 4.7. An S 2p peak was observed between 30 seconds and 3 minutes of sputtering. After 3 minutes of sputtering, a S 2p peak coincident with a sulfate was detected at 163 eV. Similarly, after 30 seconds of sputtering the S 2s peaks from sulfate and sulfonate were reduced to zero and only the peak due to an oxide remained. The Fe(2p<sub>3/2</sub>/4p) line shifted toward higher binding energy by a sulfate ligand was also observed by sputtering. The Cu(2p<sub>3/2</sub>/4p) line was initially weak and remained so until after 3 minutes of sputtering, at which time it increased in intensity concomitant with the increased S 2p intensity.

To further verify the presence of sulfate at the surface, angle resolved RPS was used. Spectra were collected at 30° and 60° take off angles for an unsputtered specimen (SR). By using the relative peak intensities of the deconvoluted S 2s peaks for sulfonate and sulfate versus sulfur at 3-40° angles of 2.0 and 1.2 were obtained, respectively. At 3-40° the corresponding ratios are 0.3 and 1.1 demonstrating that the sulfonate and sulfate components are concentrated at the outer surface.

These data suggest that the sulfate and sulfonate ligands are restricted to the outer surface (in the order of 5 nm). The sulfate products are consistent with both a copper sulfate and an iron sulfate





while the hydrosulfide appears to be confined only with the iron. The bulk of the reaction product layer is an oxide and Auger data have indicated that the oxide is dominated by  $\text{Fe}_2\text{O}_3$ . This is consistent with the XPS data. The Cu and S peaks detected below the oxide layer are consistent with a copper sulfide.

XPS Measurements Specimen for Incision Free Specimens. Four incision free specimens were analyzed with XPS for the S 2p, O 1s, Fe 2p as shown in Figure 4 (b). The Cu2p3/2 peak was weakly detected. A sulfide peak was detected for each specimen in addition to the presence of a sulfate peak which could be due to either the bulk or to underlying sulfate compound within the surface film as shown in Figure 4 (b). The O 1s peaks suggested the presence of an oxide [689.7-690.0eV], a hydrosulfide [688.4eV-688.7eV], and a sulfate [689.4eV-689.7eV] in all specimens (see Figure 4 (b)). The Fe 2p line shown in Figure 4 (b) was similar for all four specimens. Contributions from peaks at 709.4eV and 710.4eV from iron oxide and iron hydrosulfide, respectively, were found through peak deconvolution. A low intensity third peak at 714.4eV was also observed after deconvolution and is considered with a number of iron sulfate species. The Cu 2p line was more difficult to interpret due to low signal to noise ratios for specimens 20 and 22. An Cu 2p line was detected for specimen 20(200°C 1hr).

Specimen 20(200°C,1hr) was sputtered within the XPS system to obtain information on the chemical state of the film formed as a result of the heat treatment. Sputtering was done alternatively with high energy resolution analysis of Fe 2p, S 2s, O 1s, and Cu 2p lines after each sputtering sequence. A summary of the information obtained from specimen 20 as a function of sputtering time is shown in Table 4.3.

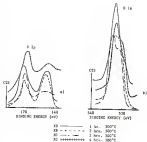


Figure 4.28 XPS high energy resolution spectra for inclusion from cholesteryl 11-β-D-xylofuran. Recorded at 300°C: (a) 2p, (b) 2s, and (c) Fe 2s(11/12).

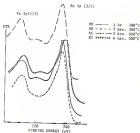


Table 4.4

Peak deconvolution data for specimen 2B (300 °C anneal) sputtered for 2 minutes. Numbers in parentheses are relative peak height information.

Sputtering Time	Fe 2p	C 1s	S 2s	Si 2p
Unannealed	715.8 (100) 721.8 (10) 718.8 (10)	285.8 (100) 288.8 (45) 281.4 (10)	188.2 (40) 188.0 (10)	See text
30 sec	708.8 (100) 721.8 (10) 724.8 (20)	288.8 (100) 288.8 (45) 281.8 (10)	181.8 (90) 188.0 (20)	830.8
1 min	708.8 (100) 721.8 (100) 724.8 (20)	288.1 (70) 288.8 (200) 288.8 (45)	181.5 (80) 200.1 (10)	830.11
2 min	708.8 (100) 718.8 (10) 715.8 (20)	288.1 (50) 288.4 (10)	181.5 (100)	830.8
3 min	708.8 (100) 718.8 (10)	288.1 (10) 281.4 (10)	181.5 (100)	830.8

The Fe 2p line is shown in Figure 4.11 as a function of sputter time as compared to the Fe 2p line of specimen 2B in Figure 4.10 after heat treatment and before sputtering. An immediate decrease in the sulfate peak after 30 seconds of sputtering was observed. A sulfate peak was not detected after 2 minutes sputtering. Thus, the sulfate compound was present on the outer 200 to 400 Å of the film, meaning that the sputtering rate is close to that for an iron oxide (10-15Å/minute) before sputtering. The C 1s lines at 285 eV (consistent with C sulfate) and the hydrocarbon (282 eV) are the dominant peaks but between 20 seconds and 2 minutes of sputtering the dominant peak shifts to 281.4 eV which is consistent with a metal oxide. Deconvolution of the Fe 2p line showed that the dominant peak was at 721 eV before heating and before sputtering (see Table 4.4). After 20 seconds of sputtering this peak

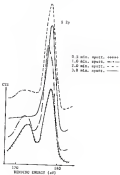


Figure 4.16. GPC high energy resolution spectra for 9.1p as a function of scattering size for species 33 (250°C, 1000g).

shifted to 711 keV while after 1 minute of sputtering the peaks at 706 keV and 701 keV are fairly equally intense. After 2 and 3 minutes of sputtering a single dominant peak is observed at 710 keV. Two peaks were observed at approximately 706 & 710 keV and 711 & 712 keV throughout the first three minutes of sputtering. In the deficiency of the hydroxide detection, the Fe 2p peak grew from a satellite (710 keV) and a hydroxide (701 keV) to an iron oxide (706.8 eV). The Fe 2p line was not detected initially, suggesting either that the surface film was thick enough to mask the detection of copper from the substrate and an overlying oxide and that the surface film formed has no copper in the outer 10-20Å of the film. However, after 40 seconds of sputtering a small Cu 2p peak was detected (see Table 4.4) at 899.8keV which shifted to 881 keV after 5 minutes of sputtering.

The data show that a sulfate exists at the surface of inclusion-free chalcogenites but sputtering for three minutes will remove the sulfate. This was demonstrated by the positive reduction of the S 2p and S 2s peaks at 1600eV and 1618 keV, respectively. Simultaneously the FeO<sub>2</sub>(Fe<sup>3+</sup>/Fe<sup>2+</sup>) peak at 710-714eV associated with sulfate is also reduced. The FeO<sub>2</sub>(Fe<sup>3+</sup>/Fe<sup>2+</sup>) peak was very weak for the heated and unspattered surface. In contrast to the surface of chalcogenites with inclusions. This indicates that without inclusion, copper sulfate is not formed on chalcogenites by heating to 500°C. However, the surface concentration of iron sulfate is observed as it was on samples with inclusions. Also similar to samples with inclusions, both the Fe and S signals increased after sputtering for 3 minutes, indicating that copper sulfate was present in the iron oxide.

Angle resolved XPS data were again collected at  $80^\circ$  and  $90^\circ$  take-off angles. Consistent with samples with inclusions, the ratio of the O 1s peak associated with oxides to that with oxides was 0.8 for  $80^\circ$  and 1.0 for  $90^\circ$  (sample BC heated to  $500^\circ\text{C}$  for 8 hours). The higher ratio at the more surface sensitive angle ( $80^\circ$ ) demonstrates that the oxide is concentrated at the surface, consistent with sputter profile data.

Fractured specimens heated at  $500^\circ\text{C}$  were analyzed with XPS and compared to data obtained from polished specimens to determine if oxidation surface products were formed. The fractured specimens were fractured immediately before heating and analyzed with XPS after heat treatment. Specimen LF contained no inclusions while BP contained inclusions of graphite and oxides; a survey scan of each specimen was found to be similar to those of polished specimens heated at  $500^\circ\text{C}$  for 8 hours. The Fe Auger transitions were weaker for fractured specimen LF while the C 1s peak was stronger. However, for specimen BP (with inclusions), the C 1s peak was weaker and the Fe Auger transitions were strong and equivalent to those of specimens first polished then heated (8 hours). The Cu Auger lines were also weak with specimens similar to polished and heated specimens. Both specimens showed the presence of a surface composed of the surface, which is most likely an iron oxide since Cu Lp was not detected in these specimens (contrary to the polished then heated specimens with inclusions). In iron oxides it is detected at the surface of fractured and heated specimens as was observed for polished and heated specimens. The iron oxide and hydroxide detected were equivalent to that observed on polished then heated specimens with and without inclusions.

Fe<sub>2</sub>O<sub>3</sub> and Fe<sub>3</sub>O<sub>4</sub> species. Auger peak analysis in specific areas of specimen 88-10870 (see) (see Figure 4.10) was employed to obtain a depth profile of the film formed after heat treatment. The value associated with this specimen was average peak as compared to the beam-pulse of the freshly polished specimen. Auger spectra of the characterization region showed that the primary chemical compositions detected on the surface were Fe and O with some C and Si. Additionally, two low energy Fe LMM transitions were detected before sputtering. The low energy Fe LMM transition (40-50 eV) indicated the presence of an iron oxide because the Fe LMM transition was split into two peaks at 40-50 eV and 51-52 eV (peak energy difference equals 2 eV). The split in peaks and the energy difference between the two peaks is consistent with an Fe<sub>2</sub>O<sub>3</sub> layer with a small amount of Fe<sub>3</sub>O<sub>4</sub> or FeOx at the surface. From RPE data the FeOx layer is believed to be present with the Fe<sub>2</sub>O<sub>3</sub>. Sputtering resulted in a decrease in the peak energy difference to 2 eV which is consistent with Fe<sub>3</sub>O<sub>4</sub> [1088] and surface removal of FeOx. After depth profiling, only one Fe LMM transition was detected. The splitting of the Fe LMM Auger transition upon oxidation has been interpreted in terms of a cross transition between the 3 d<sub>xy</sub> states and the Fe 3p states in Fe<sub>2</sub>O<sub>3</sub> [1087]. That is, the coexistence of two low peaks in the Auger spectrum is associated with rearrangement of the electronic structure of the surface upon the Fe oxide formation.

The depth profile for the characterization region is shown in Figure 4.10. An outer oxide layer was observed. A copper-rich sulfide layer between the oxide and the bulk characterization is indicated (approximately 6 minutes of sputtering) since the Cu/Fe peak to peak ratio is greater than unity. The copper-rich region and the inner oxide region cover the



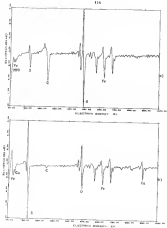
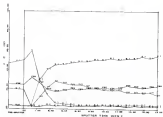


Figure 4 (b) XPS initial analysis for the electrolyte region in specimen 66 (1000°C-10h): a) survey scan before sputtering; b) survey scan after sputtering; and c) depth profile (170eV).



c)

analysis map from a region in between but this could not be clearly detected by AED or SEM.

A spinel depth profile (see Figure 4 10) was obtained for a chalcopyrite region colored blue within specimen 18 which contained copper sulfide inclusions ( $\text{Cu}_{1.4}\text{S}$ ) and was heated at 400°C for three days compared to the depth profile of specimen 16 (inclusions, heated 400°C then, Figure 4 10). The most striking difference is the thicker iron oxide layer on the blue chalcopyrite area. The copper sulfide regions were also analyzed with Auger (see appendix C). The major difference between the inclusions before and after heating is indicated by the bulk composition. The initial bulk atomic concentrations of inclusions were either  $\text{Fe}$  or  $\text{Cu}_{1.4}\text{S}$ . However, the final bulk concentrations were  $\text{FeCu}_{0.7}\text{S}_{0.8}$  for both specimens which is close to that for bornite ( $\text{Cu}_5\text{FeS}_4$ ). The chalcopyrite region in specimen 16 (Figure 4 10) was found to have a thicker iron oxide outer layer. A region below the outer iron oxide layer is copper-rich. Thus, the blue region is associated with a thicker iron oxide and a region below the oxide that is a copper rich sulfide.

An even more dramatic color change was observed for specimen 14 (100°C, three) which contained copper sulfide ( $\text{Cu}_{1.4}\text{S}$ ) inclusions. The color was characterized with electron microprobe data from an untreated specimen. One area of the specimen was colored blue while another area was colored purple. Two regions within each colored area were assigned. The chalcopyrite region (Figure 4 14) for both the purple and the blue have an outer layer of iron oxide; however, the layer is approximately twice as thick for the blue region as for the purple region. The region between the bulk chalcopyrite and the outer iron oxide in the purple

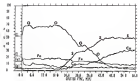
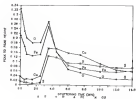
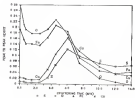


Figure 4.30 Add speaker depth profile for the time challenge region within spectrum 80 located at 800°S for 100



a)



b)

Figure 4-24 AES depth profile for a chalcogenide resist in argon gas heated at 355°C for 2 hrs : a) purple area and b) blue area

area could not be clearly determined. The smaller increases and decreases in the iron and copper peaks at the oxide/sulfide interface may be due to changing positions in each area. The differences in oxide thickness could be due to a difference in the bulk composition of chalcopyrite or the amount of inclusion present. The blue area had a greater concentration of copper sulfide which may have led to the greater deviation from the chalcopyrite stoichiometry (due to the reaction of chalcopyrite with the inclusions and the subsequent formation of hercynite inclusions).

To demonstrate that the reaction products formed on specimens with inclusions (blue areas) were representative of that formed on inclusion-free specimens a depth profile of specimen 22 heated at 800°C for 8 hours is shown in Figure 4.10. A thick outer iron oxide layer is shown that goes to a copper-rich sulfide layer between 24 and 36 microns of sputtering. These data demonstrate that the reaction products formed at 800°C are similar to those formed at 200°C. No outer iron oxide layer is detected with an intermediate copper-rich sulfide layer for both specimens with and without inclusions.

Experimental section: secondary electron spectra. The 800°C heat treated samples analyzed by XPS and AES were also analyzed with SEM. Section 1a from specimen 22 was heated at 800°C for 8 hours. A representative secondary micrograph (200X magnification) is shown in Figure 4.11 for this specimen. The actual photomicrograph is of specimen 22(800°C, 8hrs). The reflectance curves for CuFeS<sub>2</sub> samples analyzed within specimens 22(200°C, 1hr), 22(800°C, 8hrs), 22(800°C, 8hrs) 22(200°C, 8hrs) and 22(800°C, 8hrs) are summarized in Table 4.9.

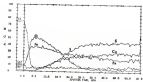


Figure 4.28 AED depth profile for Ga InGaAs/InGaAs YB (yellow) epilayers. Sample is 100°C for 24hrs.

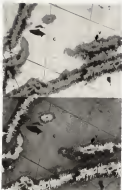


Figure 4. (a) Optical photomicrograph (500X) representative of a bulk silicophrase (N) specimen with corundum (N) and graphite (P) inclusions. (b) Freshly polished specimen (N) and (b) specimen (N) after heating at 800 °C for 4 hours.



Reflectance parameters for the wavelength and percent reflectance of the maximum and minimum reflectance peaks are detailed to correspond with the corresponding reflectance curve for each specimen. The points chosen for initial analysis showed that the two-pulse action of the sample changed little from the freshly polished brass pulley  $\text{CuPd}_{10}$ . The reflectance curves of these areas in specimens BE, DE, and EF were equivalent to those reported at 25°C and 300°C.

Table 4.3

Wavelength and reflectance maxima and minima for chalcopyrite areas within specimens heated to 300°C

Specimen	Region	$\lambda_{\text{min}}$	$R_{\text{min}}$	$\lambda_{\text{max}}$	$R_{\text{max}}$
BE	La face	480	25.0	700	88.0
DE	La face	480	25.0	700	88.0
EF	La face	480	0.0		
BE	La face	480	0.0		

By analyzing other regions of the specimens, more dramatic color changes were observed with the SEM (see Table 4.3C). The reflectance curve of specimen BE in Figure 4.1B shows one maximum and one minimum peak. The reflectance curve for a chalcopyrite area colored blue in specimen EF (La face) is similar to that for a blue colored area within specimen BE (bottom) shown in Figure 4.17c. The blue colored areas on chalcopyrite specimens from different areas were equivalent.

A broad peak in the low wavelength region (440nm) was observed in regions BE with a shift in  $\lambda_{\text{min}}$  to 490nm; this is the largest shift in  $\lambda_{\text{min}}$  observed in the reflectance curves for chalcopyrite (see Figure 4.1B and Table 4.3C). These reflectance curves were characteristic of chalcopyrite areas adjacent to or within 100µm of a single or double inclusion. Thus, the presence of copper sulfide inclusions

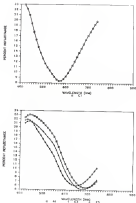


Figure 4.27 Reflectance curves for chalcogenizing zones in specimen 28 heated at 500°C: a) zone away from inclusions and b) zone adjacent to inclusions

[For specimens heated at 400°C or 500°C] results in an increased reactivity of the chalcopyrite upon exposure to the inclusion.

Table 4.18

Wavelength and reflectance maxima and minima for other chalcopyrite areas on specimens heated at 500°C.

Specimen	Color	$\lambda_{max}$	$R_{max}$	$\lambda_{min}$	$R_{min}$
4P	blue	475	4.0		
4B	blue	475	3.2		
	purple	480	5.4	480	33.0
	purple	480	3.4	480	39.4
	purple	480	4.0	480	31.6
4R	blue	480	3.3	480	35.5
	purple	480	5.1		
5A	blue	480	3.0	480	35.4
	purple	480	5.5	480	36.3
4R	purple	480	3.4	480	34.0

Specimen 4A(500°C, 480s) showed two distinct colored areas across a specimen (1 mm x 1 mm) - a blue colored area and purple colored area. Their wavelengths and reflectance maxima and minima are shown in Table 4.18. The purple area from specimen 4R and the blue area from specimen 4B (see Figure 4.18 and Table 4.18) are similar to the purple and blue colored areas of chalcopyrite in specimen 5A. Specimen 5A contained only  $\text{Cu}_2\text{S}$  inclusions (see also specimen 4B) while specimen 4B contained iron-sulfur inclusions and a small amount of CuS (see Figure 4.24 and Figure 4.25). Thus the reaction of specimen 4R or either 4B or 4A (containing either  $\text{Cu}_2\text{S}$  or CuS inclusions) resulted in reflectance curves that were equivalent. The transformation of  $\text{Cu}_2\text{S}$  or CuS to hematite ( $\text{Fe}_2\text{O}_3$ ) leads to similar reaction of the chalcopyrite within limits of the inclusions.

In four specimens with no inclusions were first heated at 400°C for the same times as for those with inclusions to determine if the reaction of the  $\text{CuFeS}_2$  was independent of the phases present in the bulk.

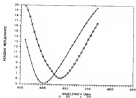


Figure 8-34 Reflectance curves for two chalcogenide glass (a) samples 8B (Controlled CuI and FeSO<sub>4</sub>) (b) sample 8C (FeSO<sub>4</sub>) for 4 hours

specimens. Specimens 33a, 33b, 34, and 35 were analyzed; their reflectance parameters,  $L_{\text{min}}$  and  $L_{\text{max}}$  (for instance in their reflectance curves are shown in Table 4.11) and are similar to those obtained from 30°C and 300°C OMI data.

Table 4.11  
Reflectance parameters,  $L$  and  $R$ , for inclusion-free chalcopyrite specimens heated at 300°C for various times

Specimen	Time	$L_{\text{min}}$	$L_{\text{min}}$	$L_{\text{max}}$	$R_{\text{max}}$
33a	1hr			276	20.8
33b	2hrs			288	20.8
34	1hrs	488	4.8		
35	2hrs	488	4.8	738	20.8
35	4hrs	488	20.8	748	20.8

The reflectance curves for specimens 33a-33b, 35, and 36 are shown in Figures 4.39 and not to be compared with the curves used in the imagery of Table 4.9. A drop in intensity ( $L_{\text{min}}$ - $R_{\text{max}}$ ) was observed at 300°C and the peak at 300°C as compared to a freshly polished chalcopyrite specimen as shown in Figure 4.4. Heating specimens for 2 and 4 hours at 300°C showed reflectance curves with more detailed reflectance parameter changes with respect to the reflectance parameters of a freshly polished chalcopyrite. The same trend in the shift of  $L_{\text{min}}$  to longer wavelengths was observed for inclusion-free specimens at 300°C and 300°C. Other areas within the bulk specimens were analyzed. The reflectance curves for  $L_{\text{min}}$  between 300°C and 300°C are shown in Figure 4.40. These curves are similar to those with equivalent  $L_{\text{min}}$  values (for example see Figure 4.19 for detection at 30°C. Heat treatments at 300°C resulted in reflectance curves that were similar to those at 30°C and 300°C for shifts in  $L_{\text{min}}$  up to 100nm. Greater shifts in  $L_{\text{min}}$  were observed at 300°C resulting in no  $L_{\text{min}}$  between 300°C and 300°C. A broad peak was also detected between 300°C and 300°C for  $L_{\text{min}}$  between 300°C and 300°C.

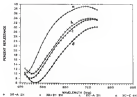


Figure 4 (b) Measurable curves from an incident-free (a) bare specimen heated at 300°C; (b) (from curve a), (c) (from curve a), (d) (from curve a), and (e) (from curve b)

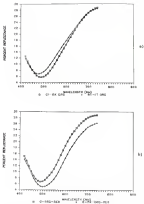
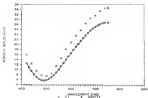


Figure 4-40. Diffraction curves for two groups of specimens BA and AC ( $1000^{\circ}\text{C}$  (Step 1) of specimen BA, isothermal and b) specimen AC, isothermal).

Calculated and experimental X-ray diffraction patterns. (Experimental)

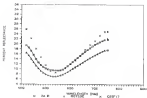
Reflection curves for specimens heated at 100°C were compared to calculated reflection curves. The layer structures used was specimens 15 which was used for reflection curves obtained from reactions at 10°C and 100°C. The outer iron oxide was  $\text{Fe}_2\text{O}_3$  while the thin outer sulfide next to the iron oxide was either  $\text{CuS}$  or  $\text{Co}_3\text{S}$  and the copper-rich sulfide in contact with the chalcopellite was always modeled as  $\text{Cu}_3\text{FeS}_4$ . As the  $L_{\text{SIS}}$  shifted to higher wavelengths and  $L_{\text{SIS}}$  decreased the outer iron oxide thickness increased. Similarly it was found that the FeS film covered when all of the layers had thicknesses that were obtained by balanced chemical equations as discussed in Chapter 5. The comparison between calculated and experimental reflection curves for  $L_{\text{SIS}}$ -films is equivalent to that shown in Figure 4.37. For  $L_{\text{SIS}}$ -films the calculated (designated as unannealed x's) and experimental curves (designated as annealed brass) are shown in Figure 4.42. The reflectance and calculated curve for  $L_{\text{SIS}}$ -films are consistent with the data obtained from heat treatments at 10°C and 100°C. The outer iron oxide was 1100 Å thick. For  $L_{\text{SIS}}$ -films the outer iron oxide was found to be 1100 Å thick as demonstrated in the calculated curve designated with unannealed x's in Figure 4.43. Likewise as  $L_{\text{SIS}}$  shifted to shift to longer wavelengths the thickness of the outer iron oxide was also increased and in fact increased linearly. The data for the large shift in  $L_{\text{SIS}}$  in films is shown in Figure 4.45 and the data for  $L_{\text{SIS}}$ -films and  $L_{\text{SIS}}$ -films are shown in Figure 4.46 and Figure 4.45 respectively. The iron oxide ( $\text{Fe}_2\text{O}_3$ ) thickness increases from 1100 Å to 1700 Å and 1700 Å as the reaction product layers thicken. In addition, the amorphous





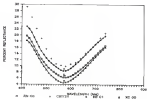
	Thickness $d$ (nm)
$\text{SiO}_2/\text{Si}$	11.8
$\text{Co}_2\text{S}_3$	1.87
$\text{Co}_2\text{S}_3/\text{FeS}_2$	24.76
$\text{CoFeS}_2$	
Substrate	

Figure 4 (a) Calculated (curve b) versus experimental (curve a) reflectance curves for specimen 24 with GaInAsGa for back transparency at 600 °C. Schematic of film layer before reflectance curves.



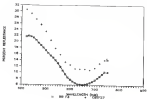
	Dickeur $\delta$ (nm)
$\text{Fe}_2\text{O}_3$	17,5
$\text{Cu}_2\text{S}$	3,5
$\text{Fe}_2\text{O}_3/\text{Fe}_2\text{S}_3$	10,5
$\text{CuFeS}_2$	
Substrato	

Figure 4.43 Calculated (curve a) versus experimental reflectance versus the wavelength (b) curve b) and (c) curve c) for thin-films the best corresponds to (a) (b) (c) (d) (e) of film layer with reflectance curve



	Thickness (Å)
$\text{Fe}_2\text{O}_3$	20.0
$\text{Ca}_2\text{F}_2$	10.0
$\text{Ca}_2\text{Fe}_2\text{O}_7$	20.0
$\text{CaFe}_2\text{O}_7$ Substrate	

Figure 4-49 Calculated versus experimental reflectance curves for species 42 (curve a), 43 (curve b), and 44 (curve c) with 1000-0000 Å incident irradiance at 100% (bottom) of film layer below reflectance curves.

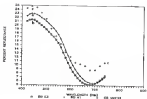
Thickness  $t$  (nm)

27.4

4.0

26.2

Figure 4 (a) Calculated (curve a) versus experimental (curve b) diffraction curves for specimen 10 (see) treated at 100°C in air. (b) Schematic of film layer below reflectance curves.



	Thickness $d$ (nm)
$\text{Fe}_2\text{O}_3$	55.6
Co	6.35
$\text{Co}_2\text{Fe}_2\text{O}_4$	47.5
$\text{CoFe}_2\text{O}_4$	
Substrate	

Figure 4-48 Calculated (curve c) versus experimental (curves a and b) reflectance curves for multilayer thin film created at  $300^\circ\text{C}$ . Substrate: deposition of thin layer below reflectance curve.

that is observed at 4000-4400 cm was explained by the calculated curves as shown in Figure 4-20.

#### Summary of X-Ray Structure of Reaction Products On Chalcopyrite

The X-ray structure consistent with the XRD, IR, and EDX data results is a  $\text{Cu}_2\text{FeS}_4$  layer in contact with the  $\text{CuFeS}_2$  substrate and an outer  $\text{Fe}_2\text{S}_3$  layer with either CuS or  $\text{Cu}_2\text{S}$  in between the outer iron oxide and the ferrite. This reaction can be affected by the type and quantity of inclusion in the substrate and their geometry. A summary of the reaction products formed on chalcopyrite between 300°C and 400°C is shown in Table 4-13. Although the sulfate products formed two phases in Table 4-13 they were a single constituent at the surface.

Table 4-13

A summary of the reaction products formed on natural specimens of chalcopyrite heated between 300°C and 400°C in air.

300°C	350°C, 400°C															
	WITH $\text{Cu}_2\text{S}$	WITHOUT $\text{Cu}_2\text{S}$														
<table> <tr><td><math>\text{Fe}_2\text{O}_3</math> / <math>\text{Fe}_2\text{S}_3</math></td></tr> <tr><td><math>\text{Cu}_2\text{S}</math> / CuS</td></tr> <tr><td><math>\text{Cu}_2\text{FeS}_4</math></td></tr> <tr><td>CuFeS<sub>2</sub></td></tr> </table>	$\text{Fe}_2\text{O}_3$ / $\text{Fe}_2\text{S}_3$	$\text{Cu}_2\text{S}$ / CuS	$\text{Cu}_2\text{FeS}_4$	CuFeS <sub>2</sub>	<table> <tr><td>CuS / <math>\text{Fe}_2\text{S}_3</math></td></tr> <tr><td><math>\text{Fe}_2\text{S}_3</math></td></tr> <tr><td><math>\text{Cu}_2\text{S}</math> / CuS</td></tr> <tr><td><math>\text{Cu}_2\text{FeS}_4</math></td></tr> <tr><td>CuFeS<sub>2</sub></td></tr> </table>	CuS / $\text{Fe}_2\text{S}_3$	$\text{Fe}_2\text{S}_3$	$\text{Cu}_2\text{S}$ / CuS	$\text{Cu}_2\text{FeS}_4$	CuFeS <sub>2</sub>	<table> <tr><td><math>\text{Fe}_2\text{S}_3</math> / <math>\text{Fe}_2\text{O}_3</math></td></tr> <tr><td><math>\text{Fe}_2\text{S}_3</math></td></tr> <tr><td><math>\text{Cu}_2\text{S}</math> / CuS</td></tr> <tr><td><math>\text{Cu}_2\text{FeS}_4</math></td></tr> <tr><td>CuFeS<sub>2</sub></td></tr> </table>	$\text{Fe}_2\text{S}_3$ / $\text{Fe}_2\text{O}_3$	$\text{Fe}_2\text{S}_3$	$\text{Cu}_2\text{S}$ / CuS	$\text{Cu}_2\text{FeS}_4$	CuFeS <sub>2</sub>
$\text{Fe}_2\text{O}_3$ / $\text{Fe}_2\text{S}_3$																
$\text{Cu}_2\text{S}$ / CuS																
$\text{Cu}_2\text{FeS}_4$																
CuFeS <sub>2</sub>																
CuS / $\text{Fe}_2\text{S}_3$																
$\text{Fe}_2\text{S}_3$																
$\text{Cu}_2\text{S}$ / CuS																
$\text{Cu}_2\text{FeS}_4$																
CuFeS <sub>2</sub>																
$\text{Fe}_2\text{S}_3$ / $\text{Fe}_2\text{O}_3$																
$\text{Fe}_2\text{S}_3$																
$\text{Cu}_2\text{S}$ / CuS																
$\text{Cu}_2\text{FeS}_4$																
CuFeS <sub>2</sub>																

## CHAPTER 3 DISCUSSION

### Introduction

The system investigated in this study consisted of various specimens of chalcopyrite from either the Lehigh or Butte mines. In general the specimens contained inclusions of copper sulfides along or in conjunction with goethite. It was of interest to determine those reactions that were intrinsic to bulk chalcopyrite. Both polished specimens and specimens fractured in air were reacted in laboratory air at 150°C, 200°C, and 300°C to determine the effects of the polishing procedure upon surface reactions.

### Calculation of Reflections from Reacted Chalcopyrite

Based on the surface products reported from the literature in both aqueous and nonaqueous environments a number of film geometries were postulated as an initial attempt to calculate reflectance curves. As a first attempt, the intermediate region was chosen to be  $\text{Fe}_2\text{FeS}_4$  [Barnitt] while the outer oxide layer was varied between  $\text{Fe}_2\text{O}_3$  [Magnetite],  $\text{Fe}_3\text{O}_4$  [Magnetite], and hematite [goethite]. Chemical equations were written for chalcopyrite reacting with oxygen and in some cases water to form hematite and either magnetite, hematite, or goethite as the outer oxide. Surface diffusion was assumed as a gas. Heating data [Brown 1978] have shown that  $\text{Fe}_2\text{O}_3$  is given off at temperatures of 300°C and above. Reflectivity data from chalcopyrite [Brown] has shown that sulfur is released from the bulk substrate from below room temperatures.

up to 300°C, thus depicting the bulk composition in surface. Further heating in air to form  $\text{Ba}_2\text{O}_3$  which can be obtained as a reaction product both at 300°C, 350°C, and 400°C.

The chemical equations are first balanced according to the number of atoms on each side of the equation. Following this the density ( $\rho$  gm/cm<sup>3</sup>) and molecular weight ( $M$ ) of each compound are used to calculate a thickness ( $\delta$ ) of the compound formed covering a unit area of reaction. In addition, the amount of chlorophyllin that is consumed can also be calculated and checked to be sure that this is consistent with the equation. It was found that the amount of chlorophyllin consumed was a small fraction of a percent of the thickness of the complex (mg) films formed from a one thin specimen corresponds to a thickness change of only 0.00010. An example of the calculation for chlorophyllin reacting to form barite plus peroxide is shown in Table 8.1. This procedure was used for each balanced chemical equation to obtain the calculated thickness of the surface layer formed and the equivalent thickness of each individual product layer.

The film thickness for peroxide ( $\delta_p$ ) was varied from one to three for the outer layer which in the above example was peroxide. The thickness of the intermediate barite layer ( $\delta_b$ ) and the amount of thickness of chlorophyllin ( $\delta_c$ ) consumed is automatically set by the value of  $\delta_p$  according to the ratios shown in Table 8.1. The reflectance versus wavelength was then calculated based upon this two layer model. This calculation was repeated for each of the three inner oxides with an intermediate barite layer. The results of these calculations are summarized in Table 8.2. A schematic diagram of the film geometry is shown for each chemical equation. Those chemical equations which



Table 1.1

Estimation of the thickness of layers formed in chalcopyrite according to the chemical equation written below. The density is defined as  $\rho = \text{mass}/\text{volume} = \text{mass}/(\text{area} \times \text{thickness})$  (1)  $\text{thickness} = \text{mass}/(\text{area} \times \rho)$ . The mass(s) is the weight of silver times the molecular weight( $MW$ ).

	Calcd $Q_1 = 1 \pm Q_1 = 1.6 \times 10^{-4} \text{ cm}^3$	$Q_1 = 1.6 \times 10^{-4} \text{ cm}^3$	$Q_1 = 1 \pm Q_1$
$T$	4.8	5.97	5.5
Wt. Ag	183.5	201.5	20.45
$Q$	$Q_1$	$Q_1$	$Q_1$
<hr/>			
$\frac{\text{Calcd}(Q_1)}{\text{Wt}(Q_1)} = \frac{4.8}{1.6 \times 10^{-4}}$	$= \frac{183.5 / Q_1}{(1.6 \times 10^{-4}) / Q_1}$	$= \frac{20.45 \times Q_1}{Q_1}$	
$1.50 \times 10^4$	$\rightarrow Q_1 = .450 \times 10^{-4}$		
<hr/>			
$\frac{\text{Wt}(Q_1)}{\text{Calcd}(Q_1)} = \frac{5.97}{1.6 \times 10^{-4}}$	$= \frac{(1.6 \times 10^{-4}) / Q_1}{(1.6 \times 10^{-4}) / Q_1}$	$= \frac{2 \times 20.45 \times Q_1}{Q_1}$	
3.73	$\rightarrow Q_1 = .445 \times 10^{-4}$		
<hr/>			

chalcopyrite to react further and an iron oxide was judged inadequate for describing the reaction based on the shape of the overall reflectance curve and the values of the percent reflectance as a function of wavelength when compared to experimental curves. This inadequacy will be graphically demonstrated below.

Rejection of the validity of a bilayer structure is consistent with AAS and XPS data which indicated that the film layer structure was more complicated than a copper rich inner layer and an outer iron oxide. Specifically, copper oxides appeared to be present within the iron oxide layer and need be accounted for in the model.



In addition to copper sulfide ATR and RRS data clearly show the presence of organic and hydrocarbon contamination and oxidation on the surface. The surface containing contaminants and oxidation are non-absorbing solids which will not change the shape of the reflectance curves. Rather, non-absorbing solids will simply cause an overall decrease in the reflected intensity. Thus, the lack of agreement between experimental and calculated reflectance curve shapes when ferrous and oxide layers were assumed to be present cannot result from ignoring surface contamination or the surface reaction products. Indeed, the assumed structure of absorbing reaction products must be modified further.

Several other arrangements of reaction products were investigated in attempt to improve the agreement between experimental and calculated reflectance data. In a second geometry, reflectance was calculated assuming the iron oxide films are on top of an intermediate ferrous compound. Film thickness ratios were calculated using the balanced chemical equation approach described above. This geometry led to calculated reflectance curves with shapes that were an improvement upon the previous set of chemical equations. The best was achieved with a  $\text{CuFe}_2\text{S}_4$  /  $\text{Cu}_2\text{FeS}_4$  /  $\text{Fe}_2\text{S}_4$  /  $\text{Fe}_2\text{S}_3$  structure. The results of these calculations can be seen in Table 4. For the  $\text{Fe}_2\text{S}_4$  /  $\text{Fe}_2\text{S}_3$  layers on top of an intermediate ferrous layer. The film thickness for  $\text{Fe}_2\text{S}_3$  ( $\text{O}_2$ ) are varied between 1 nm and 10 nm. This is done with the thickness of the  $\text{Fe}_2\text{S}_4$  ( $\text{O}_2$ ) and  $\text{Cu}_2\text{FeS}_4$  ( $\text{O}_2$ ) layers as shown in Table 4. Although the calculated shapes are more consistent with the experimental data and the shift in  $\lambda_{\text{max}}$  due to the thickening of the iron oxide, the detection by ATR and RRS of a copper sulfide compound at or near the surface

cannot be accepted for with this model. Thus, further refinement was necessary since the main deviation is in the range from 1000 to 1500 Å, which shows much higher reflectance than the experimental data.

Table 5.3

Five thickness calculations as a function of the reaction products, their thickness, and their optical refraction

$\text{CuFeS}_2 + 1/2 \text{O}_2 \rightarrow 1/2 \text{Cu}_2\text{FeS}_4 + 1/2 \text{Fe}_2\text{S}_3 + 1/2 \text{Fe}_2\text{S}_2 + 1/2 \text{O}_2$							
		$n_1$	$n_2$	$n_3$	$z$	$L_{\text{min}}$	$R_{\text{min}}$
$\lambda_1$	$\text{Fe}_2\text{S}_3$	2.0	2.4	2.48	12.00	420	0.4
$\lambda_2$	$\text{Cu}_2\text{FeS}_4$	2.75	2.84	2.9	15.00	400	0.2
		18.10	4.8	2.0	20.15	400	1.0
$\lambda_3$	$\text{CuFeS}_2$	18.0	2.80	2.0	21.00	500	1.0
		20.00	4.00	1.0	27.00	500	0.4
	$\text{CuFeS}_2$	20.0	24.00	10.0	30.00	500	1.0

$$n_1^2 = 200 \text{ Å}, \quad n_2^2 = 100 \text{ Å}$$

Another combination of reaction products studied consisted of an intermediate layer that was either  $\text{CuS}$  or  $\text{Fe}_2\text{S}_3$  with an outer iron sulfide layer. Another possibility was to have an copper sulfide with an outer iron sulfide layer. Similar calculations were done using balanced equations as discussed above. In general, these curves deviated much more in both the high and low wavelength regions than either of the previous models. Moreover, the value of thickness suggested that a region between the outer oxide and the bulk chalcopyrite should have been free of iron. This was not observed in the optical profiles. Consequently this series of reaction products were eliminated as being inconsistent with experimental data.

The reaction product arrangement that best fit the experimental data consisted of an inner layer of  $\text{Cu}_2\text{FeS}_4$  in contact with the chalcopyrite, an outer layer of  $\text{Fe}_2\text{S}_3$  and a  $\text{Cu}_2\text{S}$  or  $\text{FeS}$  layer between the iron oxide and the kerolite layer. The series of balanced reactions

equations for this type of a film layer structure and the ratio of the film layer thicknesses of one layer to another are shown in Table 2-4. In these equations, chalcopyrite reacted with oxygen on face A because layer<sub>1</sub> either a covellite or stannite layer, and on face B side. The iron oxide thicknesses were varied between 100 and 2000 which met the thickness of the copper sulfide and the barite layers. The fitted balanced chemical equation in Table 2-4 is for a  $\text{Cu}_2\text{S}$  layer while the second set is for a CuS layer.

Table 2-4

Chemical equations used to calculate thickness ratios between layers designated as barite, chalcopyrite, covellite, and magnetite. The amount of bulk chalcopyrite consumed is designated as  $\text{Cu}_2\text{S}$ .

Compound Formula	Chalcopyrite/ $\text{CuFeS}_2$	Barite/ $\text{Ca}_2\text{FeS}_4$	Covellite/ $\text{Cu}_2\text{S}$	Iron Oxide/ $\text{Fe}_2\text{O}_3$
Thickness	$\text{R}_2$	$\text{R}_3$	$\text{R}_1$	$\text{R}_4$
$\text{CuFeS}_2 + 1.667 \text{R}_2 \rightarrow 17 \text{Cu}_2\text{FeS}_4 + 66 \text{Cu}_2\text{S} + 20 \text{Fe}_2\text{O}_3 + 1.33 \text{O}_2$				
$\text{R}_2 = .667 \text{R}_4 \quad \text{R}_3 = .277 \text{R}_4 \quad \text{R}_1 = .175 \text{R}_4$				



$$\frac{\text{Fe}_2\text{O}_3}{\text{Cu}_2\text{S}}$$

$$\text{R}_4 = \text{Fe}_2\text{O}_3$$

$$\text{R}_1 = \text{Cu}_2\text{S} = \text{R}_2 = \text{CuS}$$

$$\text{R}_3 = \text{Cu}_2\text{FeS}_4$$

Compound Formula	Chalcopyrite/ $\text{CuFeS}_2$	Barite/ $\text{Ca}_2\text{FeS}_4$	Covellite/ CuS	Iron Oxide/ $\text{Fe}_2\text{O}_3$
Thickness	$\text{R}_2$	$\text{R}_3$	$\text{R}_1$	$\text{R}_4$
$\text{CuFeS}_2 + 1.73 \text{R}_2 + .18 \text{Cu}_2\text{FeS}_4 + 54 \text{CuS} + 21 \text{Fe}_2\text{O}_3 + 1.18 \text{O}_2$				
$\text{R}_2 = .41 \text{R}_4 \quad \text{R}_3 = .184 \text{R}_4 \quad \text{R}_1 = .231 \text{R}_4$				

The calculated reflectance curves from the two chemical equilibria shown in Table 5.4 were compared with the experimental reflectance curves in Chapter 4 (see Figures 3.4). Although outer oxide layers of  $\text{Fe}_2\text{P}_4$  and  $\text{FeSiH}$  were studied, the best fits of calculated and experimental reflectance curves were found by using  $\text{Fe}_2\text{P}_4$  as the inner oxide outer layer. The layer between hematite and the outer iron oxide being either  $\text{SiO}_2$  or  $\text{Fe}_2\text{P}_4$  resulted in equally good fits in most cases. This is due to the ratio of thickness of the iron oxide to the outer sulfide which for  $\text{Fe}_2\text{P}_4$  in the outer intermediate layer is 4.46 and for  $\text{SiO}_2$  as the outer intermediate layer is 7.49. However, the majority of the curves were fit with a  $\text{Fe}_2\text{P}_4$  layer. Therefore, the  $\text{Fe}_2\text{P}_4$  layer is very thin and will have a smaller influence on the reflectance curve. Additionally, the presence of  $\text{Fe}_2\text{P}_4$  was necessary both from optical reflectance data and from AAS and XPS data.

When the reaction temperature was increased from 80°C to 400°C, there was a sequential shift of  $\lambda_{\text{max}}$  to higher wavelengths and an increase in the overall reflectance in the region 400-1000 nm. These observations and the modeling work above, suggest that the reaction products are equivalent as the temperature is changed but the extent of reaction is different. However, the reflectance is color and its reflectance curves across the surface show that the reaction was not uniform. By maintaining the same reaction products ( $\text{Fe}_2\text{P}_4$ ,  $\text{SiO}_2$  or  $\text{Fe}_2\text{P}_4$ ,  $\text{Fe}_2\text{P}_4$ ) and only changing thicknesses, the reflectance model yielded reflectance curves which showed a sequential shift of  $\lambda_{\text{max}}$  to longer wavelengths and a shape consistent with the experimental curves. The sequential formation of a broad peak at 420nm-440nm which was seen in

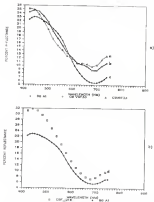


Figure 8.1 Calculated versus experimental reflection curves for specimen 28: a) Isotactic/stereoregular/heptatic (curve 1) Isotactic/heptatic (curve 2) versus experimental (curve 3) and b) Isotactic/heptatic/heptatic (curve 1) versus experimental data (curve 2).

specimens heated at 800°C and 800°C—could only be modeled when the copper sulfide was present between the boronite and copperite layers.

#### Sensitivity Of Calculated Reflectance Curves To Reaction Products

The sensitivity of AR to the copper sulfide and iron oxide layers is demonstrated in Figure 4 in where calculated reflectance data with and without a  $\text{Cu}_2\text{S}$  layer are compared to experimental data from sample 88, heated at 800°C for 2 hours. When the  $\text{Cu}_2\text{S}$  layer is removed from the model, the broad peak at 400nm is not observed and  $\lambda_{\text{max}}$  (wavelength of ARmax) is shifted to 410nm (curve a in Figure 4.1a). Moreover, the curve calculated with  $\text{Cu}_2\text{S}$  present (curve b), fits the experimental data much better. If part of the  $\text{Fe}_2\text{S}_3$  layer is replaced with  $\text{Fe}_2\text{O}_3$  over a boronite layer, a shift in  $\lambda_{\text{max}}$  from 410nm to 400nm is observed along with a large deviation in the low wavelength region for the broad peak at 400nm (see Figure 4.1b, curve c). Obviously, the agreement between experimental and calculated data is poor using these reaction products. In summary, both the intermediate copper sulfide layer and the outer  $\text{Fe}_2\text{S}_3$  layer on top of the boronite layer are necessary to match both the experimental reflectance curves and the AR and DR data.

#### Reflectance Curve Shape Suggests Iron Oxide Thickness

The shape of the slope and magnitude of the reflectance curves can be evaluated by examining the penetration depth of light in the various reaction products. The penetration depth,  $\text{Pen}(z)$  is equal to  $1/4\alpha z$  where  $z$  is the wavelength of the incident light and  $\alpha$  is the extinction (or absorbance) coefficient. Calculated penetration depths are shown in Appendix 3 for each compound. Since the penetration depth for  $\text{Fe}_2\text{S}_3$  at 400nm is 43 nm, optical information comes from the outer iron sulfide layer as well as from the underlying sulfide layers (where penetration



depths,  $d_{\text{eff}}$ , are generally larger than the true value). This is the reason that removal of the upper oxide affected the broad peak at 6000 in Figure 3.1. At  $\lambda_{\text{min}}$ -values, the  $d$  of  $\text{Fe}_2\text{O}_3$  is thin and thus even more optical information is detected from the underlying oxide layer than true light is absorbed by the true oxide. Thus, the shift in  $\lambda_{\text{min}}$  is due to both changes in thickness and changes in the reflectivity of the products contributing to the total reflectance.

It is of interest though to attempt to relate  $\lambda_{\text{min}}$  to the thickness of the reaction layer. By comparing the slopes and percent reflectance of calculated and experimental curves, it was possible to extrapolate back to a film layer thickness and relate the  $\lambda_{\text{min}}$  value to an average thickness for the outer oxide. Of course, this is true only if the thicknesses of the other two layers are constant. A plot of  $\lambda_{\text{min}}$  versus the average thickness of the outer iron oxide is shown in Figure 3.2, where data are shown for an  $\text{Fe}_2\text{O}_3$  outer layer and either  $\text{Cu}_2\text{S}$  or  $\text{CuS}$  inner layer between the oxide and substrate. Obviously, the shift in  $\lambda_{\text{min}}$  and thicknesses of the outer iron oxide layer are correlated. The observed slight correlation between film contributions from the other reaction products ( $\text{Fe}_2\text{S}_3$ ,  $\text{CuS}$ , and  $\text{Cu}_2\text{FeS}_4$ ) to the shift in  $\lambda_{\text{min}}$  as they thicken. Even the thin  $\text{Cu}_2\text{S}$  layer can be important as shown by data in Figure 3.1 where removal of the  $\text{Cu}_2\text{S}$  layer caused  $\lambda_{\text{min}}$  to shift to a lower wavelength even though the oxide layer thickness remained constant.

Another factor which could affect the relationship between  $\lambda_{\text{min}}$  and thickness is the interference between iron and copper ions which can result in an interdiffusion transfer absorption [Fisher]. For most transition metal ions as compared with oxygen, charge transfer occurs in the ultraviolet (UV) portion of the spectrum except for the  $\text{Fe}^{+2}$  ion.

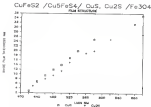


**Figure 8.8** Relationship between film thickness ratio  $L_f/L_0$  for a reaction (cross) or oxidation (plus sign) with time. The data show a linear relationship between  $\ln(L_f/L_0)$  and  $\ln(L_f/L_0)$  for all materials.

a fall of which seems to depend more strongly on the  $\text{Fe}^{+2}$  concentration increase. The effect of the disk thickness,  $d$ , and the concentration or reflection coefficient,  $k$ , are added to the effect of the charge transfer bond.

Further, one can use Figure 4-3 to determine the corresponding thickness of the outer iron oxide layer for a particular value of  $k_{\text{air}}$ . Since the  $\text{Ca}_2\text{S}$  compounds are present, on average of the two calibration curves should be used. The determined iron oxide thickness can then be used to calculate the thickness of the ferrite,  $\text{Ca}_2\text{Fe}_2\text{O}_7$ , and associated oligomers using the relationship shown in Table 3-5.

The iron oxide layers formed at 200°C and 300°C were found to be relatively thick and were uniformly covered the underlying copper substrate. To establish that the thicknesses obtained from the reflectance model were reasonable (see Figure 4-3), a sputtering rate was determined from optical thickness measurements and compared to rates determined from pure iron oxide. In this method, the time required to sputter across the oxide from a sample with  $k_{\text{air}} = 0.0100$  (see Figure 4-3b) was 18 minutes (see Figure 4-3c). From Figure 4-3 for  $k_{\text{air}} = 0.0050$  the iron oxide thickness is approximately 1000, yielding an approximate sputtering rate of about 100 per minute. For a specimen with  $k_{\text{air}} = 0.0020$ , the outer oxide was calculated to be approximately 1000 and the sputter time was 18 minutes which gives a sputter rate of 100 per minute. Similarly, for samples with  $k_{\text{air}} = 0.0010$  and 0.0005, sputter rates of 100 were obtained. These data average to an iron oxide sputter rate of 100 per minute. This compares favorably to the sputtering rate of 10 to 200 per minute for an iron oxide formed in a 20-1000 ppm Fe specimen heated at 200°C and 300°C for 2 hours. This rate was

determined by using a profilometer to measure the step height between the oxidized and unoxidized area and then dividing by the step geometry to equalize across the copper disc the surface.

### Reaction Products

A number of products are possible from the reaction between chalcogenite, copper, and water. The most obvious are oxides such as  $\text{Cu}_2\text{O}$ ,  $\text{Fe}_2\text{O}_3$ , and even mixed oxides  $[\text{FeCu}_x\text{O}_y]$  which are generally called ferrites. The next group of reaction products are the sulfates,  $\text{Fe}(\text{SO}_4)_2$  and  $\text{Fe}(\text{HSO}_4)_2$  which are found in electrochemical reactions and in naturally weathered specimens. A number of copper and iron sulfides are also possible. For example  $\text{CuFeS}_2$ ,  $\text{Cu}_3\text{S}_4$ , and  $\text{Fe}_3\text{S}_4$ . Sulfur can be released as a solid (SFM), as a gas ( $\text{H}_2\text{S}$  or  $\text{SO}_2$ ) and, if enough water is available, as sulfuric acid which can further leach the chalcogenite and help form  $\text{H}_2\text{S}$  (SFM) and sulfate products. The release of  $\text{SO}_2$  has been postulated to be a reaction product in the oxidation of galena, Pb [104]. However, it has been shown that  $\text{SO}_2$  is an intermediate product in the reaction of galena with dry  $\text{O}_2$  at 475°C [105].

The data concerning the reaction products detected by EPMA and AEM as well as SEM were presented earlier. These data were combined to identify the products and their configuration as refinements curves could be calculated. Section II is also launched to discuss the possible occurrence of other reaction products. The formation of ferrites as a reaction product on chalcogenite requires temperatures in excess of 700°C [106] and ferrites are generally avoided in altered specimens if possible due to their insolubility in water. If copper is combined in an insoluble oxide it must be easily separated, but as a sulfide, it is soluble in water and can be separated from the other

reaction products is a working process.  $\text{SnCl}_2$ ,  $\text{FeCl}_2$  and copper metal, Cd, are two other products that form at temperatures above those used in this study and therefore were not considered. Sulfates are more easily formed by oxidation at all temperatures above those used in this study, indicating that sulfates should not be major products, consistent with experimental data.

The sulfide group is by far the most complex and the least understood of the classes of reaction products. There are a number of mixed sulfides as well as copper and iron sulfides as shown in Table 4-4. The iron sulfides are most often found in alloys as very small inclusions within chalcopyrite, if present at all. However, the formation of  $\text{FeS}_2$  is not seen in chalcopyrite due to size restrictions and growth [DUFFIN, 1980C1]. Thus, only the more mixed sulfides found in nature [hematite, malachite, and covellite (CHS02)] were considered as reaction products in this study.

Experimental data from this study established that  $\text{Cu}_2\text{S}$  was not present, based upon XRF and ORE data. Data from XPS cannot be used to establish for  $\text{Cu}_2\text{S}$ , since this oxide does not create a satellite peak for the  $2p_{3/2}$  line. In fact, the  $2p_{3/2}$  spectrum from  $\text{Cu}_2\text{S}$  is consistent to that for  $\text{Cu}_2\text{O}$  [MALAB, 1988C]. To establish for the presence of  $\text{Cu}_2\text{S}$  using ORE, experimental reflectance data were compared with calculated reflectance data where the presence of covellite as a reaction product was minimal. As can be seen from Figure 4-3, the experimental data (curve a) deviate from the calculated data (curve b) when covellite is assumed to be present. The calculated data agree much better when a thin layer of chalcopyrite is used to replace the covellite. Additionally, the necessary shifts in both the  $\text{Cu } 2p$  line and the major limited XPS

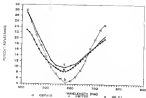


Figure 5.1 Calculated versus experimental (curve 1) reflectance data from species 18 with calculated curve for *Scenedesmus* (curve 2) and for *Strombidium* (curve 3) film layers

lines [FMR], [FMR]) were not observed to indicate the presence of  $\text{Cu}(\text{OH})_2$  or  $\text{Cu}_2\text{O}$ .

Unlike the  $\text{Cu}_2\text{O}$  group, it is much more difficult to clearly distinguish one iron oxide from the other. The iron oxides that were considered in this study are  $\text{Fe}_3\text{O}_4$  (magnetite),  $\text{Fe}_2\text{O}_3$  (hematite), and  $\text{FeOOH}$  (goethite). These compounds are all found as natural elements. However, all data show that  $\text{Fe}_3\text{O}_4$  dominated the reaction products except that water from the air caused a surface hydroxide product (presumably  $\text{FeOOH}$ ) on all samples, especially those reacted at 80°C.

It is not possible to distinguish between goethite and hematite based upon either IR or XPS data. Although IR data could not be used to conclusively determine which copper sulfide is present, the reflectance modeling results suggest chalcocite ( $\text{Cu}_2\text{S}$ ) is the product formed most often. However, the free energy of formation in chlor/acid was negative for  $\text{Cu}_2\text{S}$  than for  $\text{CuS}$ .

#### Intermediate Layer Morphologies

Previous work [GROSS] on polished specimens of chalcocite at room temperature has suggested that an intermediate copper-rich sulfide formed between the outer oxide and substrate as a result of polishing at room temperature. Both the copper-rich sulfide and the outer iron oxide were associated with a mixture of oxides and oxides. A model similar to the present one was used to calculate reflectance data which was then compared with experimental reflectance curves. The outer film sulfide was found to be less than 100 nm thick. It has been shown [GROSS] that if the film is thin or less, a single heterogeneous layer consisting of a mixture of the compounds will yield the same reflectance curves as if the compounds were two separate but parallel homogeneous

layers. While optically thin heterogeneous and homogeneous layers behave similarly, the same is not true for AED and EPR analysis. For example, a thin heterogeneous layer would allow detection of both components by AED and EPR. However, a homogeneous thin layer of the first component over another heterogeneous thin layer of the second component would, in most instances, cause only the first component to be detected by AED or EPR. This iron bearing electrolyte from the second component would be increasingly scattered by the first layer and as a result, an AED or EPR signal would be generated.

Data from AED and EPR indicated that the region intermediate between the oxide and bulk chalcopyrite contained more Fe and S with less Cu (and in some instances S) which could be modeled optically as a copper-rich oxide. However, the spatial distribution of the layers could not be directly discerned from the spectral profile data. This could be due to a inhomogeneous effect in the film layer which is detected as a small oxide with AED. Inhomogeneous could explain the inconsistency in detecting the copper rich oxide layer under the iron oxide. Because of these qualitative pieces of evidence showing that the reaction product thickness varied, it is important to consider the effects of any variable thickness on optical reflectance data.

A nonuniform film thickness (inhomogeneous) over the area was analyzed with DR in averaged in the equation of the reflected intensity from the surface. Assuming two regions with thicknesses that differ by a factor of ten were simultaneously detected over the 10µm area. It is possible to calculate the effect using the reflectance model. This will be accomplished by comparing the reflectance of two films with equal magnetic thicknesses of  $10 \pm 1\mu\text{m}$  with underlying



characteristic and periodic aspects of thicknesses dictated as in Table 2-4. The calculated curves are shown in Figure 2-3 where data are shown for  $\lambda_0 = 540$  m thicknesses of 1, 10, and 100  $\mu$  in curves a, b, and c respectively. At the thickness of the real film varying over dimensions such that light reflected from a film region does not pass through any part of a film region (or vice versa) then reflectance from a film containing equal areas of the two thicknesses can be represented as a simple arithmetical average of the two curves, as is shown in Figure 2-4 (curve d) compared to data from a uniform 100  $\mu$  film (curve e) the largest difference in percent reflectance is between films of 100  $\mu$ , but  $\lambda_{min}$  shifts from 480  $\mu$  to 470  $\mu$ . This suggests that the position of  $\lambda_{min}$  will not be greatly affected by roughness (that is, a variation of film thickness). However, the overall period of reflectance in the region of  $\lambda_{min}$  is different by as much as 50%. Thus, the effect of nonuniform film thickness across the film area tends to be averaged out due to the summation of reflected areas at the photodetector.

The effect of microroughness on the shape of the reflectance curve is secondary to that of varying composition. This conclusion is important because not only did earlier profiles indicate a microroughness of the oxide/substrate interface, but the effect was observed to vary across the surface of heated samples (and even after being blown at 40'p). Thus the oxide thickness obviously varied, and almost certainly varied over the area sampled by the QM. At least in some instances (this effect was disclosed by measuring uniformly colored areas). However, thickness variations over lateral dimensions approaching the wavelength of light will not be revealed using the color as a measure of thickness uniformity.

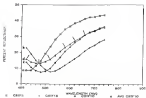


Figure 6-6: Calculated reflectance curves for wavelength/reflectance, negative layer over bulk substrate: a) two negative; b) one negative; c) thin negative; and d) sum of reflectance curves from a) and b) divided by two

### Fractured Versus Polished Specimens

The test data obtained for freshly fractured specimens had values as high as those in contrast to freshly polished specimens. This difference was observed for specimens that were subjected since fracture were present on both types of surfaces after testing. The difference for selected samples is most likely due to the fact that the crack leading to fracture followed a previously existing interface or crack. Thus, reactions leading to oxides may have occurred over anisotropic sites with possible conditions. Anisotropic reactions on fractured surfaces could be detected with the eye as tarnished areas that were distinct from freshly fractured areas which were bright gold in color and similar to freshly polished rhodochrosite.

Both from all point analysis for freshly fractured specimens were found to be equivalent to those of polished specimens. In fact, on a single specimen with both surface preparation procedures, the all three are equivalent. The reflectance curves measured from both fractured and polished specimens were found to be equivalent in shape and overall percent reflectance for areas that showed equivalent tarnishing. The shift in  $\lambda_{min}$  observed as a function of temperature for polished specimens was equivalent to fractured specimens heated at 200°C and 300°C.

In conclusion, the reaction products formed on a fractured surface are equivalent to those of a polished surface as long as the fracture truly revealed a new surface. However, the polishing procedure used in this study did not cause any modifications of the reaction products.

### 6.4.3. Inclusions Present in Both Chalcopyrite Specimens

The major inclusions present in the Le Bure and Ivato specimens were pyrrhotite, arsenicite and/or chalcocite. The presence of pyrrhotite in the Le Bure specimens had no effect upon the general reaction of chalcocite. However, there is an effect of the arsenicite vein which is between the pyrrhotite and the chalcocite. In general, reflectance curves could not be obtained from the copper sulfide inclusions in the Le Bure specimens due to the small width (less than 100 $\mu$ ). For the occasional large section of a vein the effect of CuS is seen as a shift in  $\lambda_{min}$  to longer wavelengths as the point of analysis is moved closer to the interface between chalcocite and arsenicite.

However, the arsenicite region goes through a phase transformation and becomes kersantite which has reaction products that are qualitatively similar to those formed on the chalcocite. The phase transformation to kersantite was determined from XRD data and the reflectance curves from a vein within the bulk material whose width was larger than 100 $\mu$ . This phase transformation is very dramatic for chalcocite veins in Ivato specimens, where it destroys the contrast at the interface between the chalcocite and the chalcocite after heat treatments at 300°C or 350°C (see Figure 4.18). Instead, a melted area is seen where the interface was previously observed. The chalcocite region in contact with this melted area has reflectance curves that had much more dramatic shifts in  $\lambda_{min}$  to higher wavelengths as compared to a region away from a 100 $\mu$  away from the chalcocite/chalcocite interface.

In order for the chalcocite or arsenicite to transform into kersantite iron must diffuse from the chalcocite into the copper sulfide vein. Depleting the iron in the chalcocite is immediate contact with the

higher sulfate values. This deviation of iron from the chloropyrite could arise the reaction since (TSMAG) depicted s-type chloropyrite reacts more quickly. It is known that natural specimens of hornblende include much more quickly to integrated values than the synthesis of chloropyrite (JAHNKE). Consequently, the loss of iron and the formation of a hornblende region in contact with chloropyrite could accelerate the reaction. At 60°C, the reaction products detected with SEM in the hornblende or chloropyrite regions for both the Le Barre and Bette specimens are a thin outer iron oxide. This oxide presumably came from the reaction of chloropyrite since iron was not detected with SEM in the outer sulfate inclusions.

## CHAPTER 5 SUMMARY AND FUTURE WORK

### Summary

Surface sensitive analytical techniques have been utilized to help quantify optical reflectance data from unknown specimens of chalcopyrite reacted in laboratory air between 20°C and 300°C. Auger electron spectroscopy depth profiling gave information concerning the spatial distribution of the film layers while X-ray photoelectron spectroscopy gave information about the surface composition. Due to the complex layer structure and the similarity of many of the sulfide compounds, it was not possible to uniquely distinguish the layer compounds with electron spectroscopy. Since optical properties are unique to a compound, measured reflectance as a function of the wavelength of light is routinely used to identify phases in bulk materials. The use of reflectance data to model film layers on a surface is helpful in assigning the products formed at the surface.

Optical microreflectometry was utilized to measure reflectance data from small areas (10µm in diameter) which could be monitored before and after reaction as a function of time at a specific temperature. The change in reflectance curves from alterations in the surface was related to a series of reaction products. A series of balanced chemical equations were used to determine the relative quantity of the reaction products at the surface. These relative products and their relative quantities were used in a multiple reflectance model to calculate

reflectance curves which were compared to experimental curves in an effort to narrow the possible chemical products.

The film layer structure consisted of an outer iron oxide layer ( $\text{Fe}_2\text{O}_3$ ) or laterite-like chalcoprite ( $\text{Cu}_2\text{S}$  or covellite ( $\text{CuS}$ ) layer between the outer oxide and a kerite ( $\text{Fe}_2\text{Si}_2\text{O}_7$ ) layer, with the kerite being in contact with the bulk chalcoprite ( $\text{FeSFeS}_2$ ). The  $\text{CuS}$  or  $\text{Cu}_2\text{S}$  layer was relatively thin with iron oxide being intermediate and the kerite being the thickest layer. The surface products formed at room temperature consisted of the same compounds as those formed at temperatures of 100°C and 200°C, except that some hydrous species and some sulfate species were formed at elevated temperatures. The total thickness was found to increase greatly with temperature and to a lesser extent with time. At 100°C the film was uniform across the surface and the total film thickness ranged from 10 $\mu$ m to 30 $\mu$ m while at 200°C the thickness ranged from 5 $\mu$ m to 40 $\mu$ m. The reaction products formed at 200°C ranged from less to three in total thickness. The covellite and chalcoprite inclusions were found to transform to a kerite phase which affected only the chalcoprite in direct contact with the inclusion and resulted in no increase in the iron oxide layer thickness. Sulfate inclusions had no observable effect on the reaction of chalcoprite.

Fractured specimens of chalcoprite were analyzed and compared to polished specimens. In general, the reaction products were the same. However—care must be taken with fractured surfaces to avoid areas of stress roughness. Stress fracture surfaces were produced along areas which previously had cracked and reacted over geologic time to form similar products inherent to the sample.

Future Work

Future work in the surface oxidation of chalcopyrite requires a better understanding of the role of dislocations and how they affect the oxidation process. If surface reaction products could be predicted based upon the temperature and the oxidation process, the processing of chalcopyrite could be better controlled. For example, it is easier to process a specimen if it is known to what extent it was oxidized. As seen from this work, by increasing the temperature and time the outer layer is mainly an iron oxide with an intermediate region that is copper rich and present in greater concentration. This is rationalized by chemical reactions which require a certain amount of the bulk chalcopyrite to be consumed. The reactions of chalcopyrite in both reducing atmospheres and inert atmospheres could further help describe the reaction of chalcopyrite and the role of dislocations.

The observations made during the course of this work suggest that the area of fracture analysis with optical microscopatology has great potential in terms of either monitoring a fractured surface or characterizing it with respect to the bulk or a polished specimen. However to realize this, the microscopical factor must be considered due to either immediate reaction or continued reaction at the surface of most compounds including chalcopyrite. Thus, the ability to optically analyze either a fractured or polished surface as a function of time, temperature, or some other variable would require a system capable. Although this would require some exceptional optical components, the potential application could be well worth the work. In order to successfully characterize the reaction products on chalcopyrite one could react them at low temperature in vacuum with copper. The reaction products



would then be analyzed optically in vacuum without added environmental effects, then compared to reaction products forged in air at low temperature.

Monitoring a deposition process for use in studying the optimal properties of known films on a specific substrate can be useful in the development of new thin film models. Because determining changes in the film layers as a function of temperature, rate of deposition, or other deposition variables could be very informative for quality control in deposition processes. It would be quick, non-destructive and fairly inexpensive.

## APPENDIX A REFLECTANCE MODEL CALCULATIONS

The total resulting reflectance  $R^*$ , for a single layer on an absorbing substrate is given below by Eq. A.18. This equation requires normally incident monochromatic light striking a flat surface. The incident light interacts with the surface and emits reflected waves that are due to interaction at the air/substrate boundary and for a film interacting at the film/substrate boundary. The equations for the optical reflectance with normally incident light have been previously discussed for a bulk absorbing solid [FURN,1968], for an unsupported thin absorbing film [FURN], and for thin films on transparent substrates [FURN,1968]. The reflectance model used in this study is good for an absorbing film on an absorbing substrate.

The derivation starts with a determination of the reflectance coefficient from a bulk material. Let  $a$  be the amplitude of the incident wave and  $b_r$  the amplitude of the reflected light after being transmitted through a thin layer deposited at the surface of the substrate. Let  $r_{12}$  and  $t_{12}$  be the reflection and transmission coefficients respectively for the amplitude of the wave moving from medium 1 to medium 2. In the case of absorbing materials, these coefficients are complex with  $b_{12}$  as the phase change between the incident and reflected wave with magnitude  $|r_{12}|$  and related according to

$$b_{12} = -r_{12} = |r_{12}| e^{i\theta_{12}} \quad (A.1)$$

$$t_{12} = 1 - r_{12} = 1 - |r_{12}| e^{i\theta_{12}} \quad (A.2)$$

The reflectance for the normal incidence is then given by

$$R_{\text{th}} = R_{\text{ex}} = r_{\text{th}}^2 r_{\text{ex}}^2 = \int_{\text{th}}^2 \quad (4.3)$$

where  $r_{\text{th}}^2$  is the complex conjugate of  $r_{\text{th}}$ . Considering only normally incident light, the reflectance coefficient may be expressed in terms of the refractive index,  $n$ , as

$$r_{\text{th}} = \frac{n_1 - n_2}{n_1 + n_2} \quad (4.4)$$

For an absorbing material,  $n \neq n' + j\kappa$  is complex and includes the real refractive index,  $n'$ , and the extinction index,  $\kappa$ . Expressing  $n_1$  and  $n_2$  as complex terms, the reflectance is given by

$$R_{\text{th}} = \frac{(n_1 - n_2)^2 + (\kappa_1 - \kappa_2)^2}{(n_1 + n_2)^2 + (\kappa_1 + \kappa_2)^2} \quad (4.5)$$

The absorption coefficient,  $\alpha = \kappa_2 / n_2$ , can be defined and  $\kappa_2$  is written entirely in terms of  $n_2$  and  $\alpha_2$  if so desired. The phase change,  $\phi_{\text{th}}$ , between the reflected and incident wave is given by

$$\tan(\phi_{\text{th}}) = \frac{2(n_1 - n_2)(\kappa_2 - \kappa_1)}{(n_1^2 - n_2^2) + (\kappa_1^2 - \kappa_2^2)} \quad (4.6)$$

The sign of  $\tan(\phi_{\text{th}})$  is defined by considering separately the two quantities  $\sin(\phi_{\text{th}})$  and  $\cos(\phi_{\text{th}})$  derived from the complex representation of the reflection coefficient ( $r_{\text{th}}$ ). The ranges of  $\phi_{\text{th}}$  are shown in Table A.1 for various combinations and values of the optical constants. Note that when the index  $i$  refers to air ( $n_i = 1$ ,  $\kappa_i = 0$ ), the phase change  $\phi_{\text{th}}$  due to reflection from an absorbing material ranges from  $\pi/2$  to  $\pi$  in the case of a transparent material,  $(n_2 > 1 \geq \kappa_2 = 0)$  the phase change is equal to  $\pi$ .

Table 2.1

Range of phase change versus complex optical constants of the substrate and surface layer

$n_{\text{sub}}$	$n_2, n_h > n_h, n_1$	$n_2, n_h < n_h, n_1$
$\frac{n_1^2 + n_2^2}{n_h^2 + n_h^2} > 1$	$0 < \delta_{\text{th}} < \pi/2$	$\pi/2 < \delta_{\text{th}} < \pi$
$\frac{n_1^2 + n_2^2}{n_h^2 + n_h^2} < 1$	$\pi/2 < \delta_{\text{th}} < \pi$	$0 < \delta_{\text{th}} < \pi/2$

After deriving the reflection for a bulk substrate, the next step is to arrive at an equation for an unsupported film (see Figure A.1). This comes from the derivation of a thin film on a transparent substrate, assuming that the surfaces are perfectly parallel in the transparent layer. Transmission wave amplitudes are such that the optical refractive index may be different on one side of the layer versus the other side.

The complex amplitude of the wave reaching the detector is the sum of the amplitudes of all the successive reflected waves,  $R_{\text{th}}$ , which can be expressed by an arithmetical progression containing the factor  $r_{\text{th}} r_{\text{th}}^{*} e^{-2\delta_{\text{th}}}$  where  $\delta$  denotes the incident medium,  $l$  denotes the layer,  $0$  denotes the transmission medium, and  $\delta_l$  is the phase change resulting from optical path differences. The complex amplitude of the resulting reflected wave,  $R_{\text{th}}^*$ , is

$$R_{\text{th}}^* = \frac{r_{\text{th}}^* (1 + r_{\text{th}} e^{-2\delta_{\text{th}}})}{1 - r_{\text{th}}^* r_{\text{th}} e^{-2\delta_{\text{th}}}} = r_{\text{th}}^* (1 + r_{\text{th}} e^{-2\delta_{\text{th}}}) \quad (\text{A.7})$$



The complex amplitude of the resulting transmitted wave,  $R_0^+$ , is then

$$R_0^+ = \frac{a(t_{12} + 1 + a(t_{12} + e^{i\theta_1}))}{1 + r_{12} r_{12}^* e^{i\theta_1}} \quad (4.6)$$

The argument  $\theta_1$  represents the phase change resulting from optical path differences through the layer of thickness  $d$  above.

$$\theta_1 = 2\pi d/\lambda_1 \quad (4.7)$$

The phase  $\theta_1$  refers to the first reflected beam from the surface where  $\lambda_1$  is the wavelength of light. Phase changes upon reflection are included within the complex reflection coefficient for the amplitude. The total reflected intensity,  $I_R$ , and transmitted intensity,  $I_T$ , measured at the interface are

$$I_R = |R_0^+|^2 = |R_0^-|^2 = r^2 \quad (4.8)$$

and

$$I_T = |R_0^+|^2 = |R_0^-|^2 = t^2 \quad (4.9)$$

where the complex amplitude is designated as  $R_0^+$  and  $R_0^-$  for an absorbing substrate ( $k \neq 0$ ) and  $R_0 = R_{12}$  are complete transmissions for the reflection coefficient since the incident and the transmission media against the layer may be different and the transmission media may be either transparent or absorbing.

Substituting Eq. 4.1 and Eq. 4.6 into Eq. 4.7, the amplitude of the total reflected wave is

$$R_0^+ = (a) \frac{(t_{12}^2 + t_{12}^* + \frac{\cos \theta_1 r_{12}^*}{a} + \frac{1}{a} \frac{1}{t_{12}} - \frac{\cos \theta_1 r_{12}^*}{a})}{1 + \frac{t_{12}^*}{t_{12}} + \frac{\cos \theta_1 r_{12}^*}{a} + \frac{1}{a} \frac{1}{t_{12}} + \frac{1}{a} \frac{1}{t_{12}} - \frac{\cos \theta_1 r_{12}^*}{a}} \quad (4.10)$$

According to Eq. 4.18 the resulting reflection coefficient,  $R^*$ ,

for the layer on a substrate is then given by

$$R^* = \frac{R_{11} + R_{22} e^{2i\delta} + 2(R_{12} R_{21})^B e^{iA} \cos(\delta_{11} - \delta_{22} - \cos\alpha_1 \beta_1/\lambda)}{1 + R_{11} R_{22} e^{2i\delta} + 2(R_{12} R_{21})^B e^{iA} \cos(\delta_{11} + \delta_{22} - \cos\alpha_1 \beta_1/\lambda)} \quad (4.19)$$

where  $A = -4\pi\alpha_1 \beta_1/\lambda$ .

Coefficients  $R_{11}$  and  $R_{22}$  are for the various layer and substrate with both sides values of  $n_1$  and  $n_2$  [Eq. 4.12]. Phase changes  $\delta_{11}$  and  $\delta_{22}$  due to reflection are calculated from equations similar to Eq. 4.8. The total phase change,  $\delta^*$ , between the incident and the total reflected wave includes changes due to reflection and to optical path differences [see Eq. 4.18]. Multiplying the numerator and denominator of Eq. 4.19 by the complex conjugate of the denominator and isolating the real and imaginary parts leads to equations for the value of  $R^*$  given by

$$R^*_{\text{real}} R^* = \frac{(R_{11})^2 + (1 - R_{22}) e^{2i\delta} \cos \delta_{11} + (R_{22})^B e^{iA} \cos (\delta_{22} - \delta)}{1 + R_{11} R_{22} e^{2i\delta} + 2 (R_{11} R_{22})^B e^{iA} \cos (\delta_{11} + \delta_{22} - \delta)} \quad (4.20)$$

and

$$R^*_{\text{imag}} R^* = \frac{(R_{11})^2 + (1 - R_{22}) e^{2i\delta} \cos \delta_{11} + (R_{22})^B e^{iA} \cos (\delta_{22} - \delta)}{1 + R_{11} R_{22} e^{2i\delta} + 2 (R_{11} R_{22})^B e^{iA} \cos (\delta_{11} + \delta_{22} - \delta)} \quad (4.21)$$

where  $\delta = -4\pi\alpha_1 \beta_1/\lambda$ .

Reflections and transmissions of a transparent substrate covered with multiple homogeneous layers has been previously discussed [TYRRELL; TOMSON].

[TYRRELL; TOMSON] For absorbing materials, Eq. 4.18 can easily be extended to a description of multiple thin absorbing layers superimposed on top of each other on the substrate.

Let the substrate be labelled 0 and each successive layer labelled 1, 2, ..., p-1 where p-1 is air as shown in Figure 4.2. The substrate is covered with a single layer may be considered from a reflection point of view as a single equivalent substrate with a complex reflection coefficient of amplitude  $r^*$  derived from Eq. 4.2. For the following demonstration, the coefficient  $r^*$  will be assumed as  $r_{0,2(1),0}^*$  indicating that the coefficient is equivalent to that of the original material covered with a single layer placed in air. Assuming this equivalent substrate is again covered with a thin layer (2) and placed in air (1) the reflection coefficient for two layers would be

$$r_{0,2(2,1),0}^* = \frac{r_{02}^* + r_{0,2(1),0}^* e^{-j2\beta_2}}{1 + r_{02}^* r_{0,2(1),0}^* e^{-j2\beta_2}} \quad (4.10)$$

By an iterative procedure we may calculate the reflection coefficient for a substrate covered with p successive layers as the reflection of a single layer p deposited on top of a substrate equivalent to the original substrate with p-1 layers. The outer layer is in contact with air. This procedure was used to calculate reflectance curves with three homogeneous layers on top of a substrate.

A program was written in basic language to calculate the percent reflectance as a function of wavelength. The iterative procedure described above was utilized in the program (BROWNE BAS) shown below starting at line 1100. Note that the labelling of the successive layers started at 1 for air with 2 designating the third outer layer and 3 designating the intermediate layer. Thus, the substrate was labelled 0. In program BROWNE BAS below, in addition to the calculations a plotting routine, starting at line 1600, was written to record the



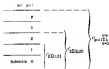


Figure 6.4 Equivalent reflection conditions for the synthesis for a substrate covered with multiple superimposed thin layers

calculations according to Eilenberg data, layer structure and the thickness of the films.

The variables requested in order to run the program are: a Eilenberg data file and a values (or all and all values) of the compound for the first through the third layer. The thickness of each layer must be input in nanometers in the order requested. The  $n$  and  $k$  values for each compound are stored in a sequential file in two programs called `REFRIND` and `EXTCOEF` and which is called by `REFRIND` but at the request of the all and all values input by the operator.

The  $n$  and  $k$  values were derived from air and all reflectance measurements obtained from the DR/COM data for the silver of interest. The Roushpfelberger [2100] equations were used to calculate the  $n$  and  $k$  values from the reflectance measurements in all and all as a function of wavelength. A separate program was written for these calculations for each compound of interest. The Roushpfelberger equations are as follows:

$$R_{\text{air}} = \frac{R_{\text{all}}^2 - 1}{R_{\text{all}}(1 + R_{\text{all}})} \frac{(1 + R_{\text{air}})}{(1 - R_{\text{all}})} \quad (A.17)$$

and

$$|n'|^2 R_{\text{air}} = \frac{1 - (1 + R_{\text{air}})}{1 - (1 - R_{\text{air}})} = \frac{n'^2 - 1}{n'^2} \quad (A.18)$$

These two equations are simultaneously solved when given the value of all  $R_{\text{all}}$ -values for the reflectance in air  $R_{\text{air}}$  and all  $R_{\text{all}}$  as a function of wavelength.

The program `REFRIND` but is described below in the form input as a file in basic. This can be run on any IBM PC compatible computer.



```

300 INPUT "WHAT IS THE FIRST CORNER POINT OF NO. 1?" X1,Y1
310 INPUT "WHAT IS THE SECOND CORNER POINT OF NO. 1?" X2,Y2
320 INPUT "WHAT IS THE THIRD POINT OF NO. 1?" X3,Y3
330 INPUT "WHAT IS THE COORDINATE OF NO. 1?" X4,Y4
340 PRINT "....."
350 DIM A(1)
360 PRINT "  1   2   3   4   5   6   7   8   9"
370 PRINT "  10  11  12  13  14  15  16  17  18"
380 PRINT "  19  20  21  22  23  24  25  26  27"
390 PRINT "  28  29  30  31  32  33  34  35  36"
400 G= 1: H= 1: I= 1
410 G= 1: H= 1: I= 1
420 G= 1: I= 1
430 IF X1= "X111" AND Y1= "Y111" THEN G= 1: H= 1
440 IF X1= "X112" AND Y1= "Y112" THEN G= 1: H= 2
450 IF X1= "X113" AND Y1= "Y113" THEN G= 1: H= 3
460 IF X1= "X114" AND Y1= "Y114" THEN G= 1: H= 4
470 IF X1= "X115" AND Y1= "Y115" THEN G= 1: H= 5
480 LET X2(J)=X2:Y2(J)=Y2: LET X3(J)=X3:Y3(J)=Y3: LET X4= "A-POINT-1"
490 LET X1(J)=X1:Y1(J)=Y1: LET X2(J)=X2:Y2(J)=Y2: LET X3= "A-POINT-2"
500 LET X1(J)=X1:Y1(J)=Y1: LET X2(J)=X2:Y2(J)=Y2: LET X3= "A-POINT-3"
510 LET X1(J)=X1:Y1(J)=Y1: LET X2(J)=X2:Y2(J)=Y2: LET X3= "A-POINT-4"
520 IF X1= "X111" AND Y1= "Y111" THEN G= 1: H= 1
530 IF X1= "X112" AND Y1= "Y112" THEN G= 1: H= 2
540 IF X1= "X113" AND Y1= "Y113" THEN G= 1: H= 3
550 IF X1= "X114" AND Y1= "Y114" THEN G= 1: H= 4
560 IF X1= "X115" AND Y1= "Y115" THEN G= 1: H= 5
570 LET X1(J)=X1:Y1(J)=Y1: LET X2(J)=X2:Y2(J)=Y2: LET X3= "A-POINT-1"
580 LET X1(J)=X1:Y1(J)=Y1: LET X2(J)=X2:Y2(J)=Y2: LET X3= "A-POINT-2"
590 LET X1(J)=X1:Y1(J)=Y1: LET X2(J)=X2:Y2(J)=Y2: LET X3= "A-POINT-3"
600 LET X1(J)=X1:Y1(J)=Y1: LET X2(J)=X2:Y2(J)=Y2: LET X3= "A-POINT-4"
610 LET X1(J)=X1:Y1(J)=Y1: LET X2(J)=X2:Y2(J)=Y2: LET X3= "A-POINT-1"
620 LET X1(J)=X1:Y1(J)=Y1: LET X2(J)=X2:Y2(J)=Y2: LET X3= "A-POINT-2"
630 LET X1(J)=X1:Y1(J)=Y1: LET X2(J)=X2:Y2(J)=Y2: LET X3= "A-POINT-3"
640 LET X1(J)=X1:Y1(J)=Y1: LET X2(J)=X2:Y2(J)=Y2: LET X3= "A-POINT-4"
650 LET X1(J)=X1:Y1(J)=Y1: LET X2(J)=X2:Y2(J)=Y2: LET X3= "A-POINT-1"
660 LET X1(J)=X1:Y1(J)=Y1: LET X2(J)=X2:Y2(J)=Y2: LET X3= "A-POINT-2"
670 LET X1(J)=X1:Y1(J)=Y1: LET X2(J)=X2:Y2(J)=Y2: LET X3= "A-POINT-3"
680 LET X1(J)=X1:Y1(J)=Y1: LET X2(J)=X2:Y2(J)=Y2: LET X3= "A-POINT-4"
690 LET X1(J)=X1:Y1(J)=Y1: LET X2(J)=X2:Y2(J)=Y2: LET X3= "A-POINT-1"
700 LET X1(J)=X1:Y1(J)=Y1: LET X2(J)=X2:Y2(J)=Y2: LET X3= "A-POINT-2"
710 LET X1(J)=X1:Y1(J)=Y1: LET X2(J)=X2:Y2(J)=Y2: LET X3= "A-POINT-3"
720 LET X1(J)=X1:Y1(J)=Y1: LET X2(J)=X2:Y2(J)=Y2: LET X3= "A-POINT-4"
730 LET X1(J)=X1:Y1(J)=Y1: LET X2(J)=X2:Y2(J)=Y2: LET X3= "A-POINT-1"
740 LET X1(J)=X1:Y1(J)=Y1: LET X2(J)=X2:Y2(J)=Y2: LET X3= "A-POINT-2"
750 LET X1(J)=X1:Y1(J)=Y1: LET X2(J)=X2:Y2(J)=Y2: LET X3= "A-POINT-3"
760 LET X1(J)=X1:Y1(J)=Y1: LET X2(J)=X2:Y2(J)=Y2: LET X3= "A-POINT-4"
770 LET X1(J)=X1:Y1(J)=Y1: LET X2(J)=X2:Y2(J)=Y2: LET X3= "A-POINT-1"
780 LET X1(J)=X1:Y1(J)=Y1: LET X2(J)=X2:Y2(J)=Y2: LET X3= "A-POINT-2"
790 LET X1(J)=X1:Y1(J)=Y1: LET X2(J)=X2:Y2(J)=Y2: LET X3= "A-POINT-3"
800 LET X1(J)=X1:Y1(J)=Y1: LET X2(J)=X2:Y2(J)=Y2: LET X3= "A-POINT-4"
810 LET X1(J)=X1:Y1(J)=Y1: LET X2(J)=X2:Y2(J)=Y2: LET X3= "A-POINT-1"
820 LET X1(J)=X1:Y1(J)=Y1: LET X2(J)=X2:Y2(J)=Y2: LET X3= "A-POINT-2"
830 LET X1(J)=X1:Y1(J)=Y1: LET X2(J)=X2:Y2(J)=Y2: LET X3= "A-POINT-3"
840 LET X1(J)=X1:Y1(J)=Y1: LET X2(J)=X2:Y2(J)=Y2: LET X3= "A-POINT-4"
850 LET X1(J)=X1:Y1(J)=Y1: LET X2(J)=X2:Y2(J)=Y2: LET X3= "A-POINT-1"
860 LET X1(J)=X1:Y1(J)=Y1: LET X2(J)=X2:Y2(J)=Y2: LET X3= "A-POINT-2"
870 LET X1(J)=X1:Y1(J)=Y1: LET X2(J)=X2:Y2(J)=Y2: LET X3= "A-POINT-3"
880 LET X1(J)=X1:Y1(J)=Y1: LET X2(J)=X2:Y2(J)=Y2: LET X3= "A-POINT-4"
890 LET X1(J)=X1:Y1(J)=Y1: LET X2(J)=X2:Y2(J)=Y2: LET X3= "A-POINT-1"
900 LET X1(J)=X1:Y1(J)=Y1: LET X2(J)=X2:Y2(J)=Y2: LET X3= "A-POINT-2"
910 LET X1(J)=X1:Y1(J)=Y1: LET X2(J)=X2:Y2(J)=Y2: LET X3= "A-POINT-3"
920 LET X1(J)=X1:Y1(J)=Y1: LET X2(J)=X2:Y2(J)=Y2: LET X3= "A-POINT-4"
930 LET X1(J)=X1:Y1(J)=Y1: LET X2(J)=X2:Y2(J)=Y2: LET X3= "A-POINT-1"
940 LET X1(J)=X1:Y1(J)=Y1: LET X2(J)=X2:Y2(J)=Y2: LET X3= "A-POINT-2"
950 LET X1(J)=X1:Y1(J)=Y1: LET X2(J)=X2:Y2(J)=Y2: LET X3= "A-POINT-3"
960 LET X1(J)=X1:Y1(J)=Y1: LET X2(J)=X2:Y2(J)=Y2: LET X3= "A-POINT-4"
970 LET X1(J)=X1:Y1(J)=Y1: LET X2(J)=X2:Y2(J)=Y2: LET X3= "A-POINT-1"
980 LET X1(J)=X1:Y1(J)=Y1: LET X2(J)=X2:Y2(J)=Y2: LET X3= "A-POINT-2"
990 LET X1(J)=X1:Y1(J)=Y1: LET X2(J)=X2:Y2(J)=Y2: LET X3= "A-POINT-3"

```

[illegible]



















L	SPR200-01	SPR200-02	SPR200-03	SPR200-04
200	0.44	0.430	0.43	1.39
400	0.77	0.460	0.44	1.04
600	0.60	0.540	0.45	1.18
800	0.57	0.490	0.44	0.84
1000	0.47	0.490	0.43	0.83
1200	0.39	0.460	0.44	0.79
1400	0.34	0.440	0.43	0.88
1600	0.30	0.500	0.44	0.84
1800	0.26	0.460	0.44	0.40
2000	0.34	0.400	0.44	0.37
2200	0.28	0.400	0.43	0.37
2400	0.24	0.440	0.47	0.20
2600	0.24	0.430	0.44	0.39
2800	0.44	0.400	0.70	0.27
3000	0.34	0.400	0.70	0.39
3200	0.40	0.400	0.85	0.34
3400	0.43	0.400	0.84	0.34

The penetration depth for each compound can be calculated from the extinction coefficient,  $\kappa$ , by  $1/\kappa \times (2\pi \times \text{wavelength of light})$  as shown in Table A.1 and Table A.2. The penetration depths recorded in Table A.1 and Table A.2 are calculated from the underlying layers for a thickness of the solar ion-oxide layer in the reflectance model calculation is being selected.

Table A.1

Penetration depths (in nm) for copper compounds as a function of  $L$  (nm)

L	$\text{Cu}_2\text{O}$	$\text{Cu}_2\text{FeS}_4$	$\text{Cu}_2\text{S}$	$\text{Cu}_2\text{Se}$	$\text{Cu}_2\text{Te}$
200	20.0	20.7	20.0	40.1	27.0
400	27.3	42.0	24.7	81.4	100.0
600	24.0	40.0	28.1	80.0	27.7
800	22.7	40.0	32.0	140.7	41.5
1000	20.0	40.1	38.7	151.0	50.0
1200	18.1	40.4	32.7	171.0	104.0
1400	16.0	40.0	40.1	160.0	120.0
1600	14.0	38.7	40.7	140.0	81.1
1800	14.0	37.0	41.0	140.4	80.4
2000	17.0	38.0	42.0	120.0	50.4
2200	14.0	38.0	41.0	114.4	57.0
2400	14.0	34.0	40.0	80.7	40.0
2600	10.0	32.0	38.0	70.0	47.0
2800	10.0	34.0	38.0	47.1	70.0
3000	10.0	30.0	34.0	40.0	70.0
3200	11.0	34.0	30.0	40.0	85.0
3400	10.1	37.0	31.0	40.0	40.0

Table A.2

Protonium depths (in nm) for iron deposits as a function of  $L$  (nm).

$L$	$Fe_{\alpha}d_{\alpha}$	$Fe_{\beta}d_{\beta}$	$Fe_{\gamma}d_{\gamma}$	$Fe_{\delta}d_{\delta}$	$Fe_{\epsilon}d_{\epsilon}$
400	27.6	46.6	76.6	111.6	158.7
450	40.7	53.6	86.6	124.4	176.6
490	48.6	63.6	99.6	137.6	191.6
530	55.4	706.3	113.3	150.4	197.6
580	62.3	846.7	130.6	166.6	43.3
620	66.7	147.6	146.6	171.7	56.6
740	73.3	166.4	176.6	181.1	61.1
840	80.6	186.3	203.7	191.6	66.6
940	87.6	204.6	246.4	191.7	207.3
1050	94.6	199.1	234.7	191.6	226.3
1150	101.6	186.6	266.7	191.6	183.7
1240	111.6	200.7	266.6	191.6	206.6
1440	96.6	236.1	266.6	96.6	203.6
1550	96.6	206.1	266.6	155.7	206.4
1640	96.6	206.6	267.7	166.6	156.7
1740	114.6	206.7	266.1	177.3	166.6
1840	116.6	206.6	266.6	186.6	175.6









```

1110 *****
1120 "          REMOVE SACKLES FROM ROVER
1130          STOP MOVING FROM ROOM TO ROOM
1140 *****
1150 MOV=100: NTRY=0: NRM=0
1160 NTRY= CRRS(1R) + CRRS(2R) + CRRS(3R) + CRRS(4R)+ CRRS(5R)
1170 +CRRS(6R)
1180 CALL IPRINT(CRRS,NTRY)
1190 PRINT "***** ROOM *****"
1200 PRINT PRINT "CHECK THAT MICROSCOPES ARE AT ROOM FOR NEXT ROOM"
1210 PRINT PRINT "CHECK LIGHT FOR LIGHT ON (AND CHECKED BLANKING)"
1220 PRINT "*****"
1230 CRRS= "0": CALL IPRINT(CRRS,CRRS)
1240 CALL ILOC(MOV): CALL ILOC(CAPAC)
1250 'PRINT "ROOM DETECTED IN ROOM COVERED"
1260 'PRINT MOV(1:5), MOV(6:10), MOV(11:15)
1270 END

```

## APPENDIX C COPPER SULFIDE INCLUSION ANALYSIS

Inclusions in the form of veins of chalcophyllite and arsenophyllite were found in the matrix and in three specimens, respectively. The reaction of iron impregnations for these inclusions resulted in a line to two thick iron oxide layers deposited with AHS, most likely due to the reaction of the chalcophyllite in contact with the inclusion resulting in Fe diffusing to the vein. No iron was detected in the bulk of the inclusion before leaching by analysis with the electron probe micro-analyzer.

The reaction of these inclusions at 1000°C and 900°C was found to be dramatically different than at 800°C. At these temperatures the inclusions were transformed to a boudin phase. The iron diffused from the chalcophyllite in direct contact with the inclusions into the inclusions. Specimens with both pyrite (FeS<sub>2</sub>) and copper sulfide inclusions and those having only the copper sulfide inclusions were studied. The inclusions transformed to boudin in both cases. These phases were identified both with electron microprobe data and by comparing reflectance ratios with reference data for boudin. In addition, laser Raman spectroscopy data confirmed that the CuS<sub>2</sub> veins and FeS<sub>2</sub> veins were associated with both boudins.

The effect of the transformation on the subsequent reaction between the bulk chalcophyllite and atmosphere is not clear. Since the interface between them has been become topographically very rough, it was not

strictly specify what phase (the inclusion or the bulk chalcopyrite) was contributing to the surface products. Due to surface roughness the reflectance data must be used only qualitatively rather than quantitatively. Furthermore, reflectance scattering is not possible due to the porosity of the materials to be used in the calculation. An attempt was made to write chemical equations for reactions between the furnace and the chalcopyrite which would result in copper sulfides and iron oxides. However there were too many combinations and insufficient reflectance data.

The reactions at 1000°C were equivalent to those observed at 1000°C. The reaction of the bulk chalcopyrite was found to be independent of the pressure of the inclusions. If the area was further than approximately 10µm to either way from the copper sulfide inclusion. However, the Auger depth profiling data suggest that the reaction layer had an outer iron oxide with an intermediate copper-rich sulfide region. The intermediate region could not be clearly distinguished from the bulk and this region could not be further characterized with reflectance calculations. Thus the effects of inclusions upon the reactions was very local but very significant. The significance of inclusions upon the general reaction was dependent upon the density of inclusions in the sulfide.

# BIBLIOGRAPHY

- 12802 J. Kockingsberger, *Ann. Phys.* **44** (1915) 149
- 17581- F. H. Gullit, *Ann. Sci.* **12** (1917) 399
- 18202- F. Meyer, *J. Phys. Chem.* **5** (1910) 458
- 20512 E. Christen and F. F. Knecht, *Ann. Chem.* **40** (1911) 431
- 27122- E. H. Schmitt, *Ann. Chem.* **52** (1927) 82
- 31222- E. H. Schmitt, *Ann. Chem.* **58** (1927) 187
- 32742 L. Felling and L. G. Henschel, *J. Biol.* **41** (1922) 349
- 37522 E. E. Menden and E. E. Lambert, *Ann. Chem.* **50** (1927) 382
- 37712- E. Tichen, *Ann. Chem.* **58** (1928) 308
- 38222 L. G. Austin, C. E. L. Graham and A. E. Fongelly, *J. Electrochem. Soc.* **100** (1953) 485
- 38712- J. E. Miller and E. F. Fongelly, *J. Biol.* **54** (1925) 348
- 39022- J. G. L. Miller, L. M. Collins, J. G. E. Goss, E. Collins and J. E. Fongelly, *Phys. Rev.* **112** (1936) 187
- 40022- E. Goss and E. Fongelly, *Rev. J. of Appl. Physics* **4** (1933) 474
- 44022 C. E. L. Graham, *J. Phys. Chem. Solids* **5** (1935) 308
- 44222 J. Goss, *J. Biol. and Chem.* **5** (1935) 417
- 44722 A. J. Fongelly, *J. The Amer. Mineral.* **44** (1955) 1825
- 44822 E. Goss, E. E. Phillips and J. C. Phillips, *Phys. Rev. Lett.* **5** (1955) 88
- 44912 E. Fongelly and E. E. Phillips, *Ann. Chem.* **48** (1955) 347
- 44922 E. A. Fongelly and E. Fongelly, *J. Polym. Sci.* **1** (1955) 411
- 44932 E. Goss and E. E. Phillips, *Phil. Mag. (London)* **10** (1955) 384

- 10000- F. Corvelli, C. Levy and B. Coge. *Bull. Soc. Fr. Mineral. Cristallogr.* , 81 (1958) 488
- 10001- B. B. Gundersen and B. J. Wroblewski. *J. Chem. Phys.* 4, (1958) 1007
- 10002- L. A. Serfaty. *J. of Appl. Phys.* 30 (1959) 1618
- 10003- R. Smolke and E. Kohn. *Ann. Chem.* 2, 62 (1959) 427
- 10004- S. H. Tscham. *Brit. J. Appl. Phys.* (J. Phys. C) 1, Ser. 2 (1959) 1007
- 10005- E. A. Niekampski and J. C. Wenzel. *Can. J. of Phys.* 38 (1960) 489
- 10006- E. A. Rame and R. J. Vaughan. *Ann. Miner.* 35 (1970) 1075.
- 10007- L. V. Farkas and R. A. King. *R. S. Bureau Min. Geol. Inv. 7021*. New York (1970).
- 10008- R. E. Hall, J. B. Sellschop and C. J. Linderoff. *Met. Sci.* 2 (1971) 286.
- 10009- C. E. Burkhart Jr. *Geol. S. Bureau of Mineralogy*. *Min. of. Ind. Water and Enrg. Inv.* New York. (1971)
- 10010- J. E. Kane and J. L. Long. *Phys. Rev. B* 3 (1971) 444
- 10011- J. Schae, J. B. Thomas and R. W. Springer. *Earth Planet. Sci. Lett.* 10 (1970) 428
- 10012- D. C. Frost, A. Ishizumi and C. A. McComell. *Sci. Phys.* 35 (1970) 961.
- 10013- E. W. Ross, J. F. Green and G. J. Saylor III. *J. of Appl. Phys.* 42 (1970) 1803
- 10014- R. T. Soderstrom Jr. and L. Wilson. *Earth Planet. Sci. Lett.* 10 (1970) 39
- 10015- R. W. Ross, L. J. Saylor and J. B. Gill. *Can. J. Earth Sci.* 9 (1970) 1088
- 10016- J. W. Steadley. *Use of the Differential Reflectometry in the Study of Thin Film Oxidation Products on Copper and Monocrystalline Thin of Fe* (1970) 1
- 10017- R. L. Soderstrom. *Minerals Sci. Eng.* 6 4 (1971) 85.
- 10018- F. Neuber. *Optical Properties of Solids*. Academic Press. New York (1971) 7
- 10019- P. B. Barlow. *Ann. Chem.* 68 (1971) 655.

- 7000- L. J. Carter, *Ann. Phys.*, **58** (1971) 603.
- 7001- B. Chao, Contributions to Relativistic Quantum Mechanics and Quantum Field Theory, Vol. 1, North-Holland, Amsterdam, 1971, p. 1.
- 7002- W. A. Poynter, J. S. Flax, W. B. Riegman and W. B. Robertson, *Rev. Sci. Instrum.*, **42** (1971) 1688.
- 7003- T. G. Worring, *Can. J. Math.*, **19** (1971) 153.
- 7004- B. J. Stone and E. B. Semon, *Nucl. Sci. Eng.*, **31** (1971) 3.
- 7005- C. B. Brundin, *J. of The. Sci. and Tech.*, **11** (1971) 613.
- 7007- J. B. Gribben and R. J. C. Macdonald, *Nucl. Sci. Eng.*, **33** (1971) 50.
- 7008- P. E. Lacey, *J. of Nuclear Sci. and Tech.*, **8** (1971) 112.
- 7009- C. Meish and J. Lajo, *J. Colloid Interface Sci.*, **37** (1971) 666.
- 7010- T. Yamashita, *J. Phys. Soc. Jap.*, **34** (1971) 219.
- 7011- T. Yamashita, K. Kato and K. Kondo, *J. of Phys. Soc. Japan*, **35** (1971) 2338.
- 7012- W. B. Clifford, R. L. Hardy and J. B. Miller, *A. I. Chem. Eng. Ser.*, **71** (1971) 138.
- 7017- R. Bell and R. Macdonald, *Can. J. Sci.*, **18** (1971) 108.
- 7018- P. W. Holloway, *Adv. in Elec. and Electron. Phys.*, **18** (1971) 311.
- 7021- R. B. Krieger and M. K. Gosh, *Can. J. Chem.*, **47** (1971) 3339.
- 7022- R. Morasini, *Can. J. Sci.*, **18** (1971) 138.
- 7023- R. Ben, J. P. Landon and R. W. Dierker, *Can. J. Sci.*, **18** (1971) 541.
- 7024- R. Gosh and R. J. Macdonald, *Can. J. Sci.*, **18** (1971) 143.
- 7025- I. Sakai, M. Oyama, Y. Nagatsu, Y. Kato and K. Suganaka, *Nucl. J.*, **8** (1971) 126.
- 7026- I. Sakai, M. Oyama, Y. Nagatsu, Y. Kato and K. Suganaka, *Nucl. J.*, **8** (1971) 130.
- 7027- G. P. McManis and R. T. Choe, *Nucl. Sci. Eng.*, **33** (1971) 348.



- TM600- R. E. Thomas, Amer. Miner., 61 (1976) 289.
- TM61F- R. Taki and T. Terasaki, J. of Phys., Soc. Japan, 46 (1978) 162.
- TM62- R. Terasaki, J. Miners. Spec. Elev., 1 (1976) 181.
- TM63A- R. Tami and K. Washimoto, Conf. Ser., 17 (1977) 389.
- TM64T- R. Tani and J. Fendler, IMA, Characterizing the Ore Microscopy Quantitative Data File, Card 80 1188 (1979).
- TM65T- R. Tani and J. Fendler, Intern. Miner. Assoc., Quant. Data File, Card 81 1200.1 (1977).
- TM65T- R. Tani and J. Fendler, Intern. Miner. Assoc., Quant. Data File, Card 81 1200.2 (1977).
- TM66- P. Tedington, Trans. Inst. Min. Met. E., 68 (1967) 169.
- TM68- R. Tenebrunser and R. Pflaum, Mineral Spectroscopy for Surface Analysis, Springer Verlag, New York (1977) 1.
- TM69- R. C. Tress, R. E. Jordan, E. J. Topping and R. McIlwain, Phil. Mag. (1977) 371.
- TM70B- R. L. Judd and E. Wilson, Can. Conf. Conf., Oct. 1975, BACC 6 (1976) 440.
- TM72- A. E. Muecke and E. L. Park, Appl. Surf. Sci., 1 (1977) 181.
- TM81- R. E. McIlwain, O. E. Edwards, Amer. Chem., 48 (1977) 1021.
- TM82T- J. Neethart, Appl. Opt., 16: 21 (1977) 3903.
- TM82T- J. Neethart, Appl. Opt., 16: 21 (1977) 3907.
- TM83- R. P. Singer and L. E. Benjardine, Chem. Soc., 69 (1977) 395.
- TM84- F. E. Schilling and R. E. McIlwain, Phil. Mag. 43 (1978) 479.
- TM85- R. Shoji, J. Mining and R. McIlwain, Phil. Mag. 43 (1978) 313.
- TM86- R. Shoji and R. Woods, Appl. J. of Chem., 36 (1978) 87.
- TM88- I. Sakai, T. Sugimoto and R. Suganaka, J. of Inst. for Chem., 49 (1979) 719.
- TM89- I. R. Shoji, J. P. Snyder, and L. E. Benjardine, Trans. Miners. Spec. Elev., 10: 2 (1979) 18.

- 7611B- B. G. Slagg and R. M. Swenson, *J. of Phys. Chem.*, **82**, 18 (1978) 1888.
- 7612- G. B. Reed and E. P. Ashby, *Ann. Chem.*, **76** (1976) 2413.
- 7613- J. B. G. Latham, J. B. Goodwin and R. Armstrong, *Physical Sciences Laboratory, Mineral Sciences Laboratory Report*, MS/MSL, 76-02 (1976) 1.
- 7614- A. R. Burstein, *Physics of Minerals and Inorganic Materials*, Springer-Verlag, New York (1976) 1.
- 7615- B. Wexler and S. Jopek, *Science and Its Sources*, ed. T. Yehuda, Krips Press, Tokyo (1976) 1.
- 7616- R. E. J. Seal, *Ann. of N.Y. Sci.*, **2** (1976) 449.
- 7617- V. V. Mazurek-Zaleski and P. A. Kluwe, *Physics Spectroscopy of Crystals*, Plenum Press, New York (1976) 1.
- 7618- G. Knebel, P. B. Hollings, A. Kozlovitch, P. Kozlovitch, R. B. Pridmore, J. A. Taylor, *Ann. Chem. Microsc.*, **2** (1976) 267.
- 7619- R. V. Selva and R. P. Seal, *Minerals Sci. Eng.*, **11**, 3 (1976) 127.
- 7620- R. P. Singer, *Science*, **19** (1976) 266.
- 7621- G. B. Wagner, G. B. Gale, and E. B. Hayward, *Ann. Chem.*, **75**, 3 (1975) 497.
- 7622- R. L. Anderson, *Minerals Sci. Eng.*, **11**, 4 (1976) 1.
- 7623- R. Wilson, *Appl. of Surf. Sci.*, **8** (1976) 179.
- 7624- R. V. Selva, J. E. Robinson, R. B. Gerson and J. E. B. Le Plante, *Ann. Microsc.*, **19** (1976) 119.
- 7625- C. de Groot, G. Boudignon, G. Knebel, *Ann. Chem. Microsc.*, **4** (1976) 89.
- 7626- L. A. Neff, *Minerals Sci. Eng.*, **12**, 3 (1976) 211.
- 7627- V. E. Melander, V. V. Selva, P. B. Kozlovitch, and G. B. Pridmore, *Surf. and Interf. Sci.*, **2**, 3 (1976) 179.
- 7628- A. Kozlovitch and P. Knebel, *Ann. Chem.*, **75** (1976) 445.
- 7629- A. Kozlovitch and P. Knebel, *Physics of Minerals and Inorganic Materials*, ed. T. Yehuda and R. J. Swillman, New York (1976) 1.
- 7630- T. Kozlovitch and G. B. Schacht, *Appl. of Surf. Sci.*, **8** (1976) 149.

- 1182- R. P. J. Salazar, Electron Beam P-Eng. Microanalysis, Van Nostrand Reinhold Co., New York (1981) 418
- 1183- P. M. Williams & Susan, and R. B. Swartz Jr., Interfacial Phenomena in Mixed Processing, eds. R. Torst and G. J. Spontaneous, New York (1981) 95.
- 1184- D. M. Bar-Gheolani, P. J. Chang, and R. L. Chang, Anal. Chem. 53 (1981) 9549
- 1185- R. S. Meloyan, J. Smoler, R. W. Shewartz and P. M. Brachfeld, J. of Vac. Sci. and Tech. 28 (1981) 704
- 1186- G. Swand, P. M. Williams, and C. De Waele, Thin Film Mater. 7 (1981) 485
- 1187- R. E. Thomas, D. A. Johnson, P. M. Williams and R. B. Freeman, Interfacial Phenomena in Mixed Processing, eds. R. Torst and R. P. Spontaneous, New York (1981) 39
- 1188- G. Swand, P. M. Williams, & T. Savinand and R. B. Swand, Thin Film Mater. 8 (1982) 385.
- 1189- R. E. Rogers and G. A. Strode, Phys. Rev. B, 27 (1983) 602
- 1190- R. A. M. Grynberg, Brit. Soc. Sci. 28 (1983) 391
- 1191- G. Briggs and R. P. Cook eds., Fractal Surface Analysis by Auger and X-ray Photoelectron Spectroscopy, John Wiley and Sons, Ltd., New York (1983) 1.
- 1192- L. J. Ruppberg, E. J. R. Smoler, and R. A. Swanson, Surf. Sci. 126 (1983) 404
- 1193- E. S. Rumer, Phys. Rev. Sol. 4, 78 (1982) 11
- 1194- R. Wells and R. E. Rogers, Surf. Sci., 126 (1982) 319
- 1195- R. S. Meloyan and J. C. Warner, Surf. Sci., 126 (1983) 321
- 1196- R. S. Meloyan, A. T. Morley, & J. Meloyan, Advances in Surface Sci., Vol. 1, 4389 Publications, New York (1983) 39
- 1197- G. Swand, P. Flor, R. Gland, P. M. Williams and P. Brachfeld, Thin Film Mater. 4 (1983) 199.
- 1198- T. Houtgast, Advances in Surface Sci., Vol. 1, 4392 Publications, New York (1983) 439
- 1199- E. Tschentsch, P. Wenzel and R. Wenzel, Surf. Sci., 126 (1983) 311
- 1200- R. P. Cook, Thin Film Mater. 8 (1983) 125

- 19800 A. B. Jagers, H. A. Jeths, and F. J. Verwey, Advances in Solid-Like Ionizing Vol. 1, AIP Publication (New York, 1983) 277.
- 198071- A. B. Buckley, I. C. Hamilton and B. Woods, J. of Appl. Electrochem., 18 (1984) 49.
- 198083- A. B. Buckley and B. Woods, Appl. of Surf. Sci., 17 (1984) 491.
- 198089- A. B. Buckley and B. Woods, Surf. J. of Chem., 71 (1984) 1993.
- 19809- B. J. Jagers, J. of Vac. Sci. and Tech., 11 (1981) 1129.
- 19809- B. J. Jagers, Electrode Properties of Solids: An Introduction for Engineers, Springer-Verlag, New York (1981) 1.
- 19810- G. Binnig, P. H. Hellweg, A. Brackwiler, P. Bandrupski, R. B. Padden and J. A. Teylor, Surf. Sci. March, 8 (1982) 1993.
- 19815- P. Bandrupski and P. H. Hellweg, J. of Vac. Sci. and Tech., 3 (1985) 1249.
- 19819- G. Binnig, B. Jagers, G. Binnig, P. Bandrupski and P. H. Hellweg, Surf. Sci. March, 3 (1985) 1993.

## BIOGRAPHICAL SKETCH

ELIZABETH A. KOSKOWSKI was born November 22, 1925, in Baltimore, Maryland. In 1944 she graduated from North Wood Senior High School. She then entered the University of Florida where she majored in mathematics. In 1948 she received her Bachelor of Science degree and was admitted to graduate school at the University of Florida in the Department of Chemical Engineering. Before starting graduate school she spent three and a half months traveling around the world. After one and a half years in the Department of Chemical Engineering while jointly working as a research assistant in the Department of Physical Science and Engineering she developed a strong interest in material science and subsequently transferred departments in the fall of 1950. In 1953 she received her Master of Science degree in Materials Science and Engineering.

She decided to continue her education by pursuing a doctorate degree in materials science and engineering. Before starting her doctorate program she worked at General Electric Research Laboratories at Kingston in Kingston, New York. In January of 1954 she started working as a full time graduate student in the area of surface science where she has been pursuing a doctorate in the Department of Materials Science and Engineering. After graduation she will take up a postdoctoral position in August of 1957 at the Max Planck Institute in Stuttgart, B. Germany.

I certify that I have read this study and that in my opinion it conforms to acceptable standards of scholarly presentation and is fully adequate, in scope and quality, as a dissertation for the degree of Doctor of Philosophy.



Paul E. Williams, Chairman  
Professor of Materials Science &  
Engineering

I certify that I have read this study and that in my opinion it conforms to acceptable standards of scholarly presentation and is fully adequate, in scope and quality, as a dissertation for the degree of Doctor of Philosophy.



Roger M. Bradley  
Professor of Materials Science &  
Engineering

I certify that I have read this study and that in my opinion it conforms to acceptable standards of scholarly presentation and is fully adequate, in scope and quality, as a dissertation for the degree of Doctor of Philosophy.



Paul E. Brown  
Professor of Materials Science &  
Engineering

I certify that I have read this study and that in my opinion it conforms to acceptable standards of scholarly presentation and is fully adequate, in scope and quality, as a dissertation for the degree of Doctor of Philosophy.



Robert T. Smith  
Professor of Materials Science &  
Engineering

I certify that I have read this study and that in my opinion it conforms to acceptable standards of scholarly presentation and is fully adequate, in scope and quality, as a dissertation for the degree of Doctor of Philosophy

  
Earl E. Bellard  
Professor of Chemical Engineering

This dissertation was submitted to the Graduate Faculty of the College of Engineering and to the Graduate School and was accepted as partial fulfillment of the requirements for the degree of Doctor of Philosophy

May, 1967

  
Dean, College of Engineering

\_\_\_\_\_  
Dean, Graduate School